
SCUOLA DI SCIENZE

Dipartimento di Chimica Industriale "Toso Montanari"

Corso di Laurea Magistrale in

Chimica Industriale

Classe LM-71 - Scienze e Tecnologie della Chimica Industriale

Bimetallic catalysts for CO₂ electroreduction

Tesi di laurea sperimentale

CANDIDATO

Luca MIGLIACCIO

RELATORE

Chiar.mo Prof. Maria Cristina CASSANI

CORRELATORE

Prof. Kazuhiro TAKANABE

Anno Accademico 2016-2017

ABSTRACT

Bimetallic catalysts for CO₂ electroreduction

Over the last decades, many steps have been taken in the search for an effective method to reduce carbon dioxide to small organic molecules that can be used as fuel or building blocks for the chemical industry. The object of this work is to prepare two bimetallic electrocatalysts utilizing Cu combined with Au or In for the efficient and selective reduction of CO₂ to CO, HCOOH and small fuels molecules. The copper-gold electrode is prepared through the electrodeposition of Cu on the surface of Au, using the underpotential deposition (UPD) technique to obtain a copper monolayer. The prepared electrode shows a high current density compared to Au electrode. Bimetallic metal oxides of CuInO₂ is used as the precursor to prepare Cu-In alloys electrodes for electrochemical reduction of CO₂. The electrocatalyst preparation is carried out using a thermal reducing treatment able to form different catalytic surfaces with different Cu-In alloys or single-phase metals. The best sample shows a high faradaic efficiency toward CO (71%) at the low overpotential of -0.8 V vs RHE. This study shows two examples of scalable and inexpensive preparation methods of bimetallic surfaces, which may use as selective electrocatalysts for the aqueous reduction of CO₂.

In questo lavoro vengono esaminati due diversi catalizzatori per la riduzione elettrochimica della anidride carbonica in soluzione acquosa. Per entrambi è utilizzato un approccio bimetallico che ha come punto cardine l'utilizzo del rame, in quanto metallo non nobile, a basso costo e facilmente reperibile. Un elettrodo è preparato depositando per via elettrochimica un singolo strato atomico di rame su una superficie di oro tramite sfruttando il fenomeno della deposizione a potenziale inferiore. I test catalitici mostrano una densità corrente maggiore di quella ottenibile utilizzando un elettrodo d'oro non modificato. Il secondo catalizzatore è preparato utilizzando un ossido misto di rame ed indio (CuInO₂), come precursore per la sintesi di una lega Cu-In in grado di convertire selettivamente la CO₂ a CO (efficienza faradica del 71%) a basse sovratensioni. Questo studio dimostra che è possibile preparare delle superfici bimetalliche per la riduzione della CO₂ in soluzione acquosa, attraverso metodi facilmente applicabili in industria.

Table of contents

Chapter 1	1
The aim of the thesis	1
1 Introduction	3
1.1 Global Warming	3
1.2 The carbon cycle	7
1.3 Challenges of CO ₂ control and utilization	8
1.4 Electrochemical reduction of CO ₂	11
1.4.1 Overview	11
1.4.2 Faradaic Efficiency	15
1.4.3 Electrode metals and reduction potential	16
1.4.4 Reaction mechanisms	19
1.4.5 Copper Alloy Electrocatalysts	23
1.5 Key challenges for the electrochemical reduction of CO ₂	25
1.6 Bibliography	27
Chapter 2	31
2 CO₂ Electroreduction on Au/Cu electrode	31
2.1 Results and discussions	33
2.1.1 Cu on Au deposition strategy	33
2.1.2 Electrochemical CO ₂ reduction measurements	38
2.2 Experimental section	44
2.2.1 Materials	44
2.2.2 Instruments	44
2.2.3 Preparation on the Au substrate	44
2.2.4 Monolayer deposition	45
2.2.5 Cu bulk layer deposition	45
2.2.6 Electrochemical reduction measurements	46
2.3 Conclusions	48
2.4 Bibliography	49

Chapter 3	51
3 CO₂ Electroreduction on Cu-In Alloy	51
3.1 Results and discussions	53
3.1.1 Synthesis of CuInO ₂ precursor and its direct use for CO ₂ reduction	53
3.1.2 Thermal reducing treatment and samples characterization	58
3.1.3 Electrochemical CO ₂ reduction measurements	70
3.2 Experimental section	77
3.2.1 Materials	77
3.2.2 Instruments	77
3.2.3 CuInO ₂ synthesis	78
3.2.4 Electrophoretic deposition	79
3.2.5 Thermal treatment	79
3.2.6 Electrochemical reduction measurements	79
3.3 Conclusions	79
3.4 Bibliography	81
Chapter 4	83
4 Conclusions	83

List of Figures

Figure 1-1. (a) Temperature anomaly recorded during the last century; data sources [2] [3]. (b) CO ₂ concentration in the atmosphere from 1980 to 2017, recorded in Mauna Loa Observatory (Hawaii).....	4
Figure 1-2. Inventories and fluxes in the carbon cycle (2008 estimates) [7].....	7
Figure 1-3. CO ₂ capture from power generation plants.	10
Figure 1-4. Walsh diagram of CO ₂ orbital energies in linear and bent geometries [22].	15
Figure 1-5. Possible structure of adsorbed CO ₂ on surface metals.	19
Figure 1-6. (a) proposed mechanism for initial electron transfer to adsorb CO as rate determining step, (b) (c) the reaction mechanisms assumed according with the observed transfer coefficient and reaction order. In orange, the Cu atoms.	21
Figure 1-7. The assumed reaction mechanisms for the formation of ethylene. (a) “Prior association” of two adsorbed CO, (b) mechanisms with CH ₂ formation. In orange, the Cu atoms.	22
Figure 2-1. Schematic representation of the electrolytic cell used for the study of the redox deposition system. (1) Au spiral counter electrode; (2) Hg/Hg ₂ Cl ₂ reference electrode; (3) Au sheet as working electrode; 50 mM H ₂ SO ₄ and 5 mM CuSO ₄ , Argon saturated electrolytic solution.	33
Figure 2-2. Deposition and dissolution of Cu on the gold polycrystalline substrate in 50 mM H ₂ SO ₄ + 5 mM CuSO ₄ . CV of bulk deposition of Cu on Au (blue line). CV of monolayer deposition (red line). Blank acquisition in 50 mM H ₂ SO ₄ solution (black-dash line).	34
Figure 2-3. Deposition of a Cu monolayer using a linear sweep voltammetry from 0.92 to 0.40 V vs RHE.	35
Figure 2-4. XPS spectra of Cu 2p for the Cu monolayer on Au substrate.	36
Figure 2-5. Current density comparison among Au, Au/Cu _{ML} , Au/Cu _{5nm} and Au/Cu _{10nm} electrodes (0.1 M KHCO ₃ , pH 6.8, saturated CO ₂).	39
Figure 2-6. Faradaic efficiency analysis of Au electrode at applied potentials for H ₂ (blue), CO (red) and HCOOH (green). The Faradaic efficiency showed is an average value calculated at the steady-state current and product concentration (0.1 M KHCO ₃ , pH 6, saturated CO ₂).	40
Figure 2-7. Faradaic efficiency analysis of Au/Cu _{ML} electrode at applied potentials for H ₂ (blue), CO (red) and HCOOH (green). The Faradaic efficiency showed is an average value calculated at the steady-state current and product concentration (0.1 M KHCO ₃ , pH 6.8, saturated CO ₂).	41
Figure 2-8. Faradaic efficiency analysis of the Au/Cu _{5nm} electrode at applied potentials for H ₂ (blue), CO (red) and HCOOH (green). The Faradaic efficiency showed is an average value	

calculated at the steady-state current and product concentration (0.1 M KHCO ₃ , pH 6.8, saturated CO ₂).	42
Figure 2-9. Faradaic efficiency analysis of the Au/Cu _{10nm} electrode at applied potentials for H ₂ (blue), CO (red) and HCOOH (green). The Faradaic efficiency showed is an average value calculated at the steady-state current and product concentration (0.1 M KHCO ₃ , pH 6.8, saturated CO ₂).	43
Figure 2-10. Scheme of the electrochemical cell used for the electrochemical measurements and the products analysis system. (1) Pt spiral counter electrode; (2) Ag/AgCl reference electrode; (3) working electrode;(4) glass chamber for the counter electrode; (5) 0.1 M KHCO ₃ , CO ₂ saturated electrolytic solution; (6) inlet of CO ₂ gas; (7) outlet of gas products.	47
Figure 3-1. Delafossite crystal structure of CuInO ₂ . Crystal lattice data obtained from the website: http://www.catalysthub.net/ and elaborated using the open source software VESTA 3.4.0 (Visualization for Electronic and Structural Analysis).	53
Figure 3-2. XRD diffractogram of CuInO ₂ as prepared heating at 400°C.	54
Figure 3-3. XRD diffractogram of CuInO ₂ as prepared heating at 500°C.	55
Figure 3-4. Schematic representation of Electrophoretic deposition of CuInO ₂ on carbon paper substrate.	56
Figure 3-5. Chronopotentiometric electrolysis profile at current density of -1.67 mA cm^{-2} (0.1 M KHCO ₃ , pH 6.8, CO ₂ saturated).	57
Figure 3-6. XRD diffractogram of the electrode surface after CO ₂ reduction experiment.	58
Figure 3-7. TGA of CuInO ₂ , Cu ₂ O and In ₂ O ₃ obtained by flowing a H ₂ 4% in Argon stream, with a ramping rate of $10 \text{ }^\circ\text{C min}^{-1}$ in a temperature range from 25 to 900 °C.	60
Figure 3-8. TPR analysis of CuInO ₂ , Cu ₂ O and In ₂ O ₃ obtained by flowing a H ₂ 4% in Argon stream, with a ramping rate of $10 \text{ }^\circ\text{C min}^{-1}$ in a temperature range from 25 to 900 °C.	61
Figure 3-9. XRD profile of the CuInO ₂ on carbon paper sample thermal reduced at 450 °C under H ₂ 4% flow in argon (300 mL min^{-1}).	62
Figure 3-10. XRD profile of the CuInO ₂ on carbon paper sample thermal reduced at 600 °C under H ₂ 4% flow in argon (300 mL min^{-1}).	63
Figure 3-11. XRD profile of the CuInO ₂ on carbon paper sample thermal reduced at 800 °C under H ₂ 4% flow in argon (300 mL min^{-1}).	64
Figure 3-12. SEM images of the CuInO ₂ powder.	65
Figure 3-13. SEM images of the thermal reduced sample at 450 °C.	66
Figure 3-14. SEM images of the thermal reduced sample at 600 °C.	68
Figure 3-15. SEM images of the thermal reduced sample at 800 °C.	69
Figure 3-16. Chronopotentiometric electrolysis of thermally reduced samples at a current density of -1.67 mA cm^{-2} in CO ₂ saturated 0.1 M KHCO ₃ .	70

Figure 3-17. Comparison of the Faradaic Efficiencies obtained during the CO ₂ reduction experiments at constant current density.	71
Figure 3-18. XRD analysis of the 450 °C sample before CO ₂ reduction experiment.	72
Figure 3-19. XRD analysis of the 450 °C sample after CO ₂ reduction experiment.	72
Figure 3-20. Current density and Faradaic efficiencies of the 200 °C thermally reduced sample at various applied potentials from -0.4 to -0.8 V vs RHE in CO ₂ saturated 0.1 M KHCO ₃ solution.	73
Figure 3-21. Current density and Faradaic efficiencies of the 450 °C thermally reduced sample at various applied potentials from -0.4 to -0.8 V vs RHE in CO ₂ saturated 0.1 M KHCO ₃ solution.	74
Figure 3-22. Current density and Faradaic efficiencies of the 600 °C thermally reduced sample at various applied potentials from -0.4 to -0.8 V vs RHE in CO ₂ saturated 0.1 M KHCO ₃ solution.	75
Figure 3-23. Current density and Faradaic efficiencies of the 800 °C thermally reduced sample at various applied potentials from -0.4 to -0.8 V vs RHE in CO ₂ saturated 0.1 M KHCO ₃ solution.	76

List of Tables

Table 1.1. The 1992-2013 CO ₂ Emissions per Region/Country (Giga Tons). Data Source: Carbon Dioxide Information Analysis Center, Environmental Sciences Division, Oak Ridge National Laboratory, Tennessee, United States.	6
Table 1.2. Physical and chemical properties of carbon dioxide [16].	12
Table 1.3. Standard potentials of reduction of CO ₂ in aqueous solution at pH 7 at 25 °C and 1 atm [21].	14
Table 1.4. Faradaic efficiencies of Products in CO ₂ reduction at various metal electrodes ^a	18
Table 2.1. Electrochemical deposition parameters for the bulk copper layer on gold substrate...	38

Chapter 1

The aim of the thesis

This thesis work was carried out at KAUST Catalysis Center (Saudi Arabia), at the group of Photocatalysis, under the supervision of the Prof. Kazuhiro Takahashi. The development of a highly efficient and selective catalyst for the electrochemical reduction of CO₂ is one of the biggest scientific challenges; which focused the attention of the academic world and major company.

The purpose of our experimental work was to explore the catalytic performance of a bimetallic catalyst consisting of a substrate of Au covered by a Cu layer at various thickness. In particular, the study aimed to increase the selectivity of Cu towards methane and ethylene production, exploiting the electronic effect due to the presence of a gold substrate.

Afterwards, considering the peculiarities of oxide derived copper (OD-Cu) as a catalyst for CO₂ reduction and the effects of the presence of an adjacent heteroatom, our attention focused on optimizing the preparation of a catalyst already studied with the aim of improving its applicability to an industrial level. A bimetallic oxide of copper and indium has been successfully used as a precursor of a Cu-In alloy for CO₂ reduction. High selectivities towards CO and formic acid at relatively low overpotential were found, with a total faradic efficiency of 94% CO₂ reduction. However, the electrochemical reduction of this precursor to Cu-In alloy has low reproducibility, for this reason, it has been explored the possibility of using a thermal approach to form the Cu-In alloy.

1 Introduction

1.1 Global Warming

Concerns about global warming have led to an increase in interest in reducing atmospheric carbon dioxide (CO₂) concentrations. While research groups base their work on the search for alternative processes with low CO₂ production, the need to find a solution to stabilize carbon concentration in the atmosphere becomes more and more urgent, pending a final transition to low-carbon alternatives. Thus, today's challenge is to make carbon dioxide no longer a problem, but as a resource that used in energy production.

Global warming is a phenomenon of an increase in the average surface temperatures of the Earth, which is not due to natural causes and found since the beginning of the 20th century. Such warming has been found to be not uniform across the globe, but hottest areas (in the northern hemisphere) are present and are more pronounced on the mainland than in the marine waters [1].

In *Figure 1-1 a* are shown the GISS Surface Temperature Analysis (GISTEMP), an estimate of global surface temperature change. The data are collected around the middle of every month from NOAA GHCN v3 (meteorological stations), ERSST v4 (ocean areas), and SCAR (Antarctic stations) [2] [3].

Global warming is now 0.6 °C over the last three decades, while in the last century the average annual temperature has increased by 0.8 °C. A misplaced platitude says that most of the global warming occurred before 1940. During the first half of the twentieth century there was a moderate fluctuating temperature increasing, but since 1975 the average temperature increased faster, with a mean speed of 0.2 °C per decade [4].

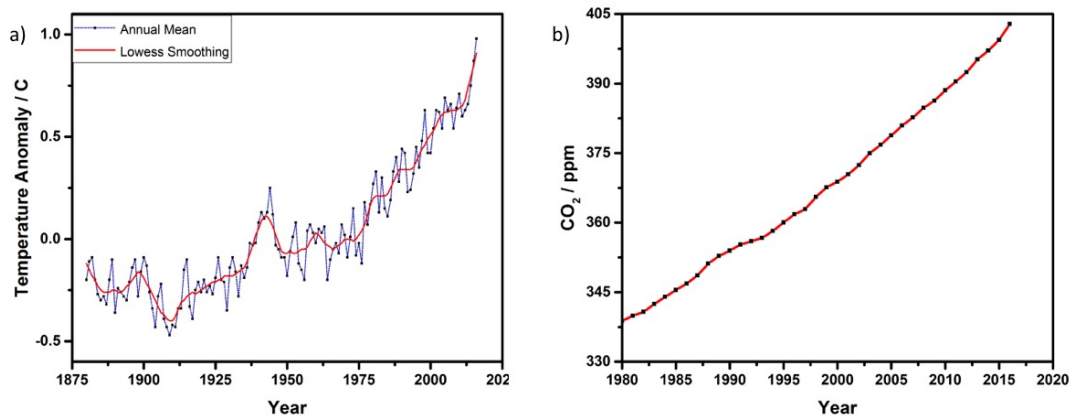


Figure 1-1. (a) Temperature anomaly recorded during the last century; data sources [2] [3]. (b) CO₂ concentration in the atmosphere from 1980 to 2017, recorded in Mauna Loa Observatory (Hawaii).

This global average increase would be attributable to the increase in the atmospheric concentration of greenhouse gases, particularly carbon dioxide, which is a consequence of human activity especially the generation of energy using fossil fuels and deforestation. The main greenhouse gases are: water vapor, responsible for the greenhouse effect in a percentage ranging between 36-70%; carbon dioxide (CO₂), which affects 9-26%; methane (CH₄), which affects 4-9%; ozone (O₃), which affects between 3-7% [5].

CO₂ globally released results from different sources, both natural and anthropogenic globally. Among natural sources, there are soils, inland waters, oceans and volcanic activities; instead, the main anthropogenic sources include cement industry, metrics, land transport, aviation, shipping, and compost reactors. However, the main cause of CO₂ emissions is the combustion of fossil fuels, which are the primary contributors to climate change [6].

Human activity has always produced carbon dioxide, but the earth-atmosphere system has always managed to self-regulate CO₂ concentration in the various environmental compartments. From about 1750 until 2000, however, the concentration of carbon dioxide in the atmosphere increased from 280 ppm to 368 ppm, and about 388 ppm in 2010 [7]. In 2015, the value of 400 ppm was exceeded, as it was recorded at the Mauna Loa observatory (Figure 1-1 b).

Anthropogenic CO₂ emissions vary by country or region is taken into account (Table 1.1). Reading the collected data, we can see that the United States is one of the countries with the highest emissions. However, a 10.4% decline from 2007 to 2013 was obtained,

due to the global financial crisis [8] and some green policy. On the other hand, China has surpassed the United States since 2007 in CO₂ emissions by almost four times their emissions in 20 years.

The European Union has relatively low CO₂ emissions compared to those of China and the United States. The country with the highest value being Germany, which with 0.76 GigaTons in 2013 representing 22.3% of European emissions, followed by United Kingdom, Italy and France.

However, it should be emphasized that direct carbon dioxide emissions represent only a small proportion when compared to natural carbon streams. In order to better understand the effects of human activity on the climate, it is necessary to consider how these affect the mechanisms of exchange between the various environmental compartments: for example, land use has reduced the carbon absorption capacity of the soil, while acidification of the oceans entails less CO₂ absorption capacity [7].

Table 1.1. The 1992-2013 CO₂ Emissions per Region/Country (Giga Tons). Data Source: Carbon Dioxide Information Analysis Center, Environmental Sciences Division, Oak Ridge National Laboratory, Tennessee, United States.

Countries	1992	1998	2002	2007	2013
<u>European Union</u>	3,99	3,96	3,96	4,00	3,41
• <i>United Kingdom</i>	0,56	0,53	0,53	0,53	0,46
• <i>France</i>	0,37	0,38	0,37	0,37	0,33
• <i>Italy</i>	0,42	0,44	0,45	0,46	0,34
• <i>Germany</i>	0,89	0,86	0,83	0,78	0,76
<u>Americas</u>	6,40	7,24	7,55	7,92	7,54
• <i>United States</i>	4,91	5,41	5,65	5,79	5,19
• <i>Canada</i>	0,44	0,51	0,52	0,54	0,48
• <i>Brazil</i>	0,22	0,31	0,33	0,36	0,50
Japan	1,12	1,16	1,22	1,25	1,24
Russian Federation	2,08	1,50	1,56	1,67	1,79
China	2,70	3,32	3,69	6,79	10,25
India	0,70	0,94	1,05	1,41	2,03
Arab World	0,80	0,91	1,06	1,36	1,77
East Asia & Pacific	0,80	1,07	1,22	1,63	2,30

1.2 The carbon cycle

Atmospheric CO₂ concentration is the result of complex exchanges between the atmosphere, the biosphere and the ocean masses, becoming part of the carbon cycle complex. About 40% of the amount of CO₂ emitted by human activities is absorbed by vegetation and oceans every year, whereas the residual 60% remains in the atmosphere [9].

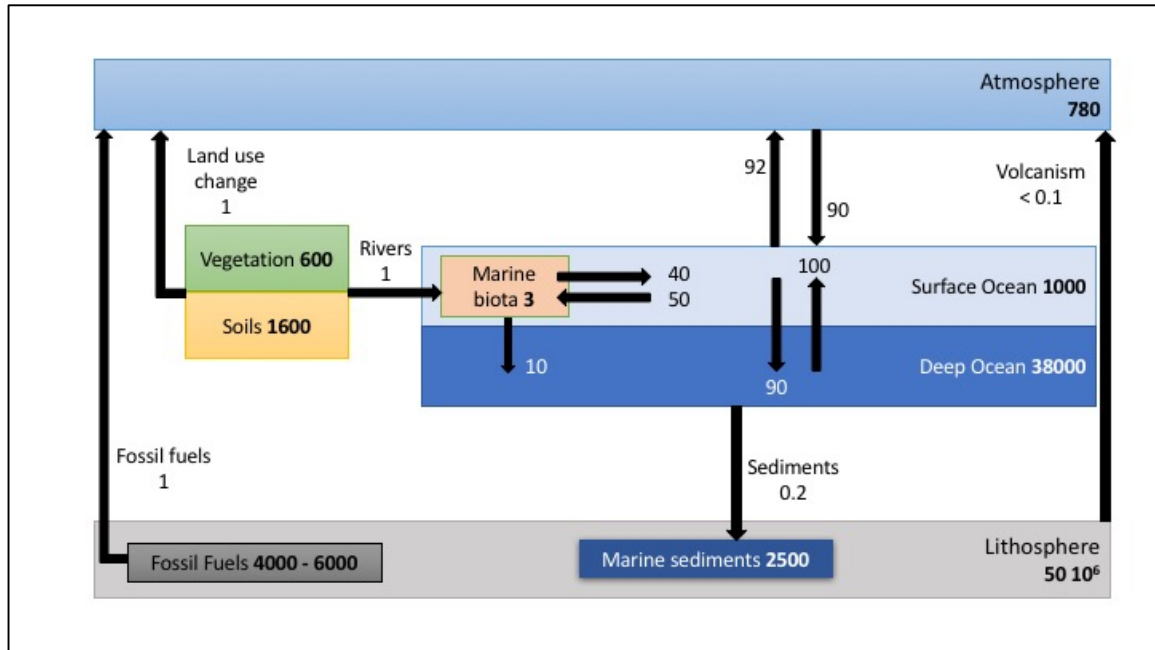
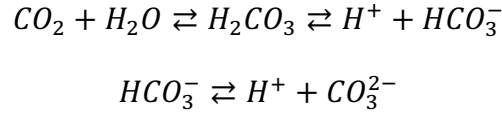


Figure 1-2. Inventories and fluxes in the carbon cycle (2008 estimates) [7].

Given the global problem, the carbon cycle (*Figure 1-3*) is governed by a source-accumulation mechanism, so there are several sites where carbon is stored, in particular: atmosphere, vegetation or biomass, soil, oceans and lithosphere. The carbon breakdown between the different sites is regulated by flows. A flow is defined as the quantity of an entity that passes through a closed surface per unit of time, if the flow is out of the surface, this becomes a source, but if the stream is incoming it becomes a storage site [10].

Oceans are the main carbon storage site on Earth, where it is estimated that there are about 38,000 GT of inorganic carbon equivalent to approximately 50 times the carbon present in the atmosphere [11]. Each year, about 90 GT of carbon are released into the atmosphere and about 92 GT are absorbed by the oceans. So, this continuous exchange of CO₂ between atmosphere and oceans results in a net absorption of carbon dioxide of about 2 GT per year from the oceans [12]. CO₂ absorption takes place in the surface of the ocean, where carbon dioxide dissolves forming carbonic acid, a weak acid which will be in equilibrium with water.



Once it has been absorbed, the carbon tends to move from the surface layer (300 m) to the ocean depths. Due to the increased solubility of CO₂ in cold water and high salinity, the absorption efficiency depends on latitude, resulting in the formation of cold and dense water masses [11].

Phytoplankton plays a key role in the absorption of carbon dioxide, which in fact contributes through the photosynthesis process to lower the partial pressure of CO₂ in the surface layers of the oceans, thus favoring the absorption of CO₂ from the atmosphere. It has been estimated that this phenomenon contributes to reducing the concentration of carbon dioxide in the atmosphere by about 150-200 ppm. Indeed, about 25% of the carbon bound through the photosynthesis is deposited in the ocean depths in the form of calcium carbonate (from phytoplankton shells) [11].

As for the atmosphere, it has been estimated that a carbon content of 750 GT and the CO₂ concentration is currently around 400 ppm that increasing every year about 2ppm [7]. Concentration depends heavily on interaction with other environmental compartments, especially the earthy vegetation with photosynthesis determines a fluctuating seasonal pattern during the year.

1.3 Challenges of CO₂ control and utilization

Greenhouse gas emissions are mainly due to the consumption of fossil fuels. Among them, CO₂ emission control is the most important area for controlling greenhouse gas emissions. In recent decades, the international community is moving towards finding long-term solutions that can stop the growth of CO₂ concentration in the atmosphere.

There are mainly five technical options for controlling carbon dioxide emissions: energy choices, energy efficiency and CO₂ capture, sequestration and utilization.

Choosing an energy source is the first step to reducing CO₂ emissions. A straightforward example would be to opt to use natural gas rather than charcoal. Generally, the H/C ratio in hydrocarbons is inversely proportional to the amount of carbon dioxide emitted [13]. The alternative is to choose a renewable source such as hydroelectric energy, solar energy, wind power and biomass.

Improving energy efficiency is another important area with a high impact on CO₂ production. In the United States, the energy efficiency of systems to produce electricity from fossil sources is around 35%, for cars this figure is even lower, around 20% [14]. So, the development of new energy utilization systems, such as new hybrid-powered vehicles, can implement efficiencies at 30% or more. Likewise, the development of new catalysts that can selectively reduce the formation of CO₂ in oxidation reactions is a significant commitment to modern industries [15].

Carbon dioxide can be considered not only as a greenhouse gas but also as a starting reagent to obtain various organic chemicals or fuels. The key word represents the use of renewable sources (such as solar energy) to derive the energy needed to convert CO₂.

CO₂ is not a high added value product but is often the defective product of many industrial processes. The energy consumption that leads to the formation of CO₂ represents a loss in economic terms. However, it is interesting to note that the amount of CO₂ emitted as a CO₂ rich stream by the production plants and waste gas from the manufacturing industry is far more than the amount of carbon used to produce many chemicals, organic materials and liquid transport fuels [16].

The primary barrier to using CO₂ is the lack of driving forces pushing the market towards this direction. In particular, it is necessary to consider that a fundamental part of the total price of the operation is the costs of capture, storage, separation, purification and transport of CO₂.

Three different approaches to carbon dioxide capture can be identified [7]:

- As a pure or near-pure CO₂ stream (from industrial process).
- Concentration of the discharge from an industrial process into a pure or near-pure CO₂ stream.
- Direct air capture into a pure stream of CO₂ or into a stable product.

Carbon dioxide content in a stream from power generation plants that use fossil fuels varies between 3% (typically for plants using natural gas) and 15% (coal-fired plants). CO₂ capture from power generating plants is known as "post-combustion capture" and involves the use of various separation technologies including chemical and physical absorbents and membranes. As an alternative to post-combustion capture, there are two possible modifications to the combustion process. One of them is the oxyfueling, which consists in a fuel combustion in pure oxygen that allows obtaining a pure CO₂ stream that can be

directly compressed and transported. The second alternative, called "pre-combustion capture", involves a partial oxidation of fuel that forms a flow of a mixture of H₂ and CO₂ with a percentage of CO₂ between 15-60% which can be readily separated using the techniques used for the post-combustion capture. The resulting hydrogen and fuel stream can be conventionally combusted in a turbine gas [7].

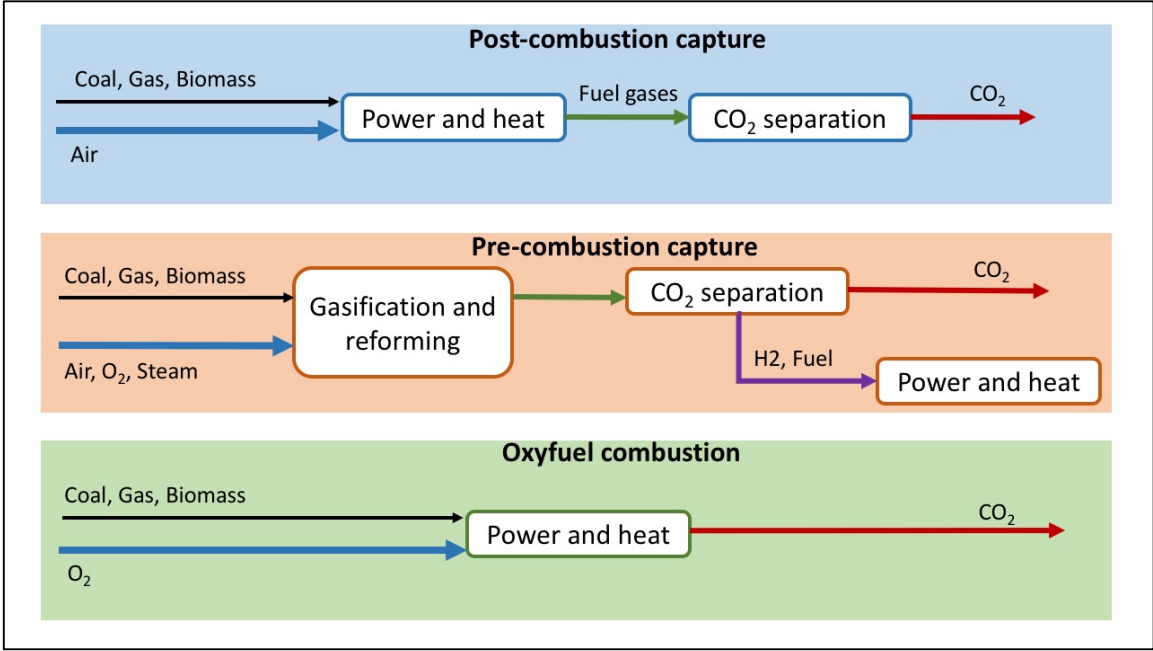


Figure 1-3. CO₂ capture from power generation plants.

The direct capture of CO₂ from the atmosphere represents an opposite situation concerning the case of the cement industry. In fact, the concentration of CO₂ in the air, as seen before, is considerably lower (about 400 ppm), which makes the absorption process much more complicated. A spray-tower system that uses a sodium hydroxide solution as the absorbent liquid, which has been shown to absorb 15 tons of CO₂ per year per square meter on a laboratory scale [17]. However, the scale-up of such a plant would require absorbing walls of about 15 meters long and up to 6 km long. The strength of this process is that, unlike the ones described above, it does not change the CO₂ emissions, but directly affects the reduction of carbon dioxide concentration in the atmosphere [7].

To capture CO₂ different techniques are currently being studied and used. Among these, which are most promising at the moment are geological storage and ocean storage.

In the first case, oil or gas reserves or in non-potable water formations are used; CO₂ is injected directly into the geological formation where it is trapped. The use of saline-

water storage is much more accessible than oil or gas storage; it is estimated to be two or three times greater [7] [18].

In the case of ocean storage, however, the basic idea is to take advantage of the ocean's storage capacity over the atmosphere. Long-term storage can be achieved by gaseous CO₂ venting or supercritical fluid at a depth sufficient to avoid rising to surface water. Alternatively, CO₂ can be stored as a supercritical glider at very high pressures under 3000 meters of depth. Pools of this type have been observed nearby the deep water hydrothermal vents as a result of the separation of CO₂ from vented gases. Other options for oceanic storage include increased photosynthetic activity in nutrient-depleted surface waters, including through direct fertilization [7].

1.4 Electrochemical reduction of CO₂

1.4.1 Overview

Carbon dioxide is, with water, the final combustion product of any carbon and hydrogen containing compounds. CO₂, a 16e⁻ molecule, (molar weight 44.0 g mol⁻¹) is a colorless and odorless gas. It is an apolar linear molecule (O=C=O), in which the oxygen atoms are each covalently double bonded to a single carbon atom. Carbon dioxide has two different reaction sites: the carbon atom is an electrophile; instead, the oxygen atoms are nucleophiles. This particular aspect makes CO₂ a bifunctional catalyst [19]. The carbon dioxide is the more stable among carbon based substances under the environmental conditions, for this reason, its chemistry is very poor. With a C=O bond energy of 187 kcal mol⁻¹, much higher than C=C (145 kcal mol⁻¹) and O=O (116 kcal mol⁻¹) bonds [6], is possible to understand the low reactivity of CO₂.

Table 1.2. Physical and chemical properties of carbon dioxide [16].

Property	Value and unit
<i>Molecular weight</i>	44.01 g mol ⁻¹
<i>Sublimation point at 1 atm</i>	-78.5 °C
<i>Triple point at 5.1 atm</i>	-56.5 °C
<i>Triple point pressure</i>	5.185 bar
<i>Critical Temperature (T_c)</i>	31.04 °C
<i>Critical Pressure (P_c)</i>	72.85 atm (7383 kPa)
<i>Critical Density (ρ_c)</i>	0.468 g cm ⁻³
<i>Gas Density at 0 °C and 1 atm</i>	1.976 g dm ⁻³
<i>Solid Density</i>	1560 g dm ⁻³
<i>Specific volume at 1 atm and 21 °C</i>	0.546 m ³ kg ⁻¹
<i>Latent heat of vaporization at the triple point (-78.5 °C)</i>	353.4 J g ⁻¹
<i>Latent heat of vaporization at 0 °C</i>	231.3 J g ⁻¹
<i>Viscosity at 25 °C and 1 atm CO₂</i>	0.015 cP
<i>Solubility in water at 25 °C and 1 atm</i>	0.759 mL CO ₂ / mL H ₂ O
<i>Heat of formation at 25 °C, ΔH° gas</i>	-393.5 kJ mol ⁻¹
<i>Entropy of formation at 25 °C, S° gas</i>	213.6 J K ⁻¹ mol ⁻¹
<i>Gibbs free energy of formation at 25 °C, ΔG° gas</i>	-394.3 kJ mol ⁻¹
<i>Heat capacity under constant pressure at 25 °C</i>	37.1 J mol ⁻¹ °C ⁻¹
<i>Heat capacity under constant volume at 25 °C</i>	28.1 J mol ⁻¹ °C ⁻¹
<i>Thermal conductivity</i>	14.65 mW m ⁻¹ K ⁻¹
<i>Viscosity at 0 °C</i>	0.0001372 Poise

The conversion of CO₂ to valuable chemicals is the most important target for reducing the emissions of this greenhouse gas into the atmosphere. Indeed, to date, the ability to control CO₂ emissions using only renewable energy sources (e.g. solar, wind and water) is the less efficient. The major reason is the absence of large-scale energy storage systems, which can overcome the intermittent nature of renewable sources. The main products of carbon dioxide reduction are carbon monoxide (CO), formic acid (HCOOH), oxalic acid (H₂C₂O₄), methane (CH₄), methanol (CH₃OH), formaldehyde (CH₂O), ethylene (CH₂CH₂) and ethanol (CH₃CH₂OH) [6]. Various approaches to the formation of these products may be used: homogeneous catalysis, heterogeneous catalysis, photocatalysis or electrochemical reduction. Among them, the electrochemical reduction has the advantage of using renewable resources as the source of electricity, making this approach the one with the highest environmental compatibility.

Also, CO₂ conversion using an electrochemical approach has great interest due to various technical advantages. The process is easily controllable by modulating the applied potential and the reaction temperature; the supporting electrolyte can be completely recycled, minimizing the total consumption of chemicals; the electrochemical reaction system is compact, modular and easy for scale-up for industry application [20].

In an electrochemical cell, the reduction of carbon dioxide occurs at the cathode while the anode takes on the reaction of oxygen evolution. As can be seen in Table 1.3, although the CO₂ reactivity is very low, CO₂ reduction potential is not very negative when compared to the hydrogen evolution reaction in aqueous electrolyte solution (equation 7).

However, the carbon dioxide reduction is not so easy, because the real potential for CO₂ reduction is much more negative than the equilibrium potential. The cause of this wide overpotential is the formation of the intermediate CO₂·⁻, which is formed by electronic transfer from the electrode to a CO₂ molecule (equation 8) [21]. The formation of this reaction intermediate was proposed in 1960 by Jordan and Smith, and later, using polarography technique was discovered that the formation of this intermediate is the determining step of the CO₂ reduction [21].

Table 1.3. Standard potentials of reduction of CO₂ in aqueous solution at pH 7 at 25 °C and 1 atm [21].

Half-Electrochemical Thermodynamic Reactions	Electrode Potentials (V vs. SHE)	
$CO_2 + H_2O + 2e^- \rightarrow HCOO^- + OH^-$	-0.43	(1)
$CO_2 + H_2O + 2e^- \rightarrow CO + 2OH^-$	-0.52	(2)
$CO_2 + 6H_2O + 8e^- \rightarrow CH_4 + 8OH^-$	-0.25	(3)
$2CO_2 + 8H_2O + 12e^- \rightarrow C_2H_4 + 12OH^-$	-0.34	(4)
$9CO_2 + 9H_2O + 12e^- \rightarrow C_2H_5OH + 12OH^-$	-0.33	(5)
$3CO_2 + 13H_2O + 18e^- \rightarrow C_3H_7OH + 18OH^-$	-0.32	(6)
$2H_2O + 2e^- \rightarrow 2OH^- + H_2$	-0.41	(7)
$CO_2 + e^- \rightarrow CO_2^{\cdot-}$	-1.90	(8)

The reaction mechanisms of the CO₂ reduction on metal electrodes has been amply studied during the last decades. Nevertheless, the mechanisms of formation of small organic molecules as products are not entirely clear. The main complication is due to the wide variety of products and the number of transferred electrons that can occur on the surface of the electrode. The assumptions now accepted come from the observation of charge transfer and the use of macroscopic electrochemical testing for the reaction orders determination.

The exact geometry of CO₂^{·-} on metal surface is still unclear but, looking at the Walsh diagram in *Figure 1-5*, is possible to better understand bonds angles of CO₂ and its intermediate. The highest occupied molecular orbital (HOMO) is the 1π_g orbital, that represent the π-C-O bonds [22]; the lowest unoccupied molecular orbital (LUMO) is the 2π_u orbital, that represent the π lone pairs. The diagram shows how the energy position of the orbitals change when the linear geometry is bent.

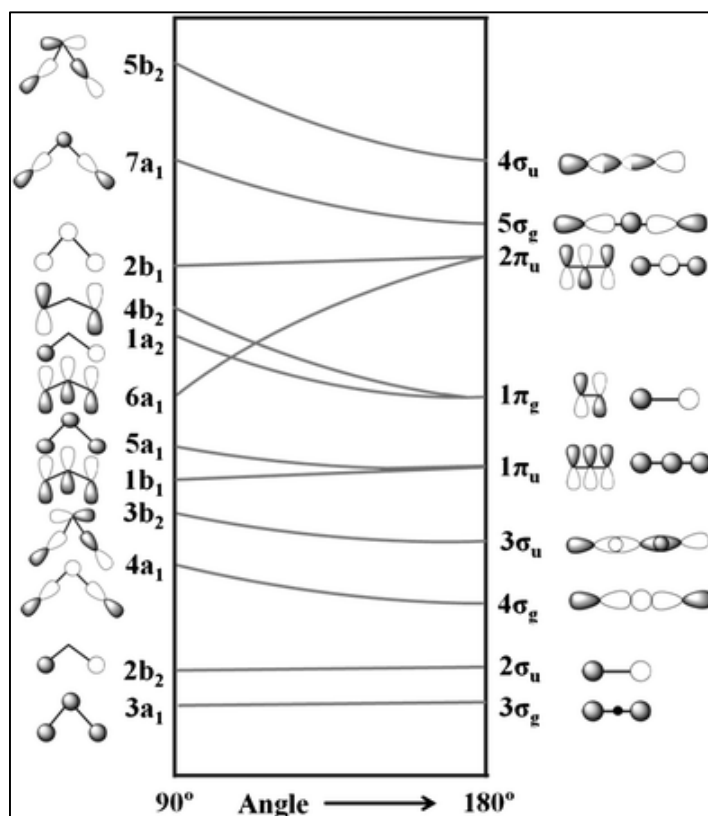


Figure 1-4. Walsh diagram of CO_2 orbital energies in linear and bent geometries [22].

In the bent molecules, the degeneracies of all π orbital are split in energies. In the case of the $1\pi_g$ orbital in both degeneracies the energy required to maintain the new geometric conformation is higher than the linear geometry, on the other hand, in the case of the $2\pi_u$ orbital, there is a stabilization in energy terms. The Walsh diagram explains why the bond angle of the CO_2 absorbed on the metal electrode surface is close to 133° , because of the occupancy of the HOMO with an electron in the $\text{CO}_2^{\cdot-}$ intermediate [19].

1.4.2 Faradaic Efficiency

The faradaic efficiency (F.E.) is one of the most popular indexes used to measure the utilization efficiency of electricity when two or more faradaic reactions co-occur at an electrode. In other words, the faradaic efficiency of a specific product of CO_2 electroreduction reveals the ratio between the amount of energy (electrons) the system requires and the amount of the product formed. It is calculable from the number of electrons consumed in the electro reduction process:

$$F.E. = \frac{mn\mathcal{F}}{\int_0^t i_{r,t} dt}$$

where m is the number of moles of product formed, n is the number of electrons required for the formation of one molecule of product, \mathcal{F} is the Faraday constant and $i_{r,t}$ is the circuit current. The integration of current in the time interval corresponding at the charges passed through the electrode.

The F.E. towards a product may be affected by several factors; many experimental results show that changing the system parameters the selectivity of the process can significantly change. Certainly, the F.E. depends on the element or chemical composition of the catalyst [23]; but also, the morphology of the electrode surface is a critical parameter, for example, the thickness of the catalyst layer or the catalyst particle size [24] [25]. Other experimental conditions such as pH, reaction time and temperature, may be essential parameters to evaluate the faradaic efficiency [26].

1.4.3 Electrode metals and reduction potential

The catalyst material influences, at the same operating conditions (e.g. temperature, CO₂ concentration, electrolyte solution), the selectivity of the CO₂ reduction reaction. The previous study by Hori's group shows that it is possible to classify the electrocatalytic metals into four fundamental groups [21]:

- The 1st group consists of several metals characterized by a high hydrogen overvoltage, low absorption capacity of CO, and high overvoltage for CO₂ to CO₂^{•-}, and consequently weak stabilization of that intermediate. The metals included in this group are Hg, Pb, In, Sn, Cd, and the major product from CO₂ reduction is formate ion (HCOO⁻).
- The 2nd group consists of metals characterized by a medium hydrogen overvoltage, the weak absorption capacity of CO, and can catalyze the breakage of the C–O bond and at the same time, promotes the desorption of CO. The metals included in this group are noble metals such as Au and Ag but also Pd, Zn and Ga. The major product from CO₂ reduction is carbon monoxide (CO).
- The 3rd group consists of metals characterized by a low hydrogen overvoltage. Therefore, the hydrogen evolution reaction is the main reaction that occurs on the electrode's surface. The metals of this group are Ni, Fe, Pt and Ti.
- The 4th group include only Cu, which has unique features for the CO₂ reduction. Indeed, it is able to produce a significant amount of methane and ethylene because of its peculiar characteristics.

Previously, the standard potential of the reduction of CO_2 was showed in Table 1.3: the thermodynamic potential depends on the products, for example at 25 °C and pH 7 the required potentials to obtain CO and HCOO^- are -0.52 and -0.43 V vs SHE respectively. However, Table 1.4 shows the experimental values of the potentials required for the reduction of CO_2 at the same current density. These potentials are much more negative than those obtained from thermodynamic data because, as discussed above, the main reason is that the formation of the $\text{CO}_2^{\cdot-}$ radical anion as intermediate species requires a large overpotential.

In order to better understand how the potential depends on the metal used as a catalyst, it is interesting to compare the potential needed for CO_2 reduction, for each metal, and the respective heat of fusion. Interestingly, the HCOO^- formation metals need a very negative potential and have a low heat of fusion value. On the other hand, the CO formation metals need a less negative potential and have a higher heat of fusion value [21]. The heat of fusion of metals is correlated to the extent of d electron contribution to metallic bond and may be used as a measure of the availability of the d electrons [27]. The extent of the stabilization of $\text{CO}_2^{\cdot-}$ depends on d electron availability. Therefore, in case of metals such as Au, Cu, Ag, Zn, with a high heat of fusion, the stabilization of $\text{CO}_2^{\cdot-}$ is high and this means that an extra negative charge on oxygen atom promotes the protonation of CO_2 followed by formation of CO [28].

Table 1.4. Faradaic efficiencies of Products in CO₂ reduction at various metal electrodes ^a.

	Electrode	Potential vs. SHE (V)	Faradaic Efficiency (%)						
			CH ₄	C ₂ H ₄	EtOH	PrOH	CO	HCOO ⁻	H ₂
1 st group	Pb	-1.63	0.0	0.0	0.0	0.0	0.0	97.4	5.0
	Hg ^a	-1.51	0.0	0.0	0.0	0.0	0.0	99.5	0.0
	In	-1.55	0.0	0.0	0.0	0.0	2.1	94.9	3.3
	Sn	-1.48	0.0	0.0	0.0	0.0	7.1	88.4	4.6
2 nd group	Au	-1.14	0.0	0.0	0.0	0.0	87.1	0.7	10.2
	Ag	-1.37	0.0	0.0	0.0	0.0	81.5	0.8	12.4
	Zn	-1.54	0.0	0.0	0.0	0.0	79.4	6.1	9.9
	Pd	-1.20	2.9	0.0	0.0	0.0	28.3	2.8	26.2
3 rd group	Ni	-1.48	1.8	0.1	0.0	0.0	0.0	1.4	88.9
	Fe	-0.97	0.0	0.0	0.0	0.0	0.0	0.0	94.8
	Pt	-1.07	0.0	0.0	0.0	0.0	0.0	0.1	95.8
4 th group	Cu	-1.44	33.3	25.5	5.7	3.0	1.3	9.4	20.5

a) Experiments conditions: 0.1 M KHCO₃, T=18.5 °C, 5 mA cm⁻². The current density applied on Hg was 0.5 mA cm⁻². Readapted from [28].

1.4.4 Reaction mechanisms

The reaction mechanisms on the electrode surface depend mainly on the nature of the metal catalyst and its interaction with the $\text{CO}_2\cdot^-$ radical anion intermediate. There are two different ways to adsorb the CO_2 on the metal surface: can take place an interaction with carbon or oxygen or both, to form carbon or oxygen coordination, or mixed coordination respectively (Figure 1-6). The coordination with the metal surface is crucial for the following step. In fact, there are two main pathways for the consecutive reduction of the adsorbed $\text{CO}_2\cdot^-$, which implicates the formation of the two major main products of CO_2 reduction, carbon monoxide and formate ion.

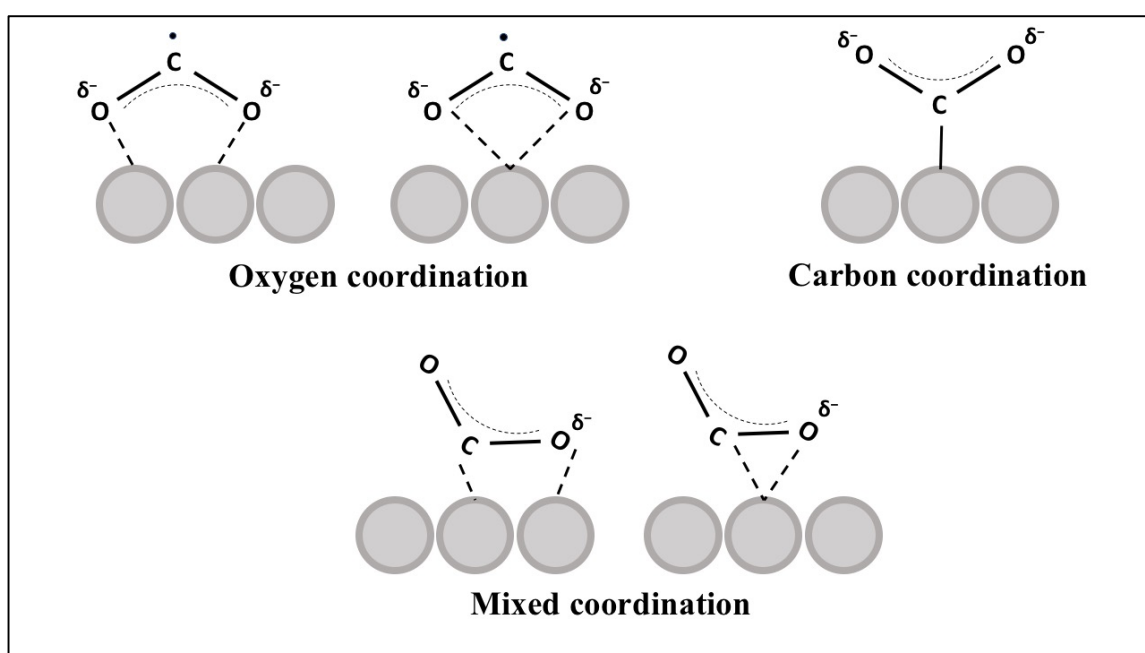
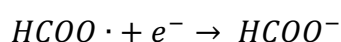
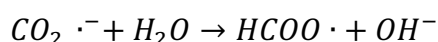


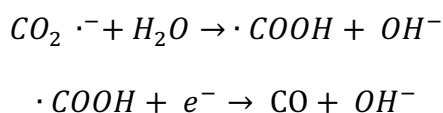
Figure 1-5. Possible structure of adsorbed CO_2 on surface metals.

The $\text{CO}_2\cdot^-$ radical anion adsorbed on the metal surface works like a nucleophilic reactant at the carbon atom or oxygen atom. Hence, in case of an oxygen coordination with the metal (e.g. Indium or Tin), the $\text{CO}_2\cdot^-$ takes a proton from a H_2O molecule at the nucleophilic carbon atom, producing $\text{HCOO}\cdot$ adsorbed. The next step is the subsequent reduction of $\text{HCOO}\cdot$ to HCOO^- at the electrode and its desorption [29]. The reaction steps can be write as:



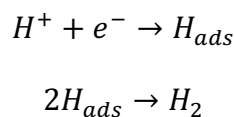
In the other hand, if the catalyst is an electrode made of 2nd group metals (e.g. Au, Ag, Zn), the carbon coordination on the surface is favored. It was demonstrated that the carbon

atom is strongly coordinated with the transition metal because a back donation from metal to CO₂, that stabilizes it by a strong charge transfer [30]. The H₂O, the electrophilic reagent, reacts with the oxygen of the adsorbed radical anion, forming CO and OH. Carbon coordination favors the protonation of oxygen and not carbon, preventing the formation of HCOO· and favoring the formation of ·COOH [29]. Subsequently, the radical ·COOH will be reduced to form CO, that is easily desorbed from the metal surface:



With the aim of proving the proposed reaction mechanism, it has been demonstrated that CO formation on a gold electrode does not depend on the pH of the electrolyte; hence the protons donor is not H⁺ but the H₂O molecule [21].

If the metal used strongly adsorbs CO on its surface (e.g., Pt, Ni, Fe, Ti), the main reaction at the electrode is the hydrogen evolution. This reaction is, in fact, the major side reaction that happens at the same time as CO₂ reduction.



Contrary to that seen with Au, Ag and Zn, a Cu electrode has a greater ability to adsorb CO on its surface. This property involves that Cu can further reduce CO to hydrocarbons and alcohols.

CH₄ formation occurs at more negative potential than C₂H₄, around -1.22 V and -1.12 V vs SHE respectively. Moreover, the formation of ethylene is favored by high electrolyte pH values [29]. As a consequence of these observations, it is conceivable that there are two different paths of reaction for the formation of methane and ethylene.

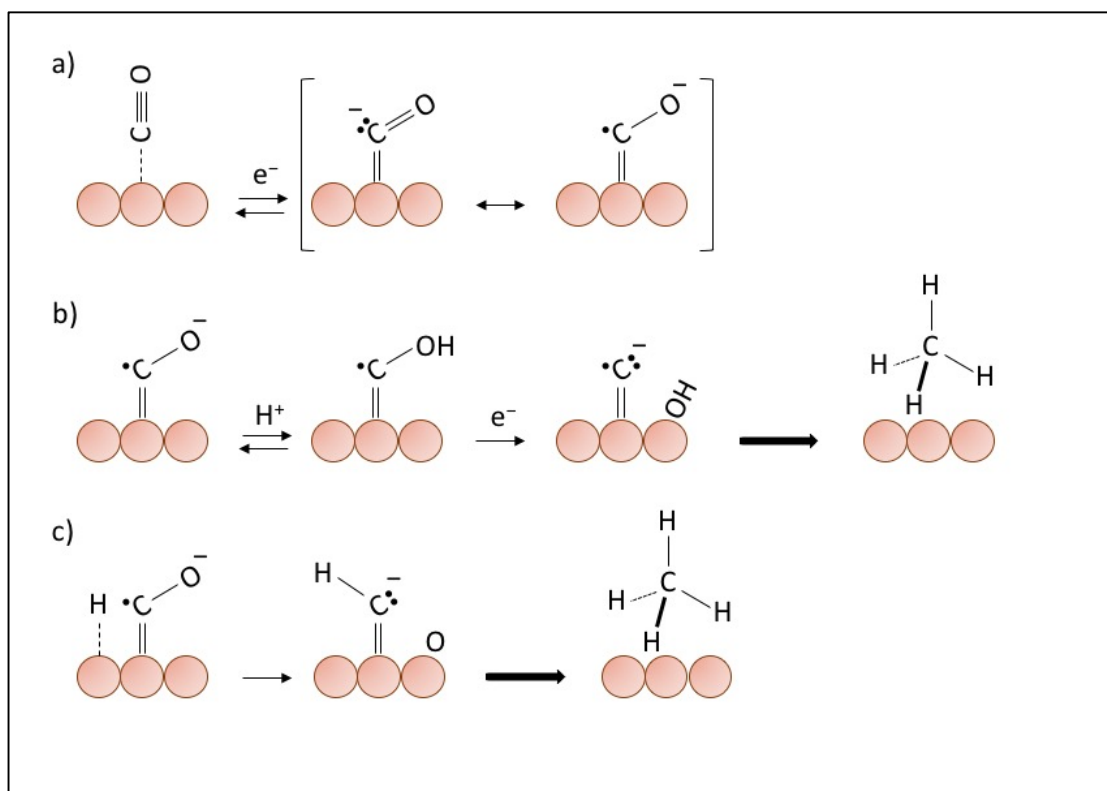


Figure 1-6. (a) proposed mechanism for initial electron transfer to adsorb CO as rate determining step, (b) (c) the reaction mechanisms assumed according with the observed transfer coefficient and reaction order. In orange, the Cu atoms.

As demonstrated by ab initio calculations, the Cu-C bond of the adsorbed CO anion radical on the surface of Cu has a double bond character [31]. After the formation of the CO anion radical (Figure 1-6 a), two reaction pathways can take place to obtain the methane production [32]:

- the first pathway provides an acid-base reaction to oxygen, with the formation of irreversible C-H bonds, leading to the production of CH_4 (Figure 1-6 b);
- the second pathway, on the other hand, proceeds with a radical CO anion reaction with an adsorbed hydrogen on the metallic surface, forming a radical C-H radical which evolves towards the formation of CH_4 (Figure 1-6 c).

The ethylene formation starts at a lower potential than methane, and as the rate determining step of electron transfer occurs, is possible to assume that there is the formation of some bond between two adjacent CO radical anions, followed by reduction to C_2H_4 (Figure 1-7 a). Alternatively, could happen another pathway to obtain the ethylene generation, where the first step is the reduction of the CO radical anion is to CH_2 , followed by a dimerization with another CH_2 or insertion of another CO and its final reduction (Figure 1.7 b) [32].

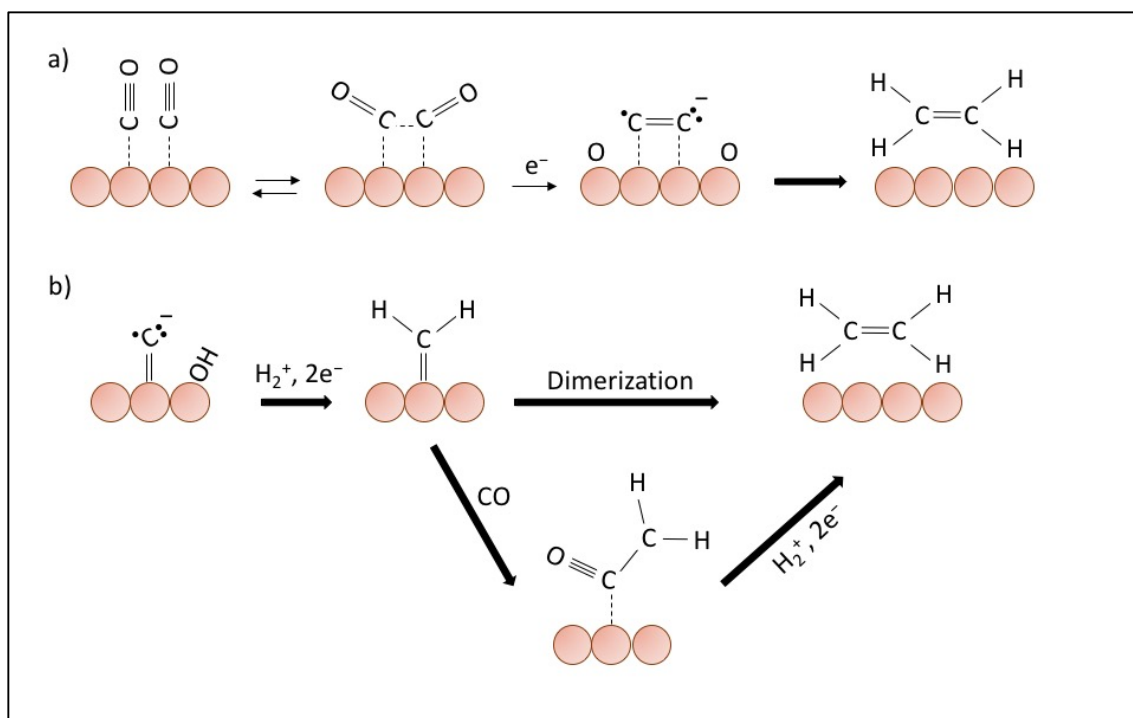


Figure 1-7. The assumed reaction mechanisms for the formation of ethylene. (a) "Prior association" of two adsorbed CO, (b) mechanisms with CH₂ formation. In orange, the Cu atoms.

Until now, the mechanism that allows the formation of C-H bond on Cu electrode, during the reaction between water or H⁺ with CO₂⁻ or CO, is not clear. In order to clarify this aspect, some experiments were carried out using different crystal faces of Cu.

Using crystal faces dominated by Cu (100), high faradic efficacy values towards ethylene were obtained, recording a relatively low overpotential. It is possible to explain this result by observing the reaction mechanism supposed in *Figure 1-7 (a)*, that shows a reaction intermediate with two CO molecules adsorbed on the copper surface. The formation of this intermediate requires interaction between the π orbitals of the CO molecules, which with vibrational motions accompany the oxygen atoms to interact with the copper surface. This transition state is easier to obtain with the right atomic arrangement that matches Cu (100) terrace surface [33].

On the contrary, the crystal faces dominated by Cu (111) show more negative potentials than Cu (100), favoring the methane production. Instead, the Cu (110) surfaces polarize to the most negative potential producing organic molecules with two or more carbon atoms such as acetic acid [34]. It follows that using a polycrystalline Cu the selectivity of the CO₂ reduction towards is distributed to many products [32].

1.4.5 Copper Alloy Electrocatalysts

As described in the previous section, among the electrode metals, only the Cu has the peculiarity of being able to produce hydrocarbons during the CO₂ reduction reaction at potential more negative than -1.0 V vs SHE. However, this extensive overpotential makes the process inefficient. For this reason, several modifications have been made to copper electrodes, as surface treatments (e.g. thermal or acid treatments) or modifying the surface of the electrode by inserting of heteroatoms.

Surface treatments are usually applied to remove surface contamination or surface irregularity caused by mechanical polishing. It was demonstrated that the product selectivity of a Cu electrode might be strongly affected by its surface treatments. Lately, a research group from Stanford has shown that an oxide derived copper (OD-Cu), could be a good precursor to obtain a catalyst with a high efficiency [35]. In particular, they show how an annealing treatment, followed by an electrochemical reduction of the oxide-derived copper, can produce a mixture of CO and HCOOH from CO₂ at low overpotential (-0.5 V vs RHE). Moreover, acceptable faradaic efficiency toward CO ($\approx 45\%$ F.E. in a potential ranging from -0.3 to -0.5 V vs RHE) was achieved, and an improvement of stability, at least several hours, compared to the rapid deactivation of polycrystalline Cu under identical conditions. The assumption carried forward to explain the improvement in CO faradaic efficiency, is that the formations of active sites can strongly bind the CO and suppress the hydrogen evolution reaction. These active sites are produced during the electrochemical reduction of copper oxide to the metallic state [36].

Subsequently, experiments were carried out with oxidized gold using electrochemical methods. As can be seen from Table 1.4, gold is a metal belonging to the 1st group identified by Y. Hori, so it has a high selectivity towards CO as well as a low overpotential. The results obtained show that oxide derived gold (OD-Au) has a metastable surface capable of accelerating the CO₂ reduction reaction, showing a remarkable catalytic activity. Besides, high faradaic efficacy values have been achieved toward CO ($\approx 99\%$) at very low overpotential (-0.35 V vs RHE) [37].

Similarly, nanocrystalline lead films prepared by electrochemical reduction of PbO₂ precursors, the results have shown a high faradaic efficiency toward CO₂ reduction to formate ($\approx 95\%$) at the low overpotential of -0.7 V vs RHE [38].

The presence of small amount of heteroatoms on the electrode surface could influence the selectivity of the CO₂ reduction reaction. There were used several methods to modify the metal surface, among these the electrochemical under potential (to obtain an atomic monolayer) or overpotential deposition are the easiest. For instance, the CO faradaic efficiency of pure Cu is 69%, while if the Cu surface is modified with a decoration of Cd or Pd, the faradaic efficiency becomes 82% and 0% respectively [29].

Several Cu-based alloys have been examined for the CO₂ reduction. Changes in the electronic structure and the crystallographic characteristics (including the introduction of vacancies and dislocations) are a combination that allows major changes in the selectivity of reaction products and reaction rates.

For example, Cu-Ni and Cu-Fe alloys, formed by electrochemical deposition, have shown a significant decline of CH₄ and C₂H₄ production, favoring the hydrogen evolution reaction when the coverage of Ni or Fe increase [39].

Other alloys catalysts as Cu-Pb, Cu-Zn, Cu-Cd have been studied; the first one showed a distributed selectivity toward CO and HCOOH; the alloys catalysts with Zn and Cd, instead, have shown a different behavior compared to elemental metals, with lower overpotential and greater distribution of faradic efficiencies [40].

A bimetallic Cu-Sn catalyst was developed by electrodeposition of tin on the Cu surface, and different thickness of that layer was investigated. The results obtained showed a high selectivity to make CO from CO₂ reduction (>90% F.E.) over a wide potential range (-0.4 to -0.8 V vs. RHE) with an excellent stability [41].

For a better understanding of the reaction mechanism, Kim D. *et al.* have investigated the CO₂ reduction activity of Au-Cu bimetallic nanoparticles in a monolayer platform, with the purpose to quantitatively compare the activity and selectivity of a different composition ratio of Au and Cu [42]. It was found a peak of activity for the Au₃Cu nanoparticles (93.1 times the only Cu nanoparticles), but they also identified the two most significant effects that may influence the selectivity of the CO₂ reduction reaction using a bimetallic catalyst: an electronic and a geometric effect. The electronic effect is due to the change in the electronic structure of a catalyst and influences the binding strength of intermediates that in case of transition metals depends on the *d*-bands interaction with the adsorbed species. An important role is also played by the geometric effect. Indeed, the presence of a different

atom at the adjacent atom, where the intermediate is adsorbed, can stabilize the adsorbed species allowing the further reaction step.

Reske R. *et al.* have investigated the thickness effects of Cu layers on Pt substrate on the activity and selectivity of CO₂ reduction [43]. They have shown that varying the Cu overlayers thickness is possible to control the product selectivity. This altered product distribution is recallable to the strain and electronic effects. While the electronic effect decreases with the increase in the atomic distance between the two elements until it disappears to a specific thickness of the Cu layer; on the contrary, the tensile strain effect remains unchanged even at great distances.

A Cu-In alloy catalyst was investigated following two different ways of preparation: electrochemical reduction of oxidized Cu and simultaneous deposition on In, otherwise by electrochemical reduction of a bimetallic mixed oxide (CuInO₂) used as a precursor. Both of them catalyzed the CO₂ reduction to CO with high faradaic efficiency toward CO, showing an exceptional stability of the electrode.

1.5 Key challenges for the electrochemical reduction of CO₂

As already mentioned above, the electrocatalytic reduction of CO₂ is a challenge and an opportunity for the academic world and industry. However, in order to reach the goal, it is necessary to take into account many aspects of both project and resource nature.

The catalyst properties are essential to optimize the desired process, which is why the main parameters investigated are catalytic activity, selectivity to a particular product, and electrode stability. As discussed above, a high overpotential is often a critical limit for some metals tested for the electrochemical reduction of CO₂. By reading Table 1.4, it can be noted that among the metals capable of producing formic acid or carbon monoxide, only Au and Pd have a less negative potential reduction of -1.3 V vs SHE, which is still very high if the goal is to use this technology in the future. Also, using the most promising metal, Cu requires a more negative reduction potential of Au, around -1.44 V vs SHE (at equal current density).

An important goal of the electrochemical reduction of CO₂ is to find a catalyst capable not only of transforming CO₂ with a low overpotential but also of minimizing parallel reactions, achieving high faradaic efficiency values for a single product. Mainly this is necessary because of the high separation costs of the products obtained. The most desired

products are formic acid and methane [44], the first is undoubtedly the easiest to produce, yet none of the catalysts developed to date has a high selectivity towards this desired product under normal pressure and temperature conditions.

One of the greatest obstacles is the deactivation of the catalyst due to the poisoning of the electrode surface. An important study by Hori et al. showed the main causes of the limited stability of the Cu electrode. The heavy metal impurities in the electrolyte solution; few organic substances in water; and some intermediate produced during the CO₂ reduction [45]. Furthermore, operating conditions, such as applied potential or current density, can affect the durability of the electrode. For example, it has been shown that the pulsed electrolysis method may decrease deactivation of the electrode, or pretreatment of a copper electrode by applying a potential can change the characteristics of the electrode surface and extend its durability [46].

Due to the stability of the CO₂ molecule, its reduction requires a great deal of energy. Consequently, the cost of electricity is an important parameter during the electroreduction process of CO₂. Moreover, it must be considered that renewable sources of energy must be used to avoid extra CO₂ emissions, which entails higher energy costs. Besides, chemical consumption is a cost that has to be taken into account for industrial development.

Energy consumption during the reduction process is high also because of the low catalytic activity of the catalysts. To overcome this problem, consider the cost of energy is critical to the development of this technology. Using fossil fuels as a primary source of electricity would certainly be cheaper, but this is a viable one if the objective is to control CO₂ emissions in the environment. To date, the lowest-cost, CO₂-free energy is the nuclear power, followed by wind energy that is expected to fall in price in the near future [47].

In conclusion, the properties of the catalyst are a key factor for CO₂ electroreduction technology. In order to achieve the set objectives, the three most important aspects of catalytic activity must be implemented: activity, selectivity and stability. In detail, it is necessary to obtain high faradaic efficiencies towards the desired products and low hydrogen evolution reaction.

1.6 Bibliography

- [1] INTERGOVERNMENTAL PANEL ON CLIMATE CHANGE, «Climate Change 2007: The Physical Science Basis.», IPCC WGI Fourth Assessment Report, 2007.
- [2] GISTEMP Team, «GISS Surface Temperature Analysis (GISTEMP)», NASA Goddard Institute for Space Studies, 2017. [Online]. Available: <https://data.giss.nasa.gov/gistemp/>. [Consultato il giorno 29 07 2017].
- [3] Hansen, J. R. Ruedy, M. Sato e K. Lo, «Global surface temperature change.», *Rev. Geophys.*, vol. 40, 2010.
- [4] J. Hansen, M. Sato, R. Ruedy, K. Lo, D. W. Lea e M. Medina-Elizade, «Global temperature change.», *PNAS*, vol. 103, n. 39, 2006.
- [5] J. T. Kiehl e K. E. Trenberth, «Earth's Annual Global Mean Energy Budget.», *Bulletin of the American Meteorological Society*, vol. 78, n. 2, 1997.
- [6] J. Qiao, Y. Liu, J. Zhang e S. Basu, *Electrochemical Reduction of Carbon Dioxide: Fundamentals and Technologies*, New York, London, Boca Raton: CRC, 2016.
- [7] Rackley e A. Stephen, *Carbon capture and storage*, Oxford: Butterworth-Heinemann Elsevier.
- [8] G. P. Peters, G. Marland, C. Le Quéré, T. Boden, J. G. Canadell e M. R. Raupach, «Rapid growth in CO₂ emissions after the 2008–2009 global nancial crisis», *Nature climate change*, vol. 2, n. 1, p. 2, 2012.
- [9] ENEA, «ENEA per lo studio dei cambiamenti climatici e dei loro effetti», Roma, 2007.
- [10] G. Burba e D. Anderson , *A brief practical guide to eddy covariance flux measurements: principles and workflow examples for scientific and industrial applications*, Li-Cor Biosciences, 2010.
- [11] P. Falkowski, R. J. Scholes, E. Boyle, J. Canadell, D. Canfield, J. Elser, N. Gruber, K. Hibbard, P. Högberg, S. Linder, F. T. Mackenzie, B. Moore III, T. Pedersen, Y. Rosenthal, S. Seitzinger, V. Smetacek e W. Steffen, «The Global Carbon Cycle: A Test of Our Knowledge of Earth as a System.», *Science*, vol. 290, n. 5490, pp. 291-296, 2000.
- [12] M. C. Colin Baird, *Chimica Ambientale*, Zanichelli, 2013.
- [13] Halmann, M. Martin e M. Steinberg, *Greenhouse gas carbon dioxide mitigation: science and technology*, CRC press, 1998.
- [14] Cooper e I. Andrew, «Polymer synthesis and processing using supercritical carbon dioxide.», *Journal of Materials Chemistry*, vol. 10, pp. 207-234, 2000.
- [15] Manzer e E. Leo, «CO₂ Emission Reductions: An Opportunity for New Catalytic Technology.», *ACS Symposium series*, vol. 809, pp. 39-52, 2002.
- [16] Song e Chunshan, «Global Challenges and strategies for control, conversion and utilization of CO₂ for sustainable development involving energy, catalysis, adsorption and chemical processing.», *Catalysis Today*, vol. 115, pp. 2-32, 2006.

- [17] J. K. Stolaroff, D. W. Keith e G. V. Lowry, «Carbon Dioxide Capture from Atmospheric Air Using Sodium Hydroxide Spray.», *Environmental Science & Technology*, vol. 42, n. 8, p. 2728–2735, 2008.
- [18] M. Bentham e G. Kirny, «CO₂ Storage in Saline Aquifers.», Oil & Gas Science and Technology, Notthigham, 2005.
- [19] A. Di Benedetto e M. Aresta, «Artificial carbon sinks: utilization of carbon dioxide for the synthesis of chemicals and technological applications.», in *Greenhouse Gas Sinks*, CABI Books, 2007, p. 98–114.
- [20] A. S. Agarwal, Y. Zhai, D. Hill e N. Sridhar, «The Electrochemical Reduction of Carbon Dioxide to Formate/Formic Acid: Engineering and Economic Feasibility.», *ChemSusChem*, vol. 4, p. 1301 – 1310, 2011.
- [21] Y. Hori, «Electrochemical CO₂ Reduction on Metal Electrodes.», *Modern aspects of Electrochemistry*, n. 42, 2008.
- [22] H. J. Freund e M. W. Roberts, «Surface chemistry of carbon dioxide.», *Surface Science Reports*, vol. 25, pp. 225-273, 1996.
- [23] H. Noda, S. Ikeda, Y. Oda, K. Imai, M. Maeda e K. Ito, «Electrochemical reduction of carbon-dioxide at various metal-electrodes in aqueous potassium hydrogen carbonate solution.», *Bulletin of the Chemical Society of Japan*, vol. 63, n. 9, p. 2459–2462, 1990.
- [24] J. J. Wu, P. P. Sharam, B. H. Harris e X. D. Zhou, «Electrochemical reduction of carbon dioxide: IV Dependence of the faradaic efficiency and current density on the micro-structure and thickness of tin electrode.», *Journal of Power Sources*, vol. 258, p. 189–194, 2014.
- [25] J. J. Wu, F. G. Risalvato, S. G. Ma e X. D. Zhou, «Electrochemical reduction of carbon dioxide III. The role of oxide layer thickness on the performance of Sn electrode in a full electrochemical cell.», *Journal of Materials Chemistry A*, vol. 2, n. 6, p. 1647–1651, 2014.
- [26] Y. Ougitani, T. Aizawa, N. Sonoyama e T. Sakata, «Temperature dependence of the probability of chain growth for hydrocarbon formation by electrochemical reduction of CO₂.», *Bulletin of the Chemical Society of Japan*, vol. 74, n. 11, p. 2119–2122, 2001.
- [27] J. E. Huheey, E. A. Keiter e R. L. Keiter, *Inorganic Chemistry: Principles of Structure and Reactivity*, Pearson Education, 2006.
- [28] Y. Hori, H. Wakebe, T. Tsukamoto e O. Koga, «Electrocatalytic process of CO selectivity in electrochemical reduction of CO₂ at metal electrodes in aqueous media», *Electrochimica Acta*, vol. 39, n. 11-12, pp. 1833-1839, 1994.
- [29] W. Li, «Electrocatalytic Reduction of CO₂ to small Organic Molecule Fuels on Metal Catalysts», in *Advances in CO₂ Conversion and Utilization*, Washington, American Chemical Society, 2010, pp. 55-76.
- [30] S. Sakaki, «An ab Initio MO/SD-CI Study of Model Complexes of Intermediates in Electrochemical Reduction of CO₂ Catalyzed by NiC12(cyclam)», *Journal of American Chemical Society*, vol. 114, pp. 2055-2062, 1992.
- [31] K. Watanabe, U. Nagashima e H. Hosoya, «An ab initio study of adsorbed carbon monoxide on a metal electrode by cluster model», *Applied Surface Science*, vol. 75, pp. 121-124, 1994.

- [32] M. Gattrell, N. Gupta e A. Co, «A review of the aqueous electrochemical reduction of CO₂ to hydrocarbons at copper», *Journal of Electroanalytical Chemistry*, vol. 594, pp. 1-19, 2006.
- [33] Y. Hori, R. Takahashi, O. Koga e N. Hoshi, «Electrochemical reduction of carbon dioxide at various series of copper single crystal electrodes», *Journal of Molecular Catalysis A: Chemical*, vol. 199, pp. 39-47, 2003.
- [34] I. Takahashi, O. Koga, N. Hoshi e Y. Hori, «Electrochemical reduction of CO₂ at copper single crystal Cu(S)-[n(111)×(111)] and Cu(S)-[n(110)×(100)] electrodes», *Journal of Electroanalytical Chemistry*, vol. 533, pp. 135-143, 2002.
- [35] C. W. Li e M. W. Kanan, «CO₂ Reduction at Low Overpotential on Cu Electrodes Resulting from the Reduction of Thick Cu₂O Films.», *Journal of American Chemical Society*, vol. 134, p. 7231–7234, 2012.
- [36] A. Verdaguier-Casadevall, C. W. Li, T. P. Johansson, S. B. Scott, J. T. McKeown, M. Kumar, I. E. Stephens, M. W. Kanan e I. Chorkendorff, «Probing the active surface sites for CO reduction on oxide-derived copper electrocatalysts», *Journal of the American Chemical Society*, vol. 137, n. 31, p. 9808–9811, 2015.
- [37] Y. Chen, C. W. Li e M. W. Kanan, «Aqueous CO₂ Reduction at Very Low Overpotential on Oxide-Derived Au Nanoparticles.», *Journal of The American Chemical Society*, vol. 134, pp. 19969-19972, 2012.
- [38] C. H. Lee e M. W. Kanan, «Controlling H⁺ vs CO₂ Reduction Selectivity on Pb Electrodes», *ACS Catalysis*, vol. 5, n. 1, p. 465–469, 2015.
- [39] T. Yamamoto, D. Tryk, A. Fujishima e H. Ohata, «Production of syngas plus oxygen from CO₂ in a gas-diffusion electrode-based electrolytic cell», *Electrochimica Acta*, vol. 47, n. 20, pp. 3327-3334, 2002.
- [40] M. Watanabe, M. Shibata, A. Kato, M. Azuma e T. Sakata, «Design of Alloy Electrocatalysts for CO₂ Reduction III . The Selective and Reversible Reduction of Formula on Cu Alloy Electrodes», *Journal of The Electrochemical Society*, vol. 138, n. 11, 1991.
- [41] S. Sarfraz, A. T. Garcia-Esparza, A. Jedidi, L. Cavallo e K. Takanabe, «Cu-Sn Bimetallic Catalyst for Selective Aqueous Eletroreduction of CO₂ to CO.», *ACS Catalysis*, vol. 6, pp. 2842-2851, 2016.
- [42] D. Kim, J. Resasco, Y. Yu, A. M. Asiri e P. Yang, «Synergistic geometric and electronic effects for electrochemical reduction of carbon dioxide using gold-copper bimetallic nanoparticles.», *Nature Communications*, vol. 5, pp. 1-8, 2014.
- [43] R. Reske, M. Duca, M. Oezaslan, K. J. P. Schouten, M. T. M. Koper e P. Strasser, «Controlling Catalytic Selectivity during CO₂ Electroreduction on Thin Cu Metal Overlayers-», *The Journal of Physical Chemistry Letters*, vol. 4, pp. 2410-2413, 2013.
- [44] J. Qiao, Y. Liu, F. Hong e J. Zhang, «A review of catalysts for the electroreduction of carbon dioxide to produce low-carbon fuels.», *Chemical Society Reviews*, vol. 2, 2014.
- [45] Y. Hori, H. Konishi, T. Futamura, A. Murata, O. Koga, H. Sakurai e K. Oguma, «“Deactivation of copper electrode” in electrochemical reduction of CO₂.», *Electrochimica Acta*, vol. 50, n. 27, pp. 5354-5369, 2005.
- [46] J. Yano, T. Morita, K. Shimano, Y. Nagami e S. Yamasaki, «Selective ethylene formation by pulse-mode electrochemical reduction of carbon dioxide using copper and

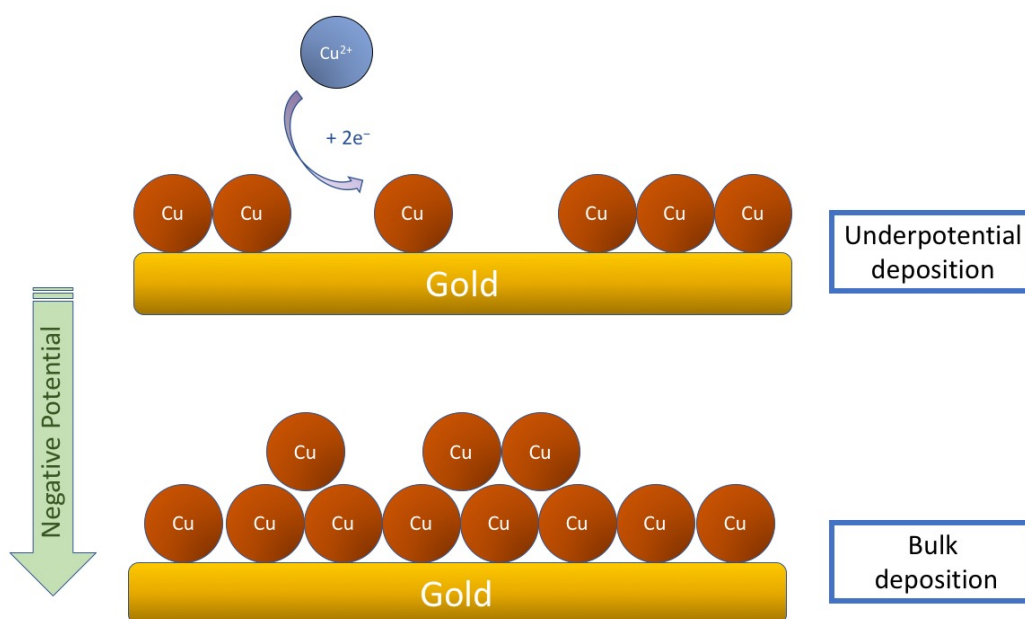
copper-oxide electrodes.», *Journal of Solid State Electrochemistry*, vol. 11, n. 4, p. 554–557, 2007.

- [47] M. Fan e J. Qiao, «Challenges and perspectives of CO₂ Electroreduction.», in *Electrochemical Reduction of Carbon Dioxide: Fundamentals and Technologies.*, vol. 11, CRC Press, 2016, pp. 357-369.

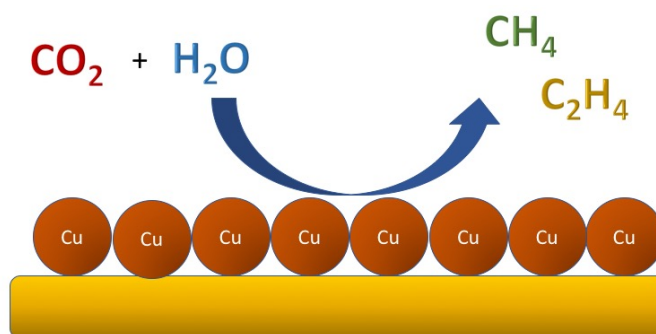
Chapter 2

2 CO₂ Electroreduction on Au/Cu electrode

Initially, the research work was focused on the electrochemical deposition of different thicknesses layer of copper on a gold substrate.



Subsequently, the working electrodes, thus obtained, were used as electrocatalysts for the reduction of CO₂ in an aqueous solution. The objective of the work was to get a selective production of methane and ethylene from CO₂ reduction.



2.1 Results and discussions

2.1.1 Cu on Au deposition strategy

In order to construct an experimental procedure with certain operating conditions, an experimental study of the system consisting of the gold electrode and the electrode deposition solution was conducted.

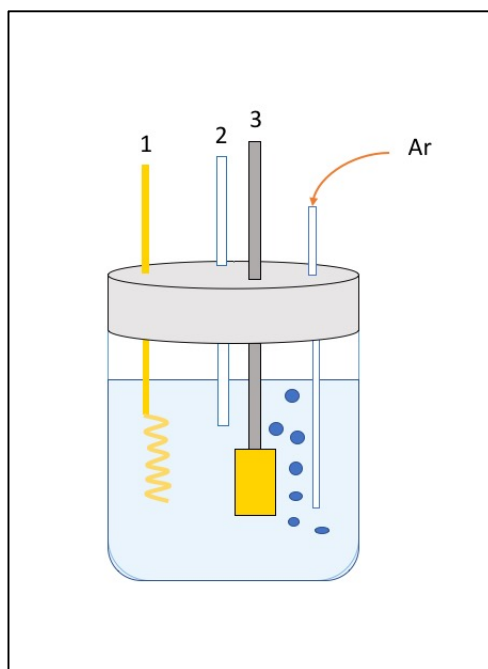


Figure 2-1. Schematic representation of the electrolytic cell used for the study of the redox deposition system. (1) Au spiral counter electrode; (2) Hg/Hg₂Cl₂ reference electrode; (3) Au sheet as working electrode; 50 mM H₂SO₄ and 5 mM CuSO₄, Argon saturated electrolytic solution.

A previously prepared gold electrode was used as working electrode, in a three electrodes cell (*Figure 2-1*) filled with 45 mL of 50 mM H₂SO₄ and 5 mM CuSO₄ solution. A gold wire was the counter electrode, and a Hg/Hg₂Cl₂ electrode was used as reference. After saturating the solution bubbling argon gas, the electrochemical system was investigated at a potential range from -0.5 to 1.8 V vs RHE with a scan rate of 10 mV s⁻¹ by cyclic voltammetry. Subsequently, in order to detect the redox potential for the underpotential deposition of Cu on Au, a cyclic voltammetry was conducted in a potential window between 0.4 and 0.8 vs RHE with a scan rate of 10 mV s⁻¹.

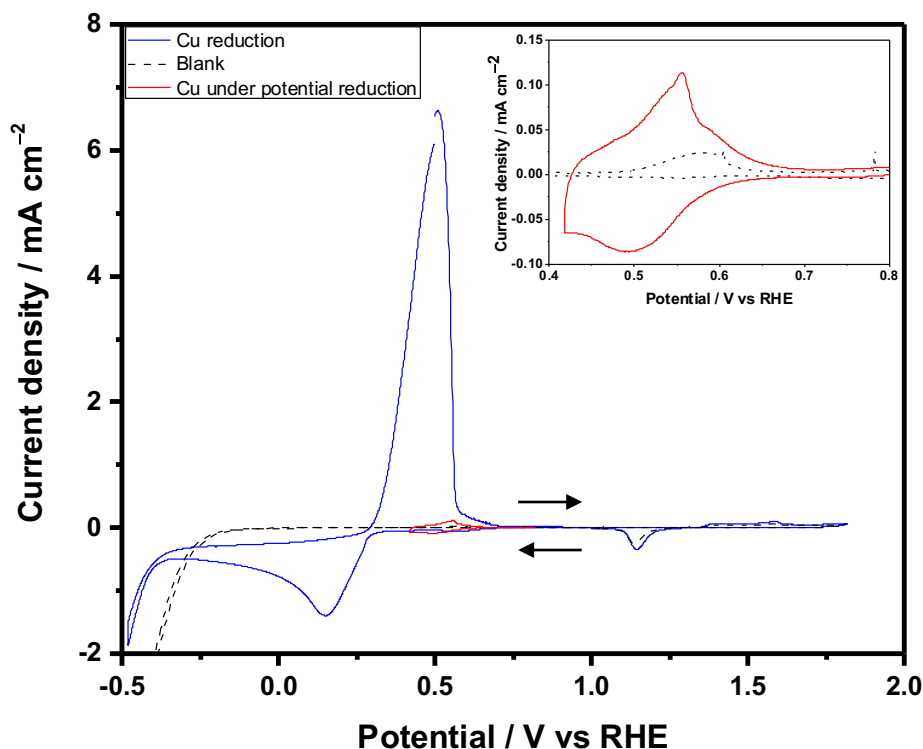


Figure 2-2. Deposition and dissolution of Cu on the gold polycrystalline substrate in 50 mM H_2SO_4 + 5 mM $CuSO_4$. CV of bulk deposition of Cu on Au (blue line). CV of monolayer deposition (red line). Blank acquisition in 50 mM H_2SO_4 solution (black-dash line).

In *Figure 2-2* the voltammograms acquired are shown. Observing the blue line, we can locate the peak relative to the copper reduction from Cu^{2+} to Cu, in a range of potential between -0.25 and 0.27 V vs RHE, with an anodic peak potential of 0.23 V vs RHE. Moreover, the reduction and oxidation peaks of gold are visible around 1.20 and 1.55 V vs RHE respectively [48]. Instead, observing the red line, we can locate the peak relative to the copper under potential reduction from Cu^{2+} to Cu, in a range of potential between 0.41 and 0.60 V vs RHE, with an anodic peak potential of 0.5 V vs RHE.

In order to obtain a full Cu monolayer deposition, a linear sweep voltammetry from 0.92 V to 0.40 V vs RHE (scan rate 10 mV s^{-1}) was carried out (*Figure 2-3*). For each deposition, the electrode was pretreated applying a potential of 0.92 V vs RHE for 20 seconds in the same solution.

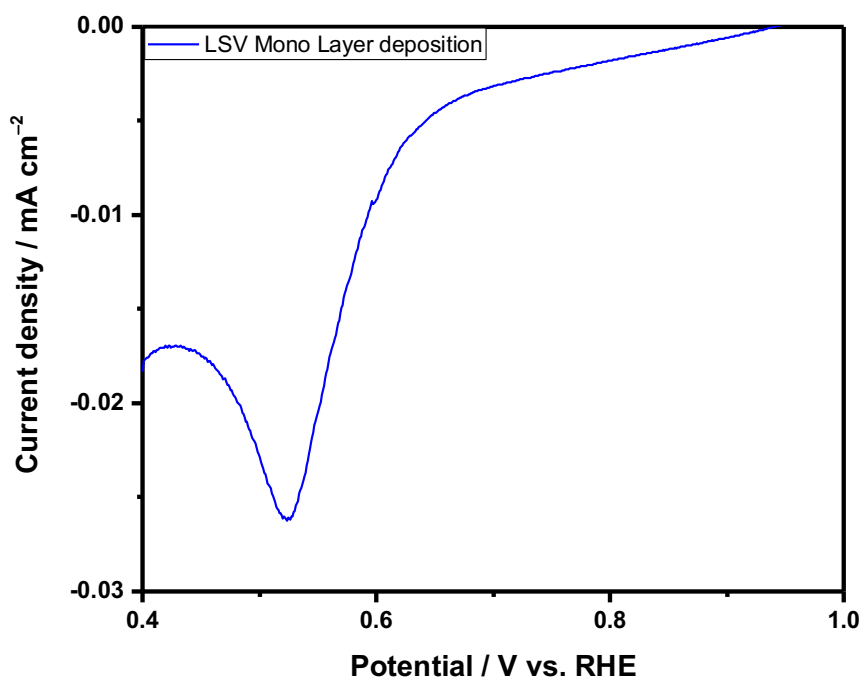


Figure 2-3. Deposition of a Cu monolayer using a linear sweep voltammetry from 0.92 to 0.40 V vs RHE.

The coulombometric charge value measured was close to $485 \mu\text{C cm}^{-2}$. This value is not very different from what it is indicated as the theoretical value necessary for the deposition of a full monolayer of copper on gold, that is $440 \mu\text{C cm}^{-2}$. The reason of a higher amount of transferred charge is attributed to the polycrystalline nature of the electrode surface and a partial coadsorption of sulphate ions in the solution. However, according to previous study, the net amount contribution of the sulphate ions adsorbed to the total charge could be negligible [49].

In order to check if the monolayer deposition has happened, an XPS analysis was performed. After depositing copper on gold, the electrode was gently washed by immersing it in Milli-Q water for a few minutes. Subsequently, a sample with a surface of about 250 mm^2 was cut and analysed by XPS.

The XPS spectra of the Cu 2p core level of Cu/Au surface shows two intense peaks at 934.8 and 954.6 eV, which correspond to Cu 2p_{3/2} and Cu 2p_{1/2} peaks respectively. These peaks were attributed to Cu^I oxide and metal Cu surface. At binding energy value of 943.4 eV is visible a weak satellite peak, relative to the copper Cu(I), because of the partially filled Cu 3d⁹ shells.

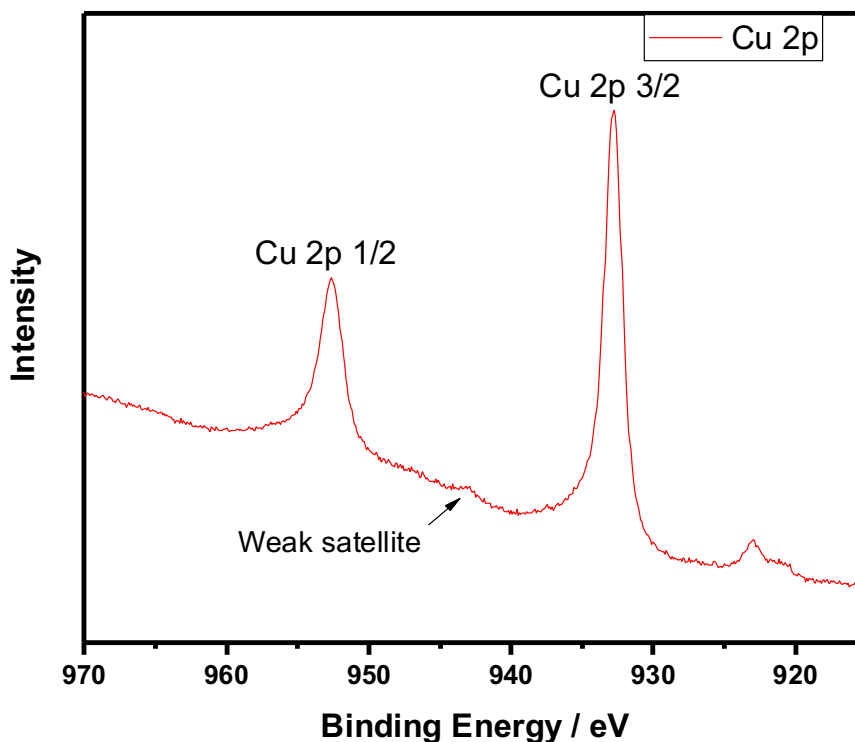


Figure 2-4. XPS spectra of Cu 2p for the Cu monolayer on Au substrate.

Besides, the XPS regions for Au and S were analyzed (to estimate the sulphate co-absorption). However, no visible peaks in both regions indicate the absence of the two elements on the surface. This result, in addition to the linear sweep voltammetry shown previously, confirms the deposition of a full Cu monolayer on Au substrate, without sulphate.

For the bulk copper deposition, a 50 mM of H₂SO₄ and 10 mM of CuSO₄ solution purged with Argon was prepared as the electrolyte and the same electrochemical cell configuration described above was used. During an electrochemical deposition, the amount of metal that is reduced to the cathode is directly proportional to the charge passing through the cathode itself (first Faraday's law). Then, if the potential is maintained constant, the deposition time determines the amount of copper deposited on the electrode's surface as in equation 2.1.

$$m = \frac{M \cdot q}{z \cdot F} \quad 2.1$$

where m (g) is the total mass deposited on the cathode, M ($g \text{ mol}^{-1}$) is the molar mass of the deposited substance, q (C) is the total electrical charge associated with charge carriers

crossing the solution, z is the charge value of the ion (charge transferred by ion) and F is the Faraday constant (equal to 96485 C/mol).

However, if in the previous equation we consider that $m = \rho_{Cu} \cdot V$ (where ρ_{Cu} is the density of copper and V is the volume of the copper layer) and $V = d \cdot A_{electr.}$ (where d is the copper layer thickness and $A_{electr.}$ is the surface area of the electrode) then the equation 2.1 becomes:

$$d = \frac{M \cdot q}{z \cdot F \cdot \rho_{Cu} \cdot A_{electr.}} \quad 2.2$$

The equation 2.2 explicates as the thickness of the deposited metal depends on constant values such as the density and molecular weight of the metal, its ionic charge, the Faraday constant and the electrode area. Therefore, the only experimentally controllable parameter, during the electrochemical deposition process, is the transferred charge q . The total charge transferred q is given by the integral of the electric current $I(t)$:

$$q = \int_0^{\Delta t} I(t) dt \quad 2.3$$

For this reason, chronoamperometry was used as a potential controlled technique for electrochemical deposition. In fact, the transferred charge is easy to obtain, calculating the area under the I vs t curve that is shown as the response from the potentiostat. Therefore, rearranging equation 2.1 and explaining q , the charge required to deposit a copper layer of 5 or 10 nm on a gold electrode of 1 cm² was calculated:

$$q = \frac{d \cdot \rho_{Cu} \cdot A_{electr.} \cdot z \cdot F}{M} \quad 2.4$$

Performing a chronoamperometry of 20 seconds and applying a potential of -0.18 V vs RHE, the time values relative at the charge transferred needed were obtained. In Table 2.1 the layer thickness and the respective charge transferred and deposition time are shown.

Table 2.1. Electrochemical deposition parameters for the bulk copper layer on gold substrate.

$\rho_{Cu} (g \cdot cm^{-3})$	$M (g \cdot mol^{-1})$	$F (C \cdot mol^{-1})$	z	$A_{electr.} (cm^2)$
8.92	63.55	96485	2	1
Thickness (nm)	Charge (mC)^a		Time (s)^b	
5	13.54		4	
10	27.09		11	

a) Calculated from equation 2.4

b) Experimental values

In conclusion, the electrochemical deposition of bulk Cu layer on gold was carried out using a chronoamperometry experiment, applying a constant potential of -0.18 V vs RHE (chosen using the blue cycle voltammogram in *Figure 2-2*) for a time of 4 or 11 seconds in order to obtain a 5 or 10 nm thick layer respectively.

2.1.2 Electrochemical CO₂ reduction measurements

Chronoamperometry was performed on the copper monolayer on gold electrode (Au/Cu_{ML}), and on the bulk copper layers on gold electrodes with a thickness of 5 nm or 10 nm (Au/Cu_{5nm} and Au/Cu_{10nm}), in order to study the reduction of CO₂ for 1 hour applying various potential in the range between -0.8 and -1.4 V vs RHE. H₂, CO and HCOOH were the only detected reaction products by gas chromatography and HPLC. The Cu_{ML} was the result of a linear sweep voltammetry deposition, whereas the 5 and 10 nm Cu layers were the results of a chronoamperometry deposition at constant potential applied. To compare the results obtained, a gold electrode for electrochemical measurements was also used (Au blank).

Before each electrochemical measurement, an induction period of 30 minutes was conducted in open circuit voltage, that was necessary because of the filling of the dead-space volume of the electrochemical cell. After this induction period, the potential was applied, and after around 10 minutes a stable concentration of the gas products for all the electrodes was observed. When the steady-state conditions were reached, the currents observed were constant, and the average faradaic efficiency was determined at this point.

Figure 2-5 show a comparison of the total geometric current density as a function of the potential applied for the Au blank, Au/Cu_{ML}, Au/Cu_{5nm} and Au/Cu_{10nm} electrodes. At

low overpotential, the current densities of the four different materials were very similar, however, at the more negative potential, not only does the current density increase for each electrode, but also the difference in current values is greater among them. The current density of Au/Cu_{5nm} and Au/Cu_{10nm} was lower than that of only Au substrate, showing that the overall activity decreased when more copper was present on the gold electrode surface.

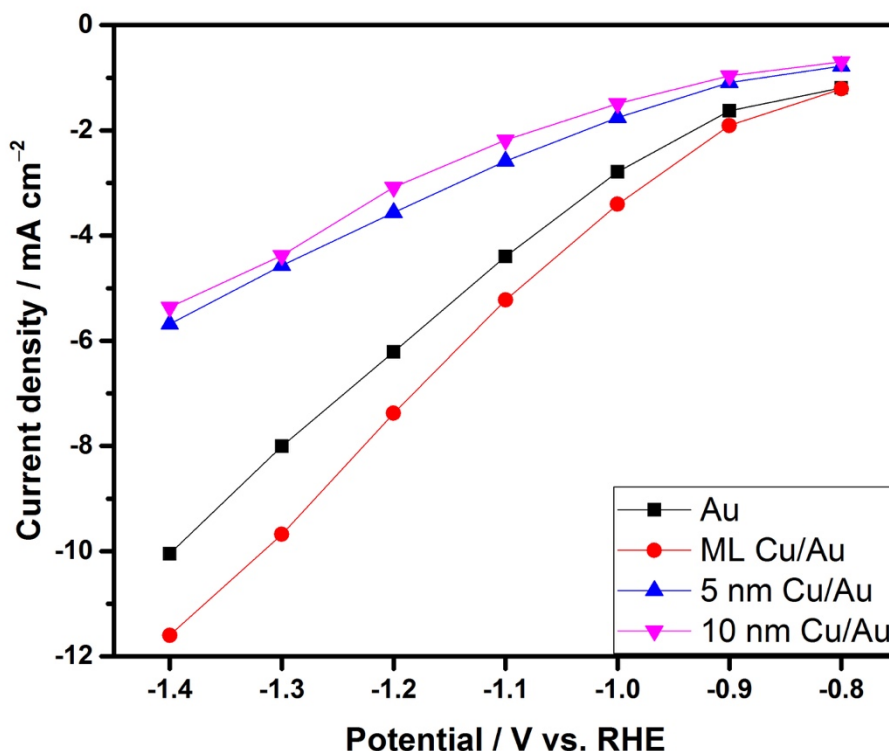


Figure 2-5. Current density comparison among Au, Au/Cu_{ML}, Au/Cu_{5nm} and Au/Cu_{10nm} electrodes (0.1 M KHCO₃, pH 6.8, saturated CO₂).

Contrariwise, Au/Cu_{ML} electrode shows a opposite trend. The current density recorded at the lower potential of -1.4 V vs RHE is double of that recorded with the other two bulk copper modified electrodes, indicating a greater overall activity if the copper layer is thinner. Nevertheless, the most significant outcome obtained from the data of this experiment is the significant increase in the current density in the presence of a copper monolayer on the gold surface compared to a bare gold electrode.

The Au sample (Figure 2-6) showed 67% of CO faradaic efficiency at -0.8V vs RHE, which decreases gradually to 9% at -1.4 V vs RHE. In contrast, the H₂ faradaic efficiency monotonically increased with increasing overpotential using Au electrode, reaching 49% of faradaic efficiency at -1.4 V vs RHE starting from a value of 23% at -0.8 V vs RHE.

The same trend was observed for the HCOOH faradaic efficiency, in fact, it was $\approx 3\%$ at -0.8 V vs RHE then increases to 28% at -1.3 V vs RHE and again decrease to 22% at -1.4 V vs RHE. The trend of these products for Au electrode is in accordance with the literature [50]. From the data obtained it can be seen that at lower potentials the hydrogen evolution reaction becomes dominant, going to the detriment of CO_2 reduction. The overall products faradaic efficiency is not 100% , that probably because of some reduction process of gold itself or the production of not detectable products. About this is worth noting that the overall faradaic efficiency increased going to lower potential, but at -1.4 V vs RHE showed a sudden decrease, ascribable at another product not detected.

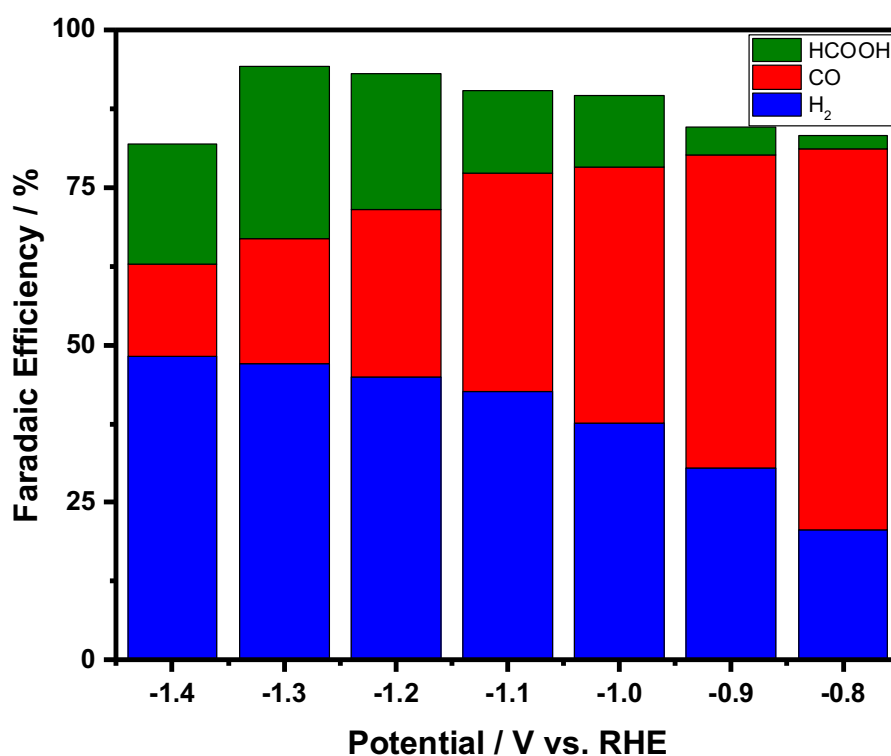


Figure 2-6. Faradaic efficiency analysis of Au electrode at applied potentials for H_2 (blue), CO (red) and HCOOH (green). The Faradaic efficiency showed is an average value calculated at the steady-state current and product concentration (0.1 M KHCO_3 , pH 6, saturated CO_2).

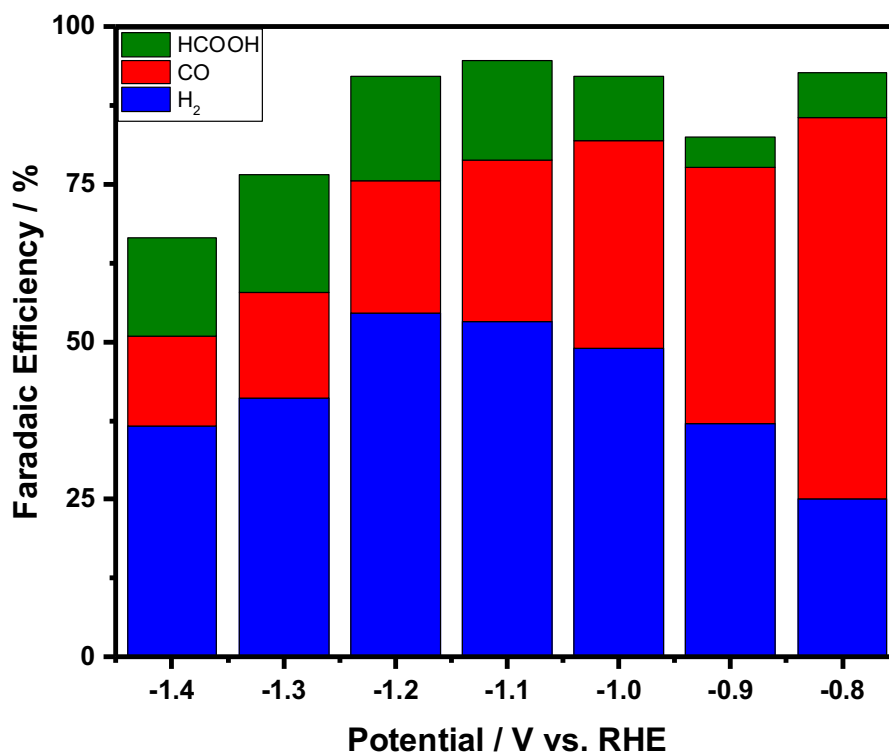


Figure 2-7. Faradaic efficiency analysis of Au/Cu_{ML} electrode at applied potentials for H₂ (blue), CO (red) and HCOOH (green). The Faradaic efficiency showed is an average value calculated at the steady-state current and product concentration (0.1 M KHCO₃, pH 6.8, saturated CO₂).

The Au/Cu_{ML} sample (Figure 2-7) showed 64% of CO faradaic efficiency at -0.8 V vs RHE, which decreases gradually to 11% at -1.4 V vs RHE. The H₂ faradaic efficiency monotonically increased from a value of 25% at -0.8 V vs RHE, then reached 53% with increasing overpotential until -1.2 V vs RHE, and again decreased to 37% of faradaic efficiency at -1.4 V vs RHE. Instead, the HCOOH faradaic efficiency observed was 7% at -0.8 V vs RHE then increases to 14% at -1.1 V vs RHE and remained constant until -1.4 V vs RHE. As seen above for the Au sample, the overall products faradaic efficiency is not 100%, and its decrease at lower potentials than -1.1 V vs RHE is considerable. In fact, the overall products faradaic efficiency decreases from 94% to 68% in a range of 0.4 V, that means that the 26% of the current, at least, formed other products not detected. The formation of other products such as methanol or ethanol required more electrons than carbon monoxide or formic acid formation. Consequently, the formation of different products explains the higher current density observed in Figure 2-5 for the Au/Cu_{ML} sample.

The faradaic efficiencies for the Au/Cu_{5nm} and Au/Cu_{10nm} samples between -0.8 and -1.4 V vs RHE are compared in *Figure 2-8* and *Figure 2-9*, respectively. Both of them show an increase of H₂ faradaic efficiency from $\approx 25\%$ at -0.8 V vs RHE to $\approx 40\%$ at -1.3 V vs RHE, but if in case of the Au/Cu_{10nm} sample the H₂ Faradaic efficiency does not change between -1.3 and -1.4 V vs RHE, on the other hand, in the case of the Au/Cu_{5nm} sample a decrease was observed. The trends for CO and HCOOH faradaic efficiencies is similar for both the samples: the CO faradaic efficiency slightly decreases from -0.8 to -1.4 V vs RHE; whereas the HCOOH faradaic efficiency slightly increases at higher overpotentials. The Au/Cu_{5nm} sample showed a very high HCOOH faradaic efficiency, 36% at -0.8 V vs RHE, however that value is incoherent with the overall trend.

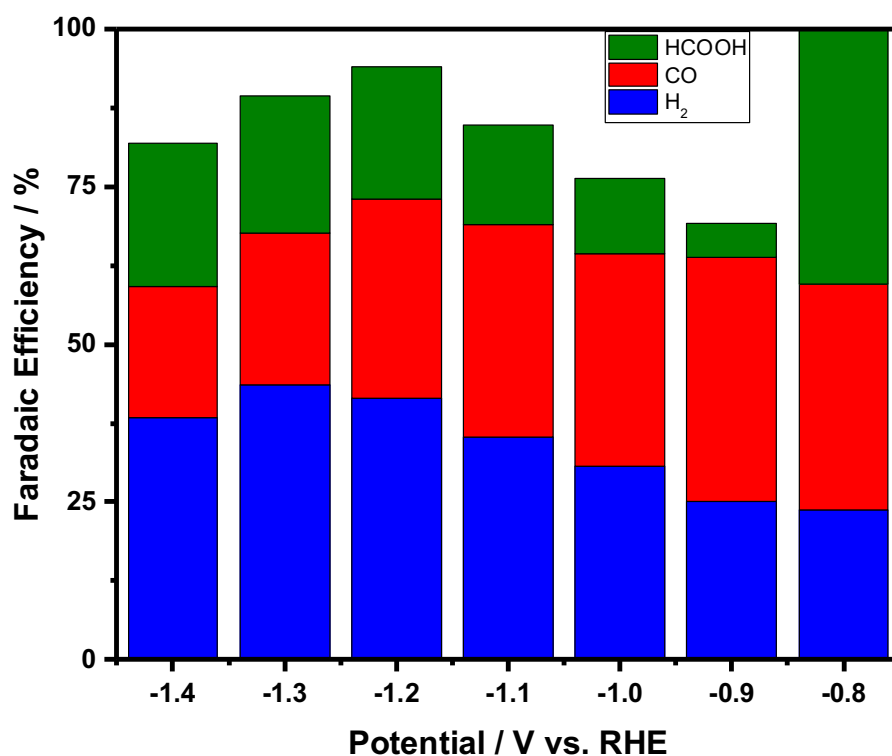


Figure 2-8. Faradaic efficiency analysis of the Au/Cu_{5nm} electrode at applied potentials for H₂ (blue), CO (red) and HCOOH (green). The Faradaic efficiency showed is an average value calculated at the steady-state current and product concentration (0.1 M KHCO₃, pH 6.8, saturated CO₂).

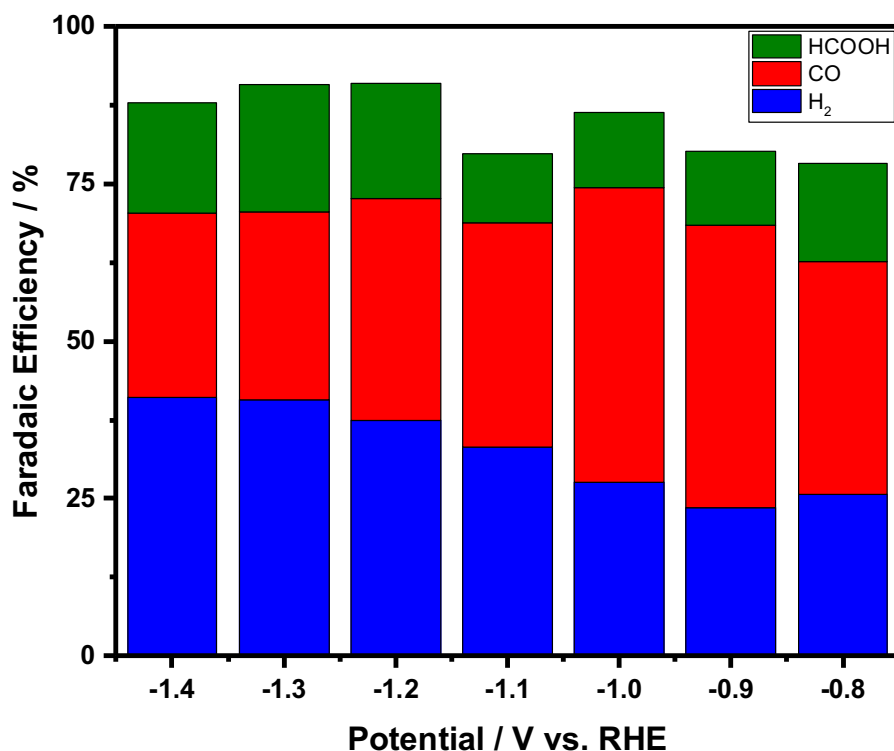


Figure 2-9. Faradaic efficiency analysis of the Au/Cu_{10nm} electrode at applied potentials for H₂ (blue), CO (red) and HCOOH (green). The Faradaic efficiency showed is an average value calculated at the steady-state current and product concentration (0.1 M KHCO₃, pH 6.8, saturated CO₂).

Moreover, the Au/Cu_{5nm} sample showed an overall faradaic efficiency similar to that observed from the Au/Cu_{ML} sample, but the difference that is lower even at relative high potential range between -0.9 and -1.1 V vs RHE. On the other hand, the hydrogen evolution reaction was less dominant compared to the results observed with the Au and Au/Cu_{ML} samples, to the advantage of CO₂ reduction.

All the samples described above did not produce significant amounts of methane and ethylene. Small quantities, $\approx 0.6\%$ and $\approx 1\%$ of faradaic efficiencies for CH₄ and C₂H₄ respectively, at lower potentials for Au/Cu_{ML} and Au/Cu_{5nm} samples were detected.

2.2 Experimental section

2.2.1 Materials

Au sheets of 0.2 mm thickness (99.95% purity) and an Au wire of 1.0 mm in diameter were purchased from Nilaco Corporation, Japan. An Ag/AgCl and a Hg/Hg₂Cl₂ reference electrodes saturated in KCl solution were obtained from BAS Corporation, Japan. High purity CO₂ gas cylinder (99.9999%) was bought from AHG industrial gases, Saudi Arabia.

The following chemicals were obtained from Sigma-Aldrich:

- Copper (II) sulfate pentahydrate (CuSO₄ · 5H₂O, 99.999% trace metal basis);
- Potassium bicarbonate (KHCO₃, 99.99%);
- Sulfuric acid (H₂SO₄, 99.999% trace metal basis);
- Hydrochloric acid (HCl, ACS reagent, assay 36.5-38.0%).

2.2.2 Instruments

For all electrochemical measurements, including electrodeposition and CO₂ reduction experiments, a BioLogic VMP3 potentiostat was used.

Gas products were quantified using a VARIAN 450-GC gas chromatograph equipped with a 5 Å MolSieve column and two detectors: a thermal conductivity detector (TCD) and a flame ionization detector (FID) for hydrocarbons. Furthermore, a high-performance liquid chromatograph (HPLC) from Agilent Technologies equipped with an ICE-Coregel 87-H3 column and 1260 Infinity Variable Wavelength Detector for the detection of HCOOH.

A 3400 KRATOS AMICUS/ESCA was used for the X-ray photoelectron spectroscopy (XPS), with an un-monochromatized Al-anode K α X-ray source (1486.6 eV) activated at 15 mA and 10 kV. To calibrate the binding energy of diffractogram obtained was used the adventitious C 1s spectra with a reported binding energy of 284.8 eV.

2.2.3 Preparation on the Au substrate

The pristine Au sheet with 0.2 mm of thickness (99.95% purity) was cut into 1×2 cm² plates, plenty washed with Milli-Q water, sonicated for 3 minutes in acetone and subsequently in ethanol. After removal from ethanol, the plates were placed under nitrogen flow until a dry surface was obtained. The single gold plate was connected to a stainless-

steel rod using a screw, and the top was wrapped with a Teflon tape, leaving only an area of 1 cm^2 exposed as working electrode.

After that, in order to obtain a homogeneous surface, the as prepared Au electrode was cleaned following an electro polishing method described in the literature [51]. The Au electrode was immersed in a 50 mM sulfuric acid solution, purged with Argon gas, and using an Au wire as counter electrode and a Hg/Hg₂Cl₂ electrode as reference, the potential was cycled from -0.13 V to 1.67 V vs RHE. The Cycle Voltammetry was carried out for around 12 cycles until the CV becomes stable.

At which point, the gold electrode was removed from the sulfuric acid solution, abundantly washed with Milli-Q water, gently dried with a wiper for the lab using (Kimwipes from Kimtech), and directly used for electrodeposition of Cu layer.

2.2.4 Monolayer deposition

In case of the Cu under potential deposition, a 50 mM H₂SO₄ + 5 mM CuSO₄ solution (pH 1.3) was prepared. 50 mL of the deposition solution were placed into a glass cell, closed with a cap, and argon gas was bubbling inside the cell. For the deposition, a three-electrode configuration was used: a gold wire was the counter electrode, a Hg/Hg₂Cl₂ electrode was used as reference, and the gold sheet was the working electrode (*Figure 2-3*). In order to remove all the oxygen dissolved in the solution, and saturated it with argon, the open circuit voltage was measured and monitored before each deposition, until a stable cell potential value was reached.

The deposition was carried out using a linear sweep voltammetry from 0.92 V to 0.40 V vs RHE (scan rate 10 mV s^{-1}), after 20 seconds of pretreatment at 0.92 V vs RHE. The aim of the pretreatment was to remove all the oxygenate group that may be present on the gold surface. When the Cu monolayer was deposited, the Au/Cu_{ML} was removed from the cell and placed into a beaker containing Milli-Q water to gently clean the surface from the deposition solution.

2.2.5 Cu bulk layer deposition

In case of the Cu bulk deposition, a 50 mM H₂SO₄ + 10 mM CuSO₄ solution (pH 1.3) was prepared. As described above for the monolayer deposition, a three-electrode configuration was used: a gold wire was the counter electrode, a Hg/Hg₂Cl₂ electrode was used as

reference, and the gold sheet was the working electrode. The solution was saturated with argon gas until a stable potential in an open circuit voltage measurement was achieved.

The deposition was carried out using a chronoamperometry experiment applying a potential of -0.18 V vs RHE (scan rate 10 mV s^{-1}) for 4 or 11 seconds for Au/Cu_{5nm} and Au/Cu_{10nm}, respectively. Before each deposition a pretreatment at 0.92 V vs RHE for 20 seconds was performed, in order to remove all the oxygenate group that may be present on the gold surface. The Au/Cu electrode thus obtained was gently cleaned removing it from the cell and placing it into a beaker containing Milli-Q water to eliminate the deposition solution from the surface.

2.2.6 Electrochemical reduction measurements

The electrochemical CO₂ reduction experiments were carried out using a typical three-electrode cell with a volume of 50 mL, completely sealed to avoid the gas leaking. An Ag/AgCl electrode saturated with KCl was chosen as the reference electrode, and a Pt wire as the counter electrode. The area of the cathode (working electrode) was typically of 1.0 cm², and was immersed in an aqueous electrolyte 0.1 M KHCO₃ solution CO₂ saturated by bubbling CO₂ gas (99.9999% purity) for 30 minutes (298K, pH 6.8). The flow-rate of the CO₂ gas that was purged inside the electrolyte solution was set to 10 ml min^{-1} by a mass-flow controller which was the beginning calibrated for CO₂ gas. During the electrochemical reduction, a magnetic stirrer bar kept stirred the electrolyte solution, in order to allow the mass transfer of the reagents toward the cathode.

Gas phase samples were taken from the sealed cell via online outlet connected to a Gas Chromatograph (GC) equipped with a TCD detector (for H₂ and CO quantification) and a FID detector (for hydrocarbons quantification). The GC collected a gas sample every 10 minutes, and it was split into two columns, one for each detector. The liquid products analysis was made using a High-Performance Liquid Chromatograph (HPLC). The liquid samples were collected manually at the end of the experiments and stored in an HPLC vial for the following analysis. The quantification of the products, by the information obtained from GC and HPLC analysis, is indispensable to evaluate the efficiency and selectivity of the electrocatalysts.

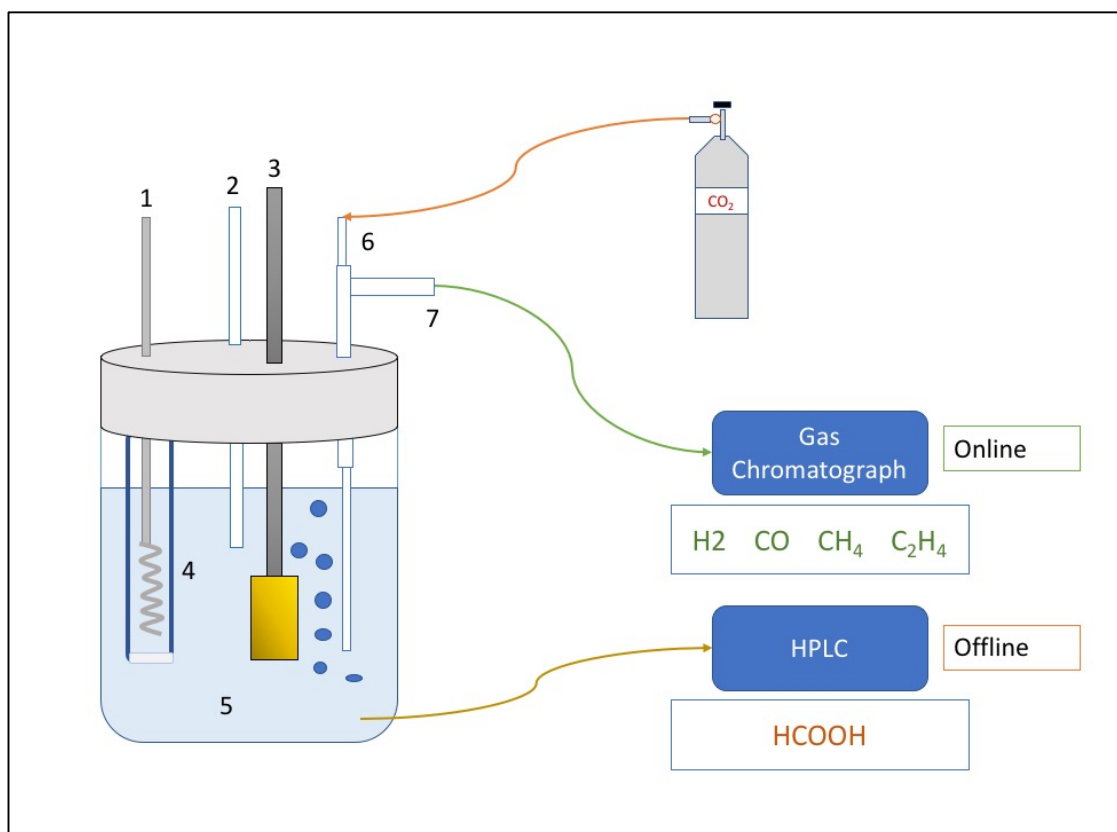


Figure 2-10. Scheme of the electrochemical cell used for the electrochemical measurements and the products analysis system. (1) Pt spiral counter electrode; (2) Ag/AgCl reference electrode; (3) working electrode; (4) glass chamber for the counter electrode; (5) 0.1 M KHCO₃, CO₂ saturated electrolytic solution; (6) inlet of CO₂ gas; (7) outlet of gas products.

The electrocatalytic activity was explored by using Chronoamperometric analysis. A constant potential was applied for 1 hour, after an induction period of 30 minutes needed to saturate the electrolyte solution with CO₂ gas and filling the dead space on the top of the cell. During the induction period the open circuit voltage was monitored to check the saturation of the solution, and also the GC analysis was started to check the presence of N₂ and O₂ peaks indicating a leak in the system.

All potentials for CO₂ reduction are reported with respect to the reversible hydrogen electrode (RHE) using the following equations:

$$E_{RHE} = E_{SCE} + 0.242 + 0.059 \text{ pH}$$

$$E_{RHE} = E_{Ag/AgCl} + 0.197 + 0.059 \text{ pH}$$

Several technical problems were encountered during the reduction reaction experiments on the course of this study. In the electrochemical system, a glass chamber (Figure 2-8 (4)) must be used because the anodic and cathodic reaction has to be separated. This precaution is necessary to prevent the reaction of the cathode products on the surface

of the Pt counter electrode, and also separate the oxygen evolution and do not send it to the GC. Frequently the chamber frit could be blocked from the gas into the electrolyte solution (e.g. CO₂, H₂ or CO), that implicates an error in the analysis. In addition to the gas, even some solid particles coming from the working electrode could block the frit, thus increasing the current resistance. Also, the formation of the products on the vertical surface of the electrocatalyst is a problem: in fact, bubble formation on the surface results in a decrease in the electrode area. To avoid this issue is necessary to control the rotation speed of the magnetic stirrer bar, to move the bubbles away from the electrode surface. One crucial point is the need to keep the electrochemical system completely air-tight because a leak can alter the gases products quantifications. Last but not least technical problem is due to the low conversion of CO₂ entered in the cell: the small amount of products represent a challenge for the detection and quantification, also because of the low products concentration in the CO₂ outflow.

2.3 Conclusions

In conclusion, the thickness effects of copper over layers on a gold substrate on the catalytic activity and selectivity of CO₂ electroreduction were investigated.

The modification of the gold surface by a copper monolayer could be a right way to change the selectivity of the gold as the catalyst for CO₂ reduction. A significant increase of current density in the presence of a Cu monolayer was observed at high overpotentials applied. The most interesting result shows that the presence of an atomic layer can considerably affect the reaction rate on the catalyst surface, respect a bare gold electrode. Contrariwise, a high thickness of the copper layer implicates a decrease of the reaction rate and high selectivity toward CO and HCOOH, though the hydrogen evolution reaction is less dominant in these conditions.

The copper monolayer modified electrode had shown less overall faradaic efficiency, that data suggest a different reactivity and selectivity in this surface; the surface strain can alter the chemisorption energies of reactive intermediates, favoring different pathways.

However, it is necessary to investigate more about the non-identified products and to understand why there has been no consistent production of low molecular weight hydrocarbons such as methane and ethylene.

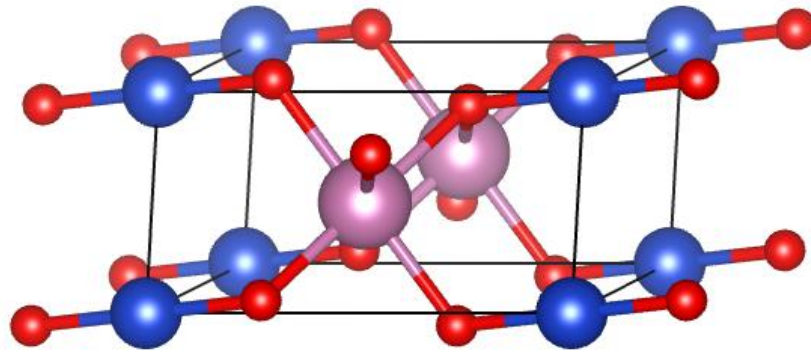
2.4 Bibliography

- [48] D. A. J. Rand e R. Woods, «A study of the dissolution of platinum, palladium, rhodium and gold electrodes in 1 M sulphuric acid by cyclic voltammetry.», *Journal of Electroanalytical Chemistry and Interfacial Electrochemistry*, vol. 35, n. 1, pp. 209-218, 1972.
- [49] E. Herrero, L. J. Buller e H. D. Abruña, «Underpotential deposition at single crystal surfaces of Au, Pt, Ag and other materials.», *Chemical Reviews*, vol. 101, n. 7, pp. 1897-1930, 2001.
- [50] Y. Hori, A. Murata, K. Kikuchi e S. Suzuki, «Electrochemical reduction of carbon dioxides to carbon monoxide at a gold electrode in aqueous potassium hydrogen carbonate.», *Journal of the Chemical Society*, vol. 10, pp. 728-729, 1987.
- [51] L. M. Fischer, M. Tenje, A. R. Heikanen, N. Masuda, J. Castillo, A. Bentien, J. Émneus, M. H. Jakobsen e A. Boisen, «Gold cleaning methods for electrochemical detection applications.», *Microelectronic Engineering*, vol. 86, pp. 1282-1285, 2009.

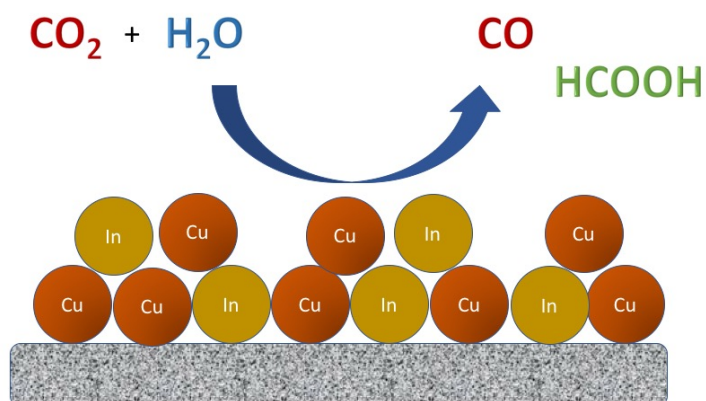
Chapter 3

3 CO₂ Electroreduction on Cu-In Alloy

The work started with the synthesis optimization of CuInO₂, a bimetallic mixed oxide used as precursor for a Cu-In alloy catalyst. The precursor was further thermally reduced at various temperature, in order to obtain a bimetallic catalyst with different catalytic surfaces.



Subsequently, the working electrodes obtained using a carbon paper as substrate, were used as electrocatalysts for the reduction of CO₂ in an aqueous solution.



3.1 Results and discussions

3.1.1 Synthesis of CuInO₂ precursor and its direct use for CO₂ reduction

The CuInO₂ is a bimetallic mixed oxide in the family of Cu-based delafossites, such as CuAlO₂, CuGaO₂, CuScO₂ and CuFeO₂. The crystal structure of the delafossite group A³⁺B⁺O₂ consists of a sheet of linearly coordinated A cations stacked between edge-shared octahedral layers (BO₆). Two layers can be individuated: a triangular-patterned A cations layers and a layer consisting in an edge-sharing BO₆ octahedral compacted. There are two polytypes for the delafossite structure, in case of CuInO₂ the layers are stacked each layer in the same direction making a rhombohedral 3R type with a R3m space group.

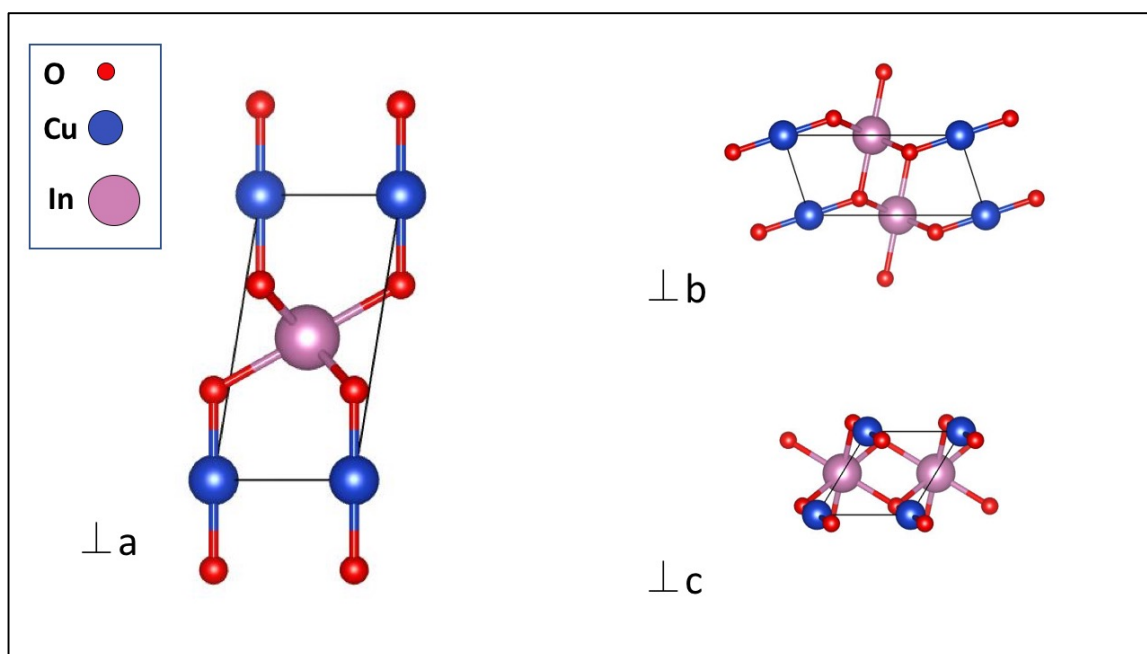
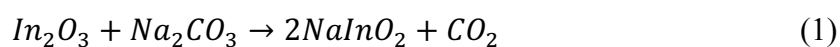


Figure 3-1. Delafossite crystal structure of CuInO₂. Crystal lattice data obtained from the website: <http://www.catalysthub.net/> and elaborated using the open source software VESTA 3.4.0 (Visualization for Electronic and Structural Analysis).

The synthesis of CuInO₂ was carried out in two steps by ion-exchange reactions at high temperature, starting from In₂O₃ and CuCl as precursors. The synthesis procedure was built from literature [52] and subsequently optimized. The first reaction occurred between In₂O₃ and Na₂CO₃ at 1273 K under nitrogen flow to obtain NaInO₂, with the object to isolate the [InO₂]⁺ ion and bond it with a mobile counterion such as Na.



A significant advantage of this reaction is the production of CO₂ as reaction co-product, which being gaseous leaves the alumina boat, thus avoiding the purification of the product.

The second step was the insertion of Cu^{I} into the crystal lattice by ion exchange with Na. CuCl was chosen as source of Cu^{I} because the chlorine can bond with Na to make a stable co-product as NaCl , favoring the reaction. Moreover, the NaCl formed can be easily washed with water, allowing a simple purification of the final product.



The procedure reported in the literature suggests to use a temperature of $400\text{ }^\circ\text{C}$ for the reaction (2), but the product obtained is not pure and present both NaInO_2 and In_2O_3 reagents suggesting a low conversion of both reaction. In our case we try to reproduce the same experiments but, even if the conversion of In_2O_3 may be complete, the NaInO_2 pattern was still present in the XRD diffractogram (*Figure 3-2*).

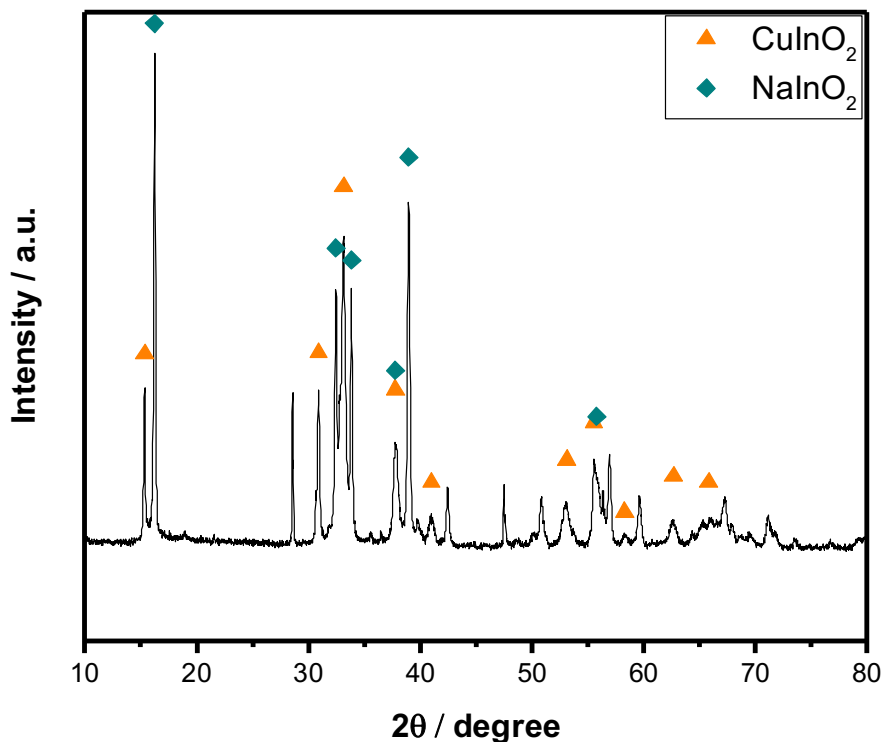


Figure 3-2. XRD diffractogram of CuInO_2 as prepared heating at 400°C .

In order to increase the conversion and obtain a product with greater purity, the reaction (2) was conducted in the tube furnace, using the same inert atmosphere, but increasing the temperature from 400 to 500°C .

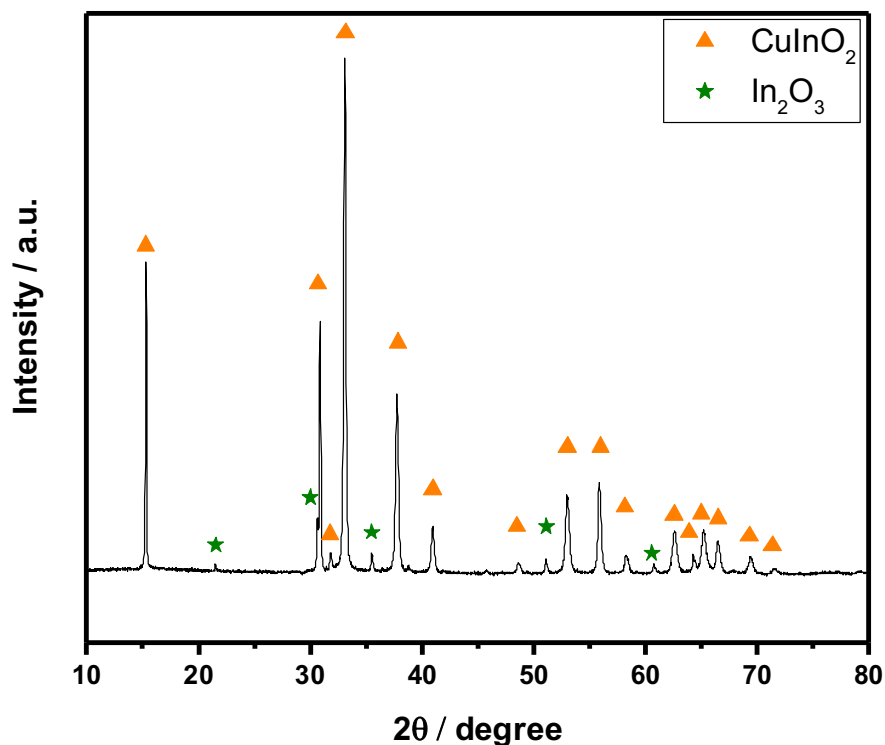


Figure 3-3. XRD diffractogram of CuInO_2 as prepared heating at 500°C.

Observing the XRD diffractogram in *Figure 3-3*, the major pattern is ascribable to CuInO_2 that shows peaks sharper than the 400 °C sample, along only a small amount of In_2O_3 precursor as impurity phase. Consequently, this second approach was chosen to prepare the precursor of the copper-indium-based catalysts.

The catalyst precursor CuInO_2 was directly tested for CO_2 reduction, with the aim of reduce it to Cu-In alloy in situ during the experiment applying a negative potential. The CuInO_2 powder was deposited on a carbon paper substrate using the electrophoretic deposition technique. As shown in *Figure 3-4*, two sheets of 1 x 2 cm dimension were placed vertically facing each other (3 mm of distance) in a suspension containing the precursor powder in acetone and I_2 .

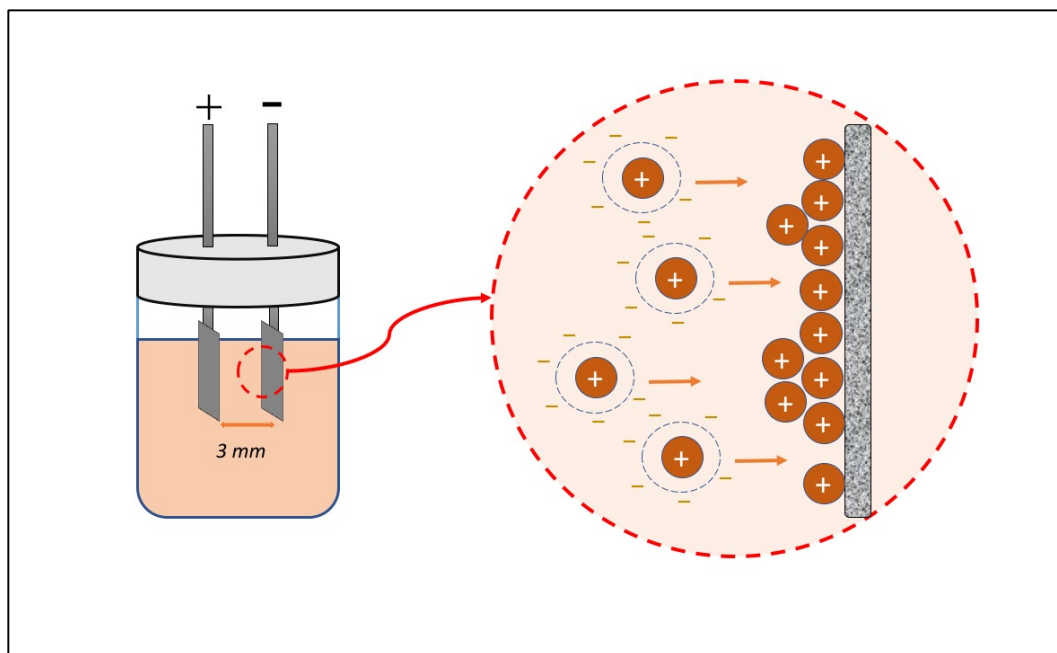
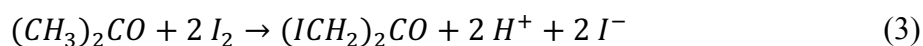


Figure 3-4. Schematic representation of Electrophoretic deposition of CuInO_2 on carbon paper substrate.

During the electrophoretic deposition, the CuInO_2 particles are covered with proton generated from the reaction between the solvent acetone and I_2 :



The adsorption of the formed proton on the surface of the CuInO_2 particles make them positively charged, then with a voltage application the particles move toward the cathode negatively charged and deposit there. The use of organic solvent for the electrophoretic deposition is necessary to avoid the gas evolution at high voltage associated at aqueous media; anyhow, the use of organics required higher voltage and high disposal costs [53].

After deposition, the dried CuInO_2 electrode was tested for the electrochemical reduction of CO_2 . The electrocatalytic performance was analyzed by chronopotentiometry, using a constant current density of -1.67 mA cm^{-2} for 2 hours.

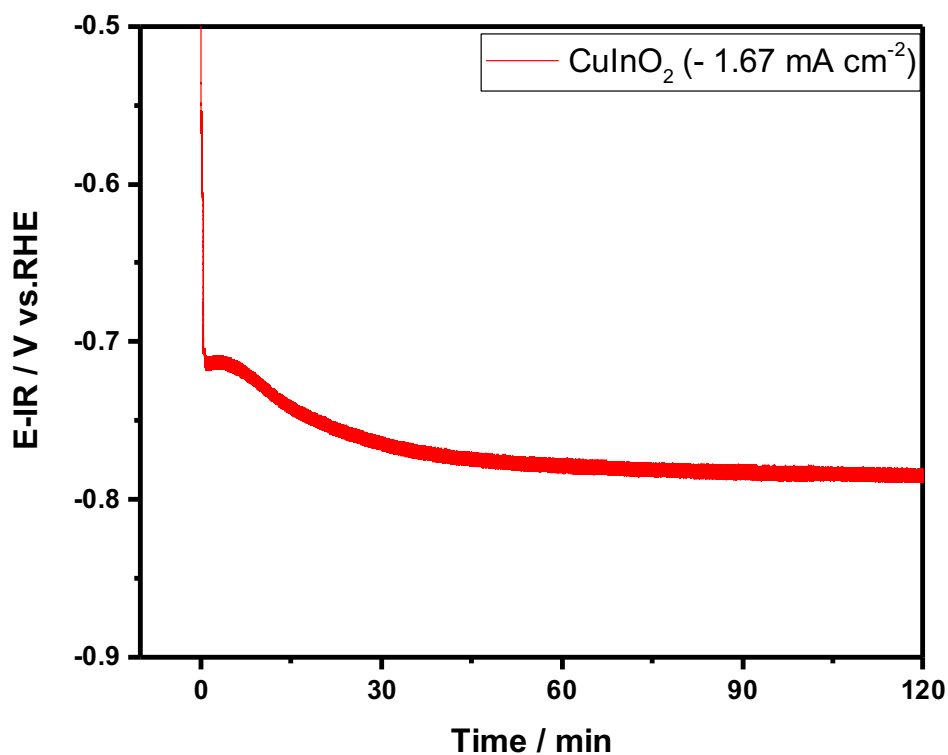


Figure 3-5. Chronopotentiometric electrolysis profile at current density of -1.67 mA cm^{-2} (0.1 M KHCO_3 , pH 6.8, CO_2 saturated).

In *Figure 3-5* is reported the chronopotentiogram obtained, to maintain the current stable the potentiostat needed to apply to the system a less negative potential for the first 50 minutes, this observation suggests the presence of an initial reduction step of the electrode surface. However, the only product detected by GC was the H_2 produced from the water splitting reaction, and not any liquid products were detected by HPLC analysis.

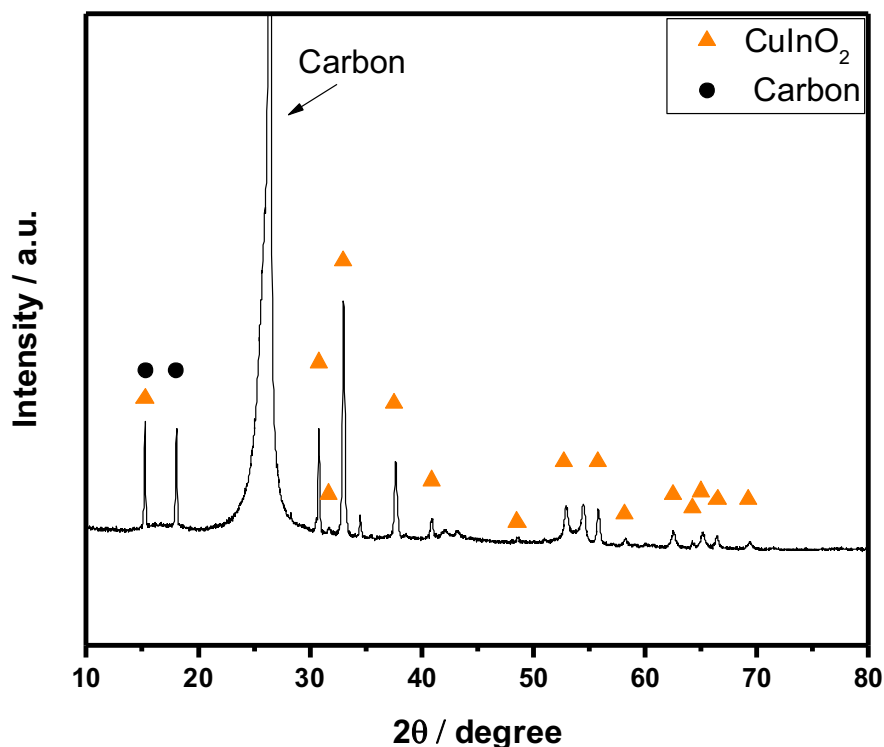


Figure 3-6. XRD diffractogram of the electrode surface after CO₂ reduction experiment.

The XRD diffractogram in *Figure 3-6* shows that the sample after electrolysis was not completely reduced. The patterns of CuInO₂ are still visible and there are not any pattern of Cu-In alloy or Cu and In as metals. These evidence is in according with the absence of CO₂ reduction products during the experiments. The hypothesis was that the current was passed directly through the carbon paper because a weak contact between the CuInO₂ and the carbon-based support.

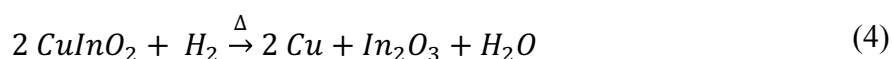
3.1.2 Thermal reducing treatment and samples characterization

Considering the negative results obtained with the CuInO₂ electrochemical reduction, the possibility of performing a forced reduction using a hydrogen stream as a reducing agent was explored. The goal was to reduce CuInO₂ and improve physical contact between the catalyst and the carbon paper substrate.

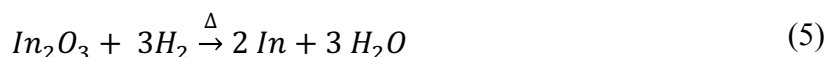
To better understand the optimal reduction conditions for the material, thermogravimetric analysis (TGA) and a temperature-programmed reduction (TPR) were realized.

The TGA was obtained using an automatic thermogravimetric analyzer, and the samples were placed inside an alumina crucible of 1.6 mL of volume. In addition to the CuInO₂ sample, a Cu₂O and In₂O₃ sample were also analyzed for comparison. The operating conditions set in the instrument were a reducing atmosphere created by flowing a H₂ 4% in Argon stream (100 mL min⁻¹), a ramping rate of 10 °C min⁻¹ in a temperature range from 25 to 900 °C.

In *Figure 3-7* are reported thermogram of the three samples examined. The CuInO₂ thermogram shows a weight loss of about 5% until 400 °C. An Oxygen atom represent the 7% of the total CuInO₂ weight, for this reason, is reasonable thinking that the first weight loss in the thermogram is probably due to the following reaction:



the second (between 400 and 600 °C) and the third weight loss (between 600 and 800 °C) are ascribable to the reduction of In₂O₃ to In metal according to the following reaction:



Reference samples analysis confirms the two hypotheses made above, in fact, the Cu₂O sample shows steep weight loss around 400 °C (coinciding with the first step observed in the CuInO₂ sample); also, the In₂O₃ sample shows a loss of weight that begins slowly around 550 °C and becomes faster than 700 °C. However, it is not possible to perfectly allocate the second weight loss, this is probably due to a mixed reduction process of the two metals. This possibility appears more apparent by observing the results obtained through TPR analysis.

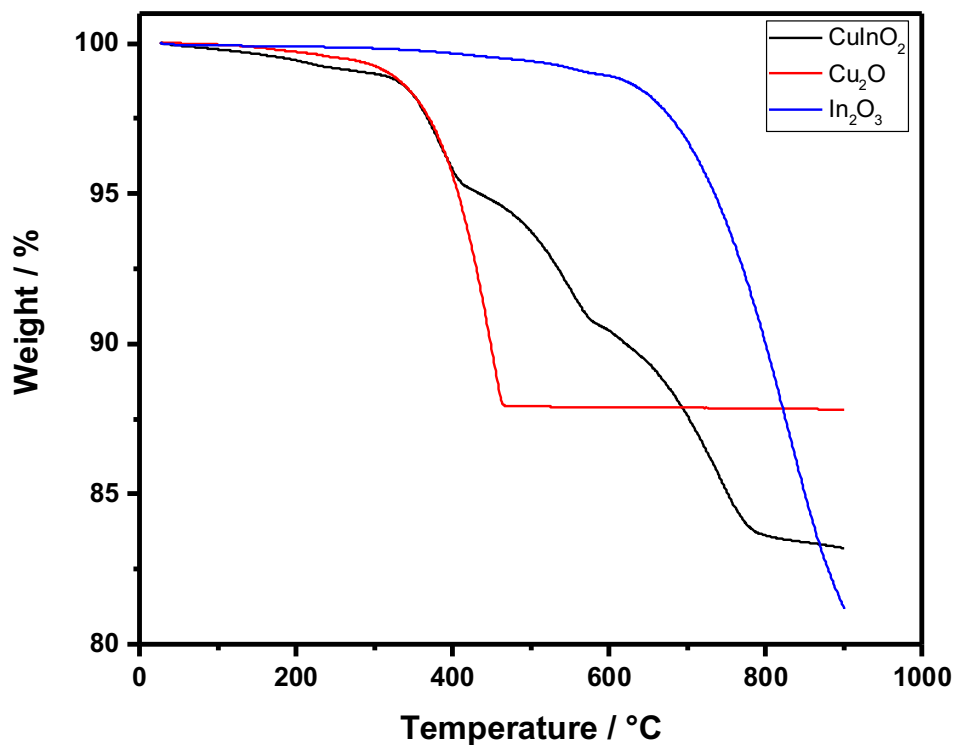


Figure 3-7. TGA of CuInO_2 , Cu_2O and In_2O_3 obtained by flowing a H_2 4% in Argon stream, with a ramping rate of $10\text{ }^\circ\text{C min}^{-1}$ in a temperature range from 25 to 900 $^\circ\text{C}$.

For the TPR analysis, the sample was placed into a U-tube and blocked with rock wool. The U-tube containing the sample was positioned inside a furnace where is possible to control the temperature using a thermocouple near the sample, in a range from 25 to 900 $^\circ\text{C}$. An H_2 4% in Argon stream (100 mL min^{-1}) flowed through the sample, and the gaseous mixture was detected by a TCD detector in a temperature range from 25 to 900 $^\circ\text{C}$. Also in this case, besides the CuInO_2 sample, Cu_2O and In_2O_3 samples were analyzed for comparison.

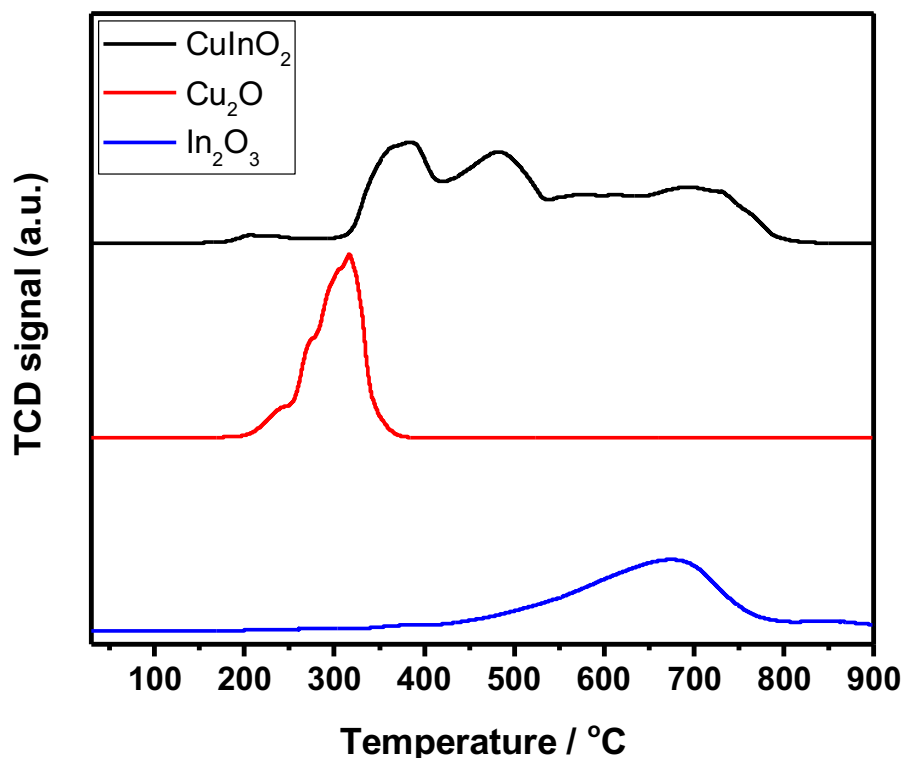


Figure 3-8. TPR analysis of CuInO_2 , Cu_2O and In_2O_3 obtained by flowing a H_2 4% in Argon stream, with a ramping rate of $10\text{ }^\circ\text{C min}^{-1}$ in a temperature range from 25 to 900 $^\circ\text{C}$.

In *Figure 3-8*, the CuInO_2 chromatogram shows a broad big peak from 350 to 800 $^\circ\text{C}$, which is the result of an overlap of more peaks. As we have seen before with the TGA, even in this case it is possible to distinguish three sections. The first peak is clearly related to copper reduction, as seen from the Cu_2O reference sample thermogram. The copper reduction peak of the CuInO_2 thermogram is slightly shifted to higher temperatures, because the greater stability is exercised by the different crystalline structure, so the copper reduction reaction requires a slightly higher temperature. The In_2O_3 sample chromatogram also shows a large peak that begins at 400 $^\circ\text{C}$, that is the same temperature of the second weight loss observed in the CuInO_2 thermogram.

In conclusion, it was decided to prepare three different samples, using as reduction temperature corresponding the three CuInO_2 partial reduction visible in the thermogram in *Figure 3-7*: 450, 600 and 800 $^\circ\text{C}$.

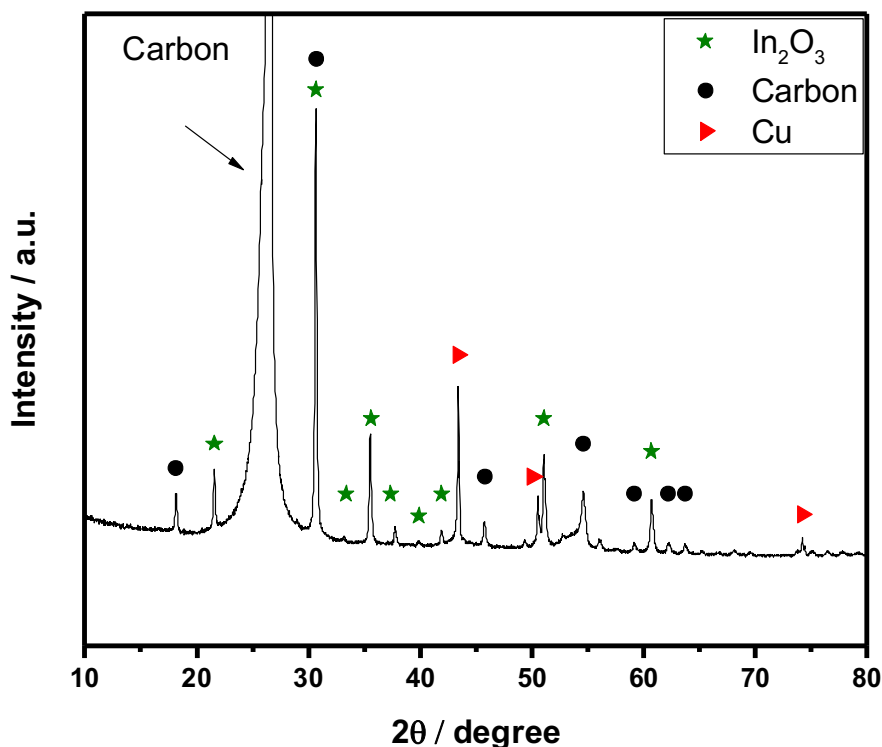


Figure 3-9. XRD profile of the CuInO_2 on carbon paper sample thermal reduced at $450\text{ }^\circ\text{C}$ under H_2 4% flow in argon (300 mL min^{-1}).

In *Figure 3-9* is reported the XRD diffractogram of the sample thermally treated at $450\text{ }^\circ\text{C}$. After three hours of reduction at that temperature, the sample was partially reduced, in fact, the CuInO_2 pattern is completely disappeared in the diffractogram. The major patterns were relative to the presence of Cu metal and In_2O_3 . These results confirm the previously hypothesis, at that temperature of $450\text{ }^\circ\text{C}$ only the copper can be reduced leaving a water molecule, while the indium preserves its oxidation state as In^{3+} .

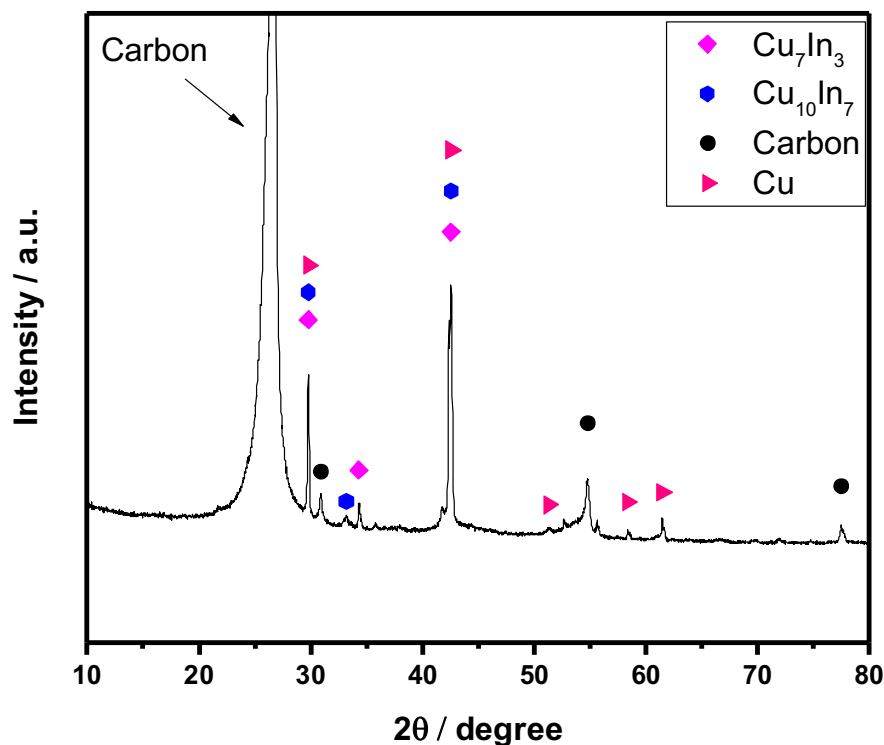


Figure 3-10. XRD profile of the CuInO_2 on carbon paper sample thermal reduced at $600\text{ }^\circ\text{C}$ under H_2 4% flow in argon (300 mL min^{-1}).

In *Figure 3-10* is reported the XRD diffractogram of the sample thermally treated at $600\text{ }^\circ\text{C}$. This shows that at that temperature the CuInO_2 can be completely reduce, forming two different phases of Cu-In alloy and Cu metal. The two phases of Cu-In observed were the δ -phase Cu_7In_3 and the η -phase $\text{Cu}_{10}\text{In}_7$: the first is a well-noted tetragonal alloy structure where the In atoms and some Cu atoms form parallel payers and between them there is a only Cu atom layer [54]; while the $\text{Cu}_{10}\text{In}_7$ is a relatively new discovered η -phase alloy, with a crystal structure similar to $\text{Cu}_{11}\text{In}_9$, but more ordered and consequently less stable [55].

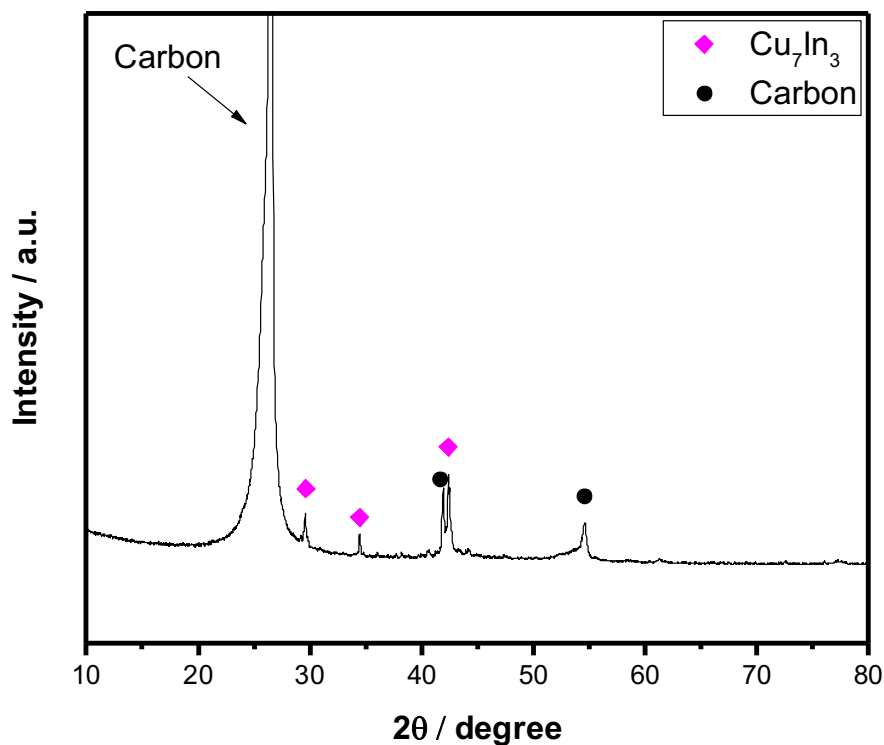


Figure 3-11. XRD profile of the CuInO_2 on carbon paper sample thermal reduced at $800\text{ }^\circ\text{C}$ under H_2 4% flow in argon (300 mL min^{-1}).

In *Figure 3-11* is reported the XRD diffractogram of the sample thermally treated at $600\text{ }^\circ\text{C}$. At such a high temperature, the sample is completely reduced and the only crystalline form that can be detected by XRD analysis is attributable to the Cu_7In_3 alloy. This last analysis confirms what was observed through TGA and TPR analysis. The minimum temperature for a sample reduction is $600\text{ }^\circ\text{C}$, reaching a temperature of $800\text{ }^\circ\text{C}$ is achieved with a stable Cu-In alloy.

For a better understanding of the samples and their morphology, SEM microscopy was performed. Samples were covered with palladium and analyzed using a microscope Magellan 400 XHR from FEI. In *Figure 3-12*, the SEM images of the CuInO_2 sample show large particle aggregates describable as a macroporous structure.

Instead, in *Figure 3-13*, the SEM images of the sample thermally reduced at $450\text{ }^\circ\text{C}$ are shown. It is interesting to note that in a morphological structure almost unchanged with respect to the previous sample, well-defined crystal structures appear, attributable to the metal Cu identified by XRD analysis in *Figure 3-9*.

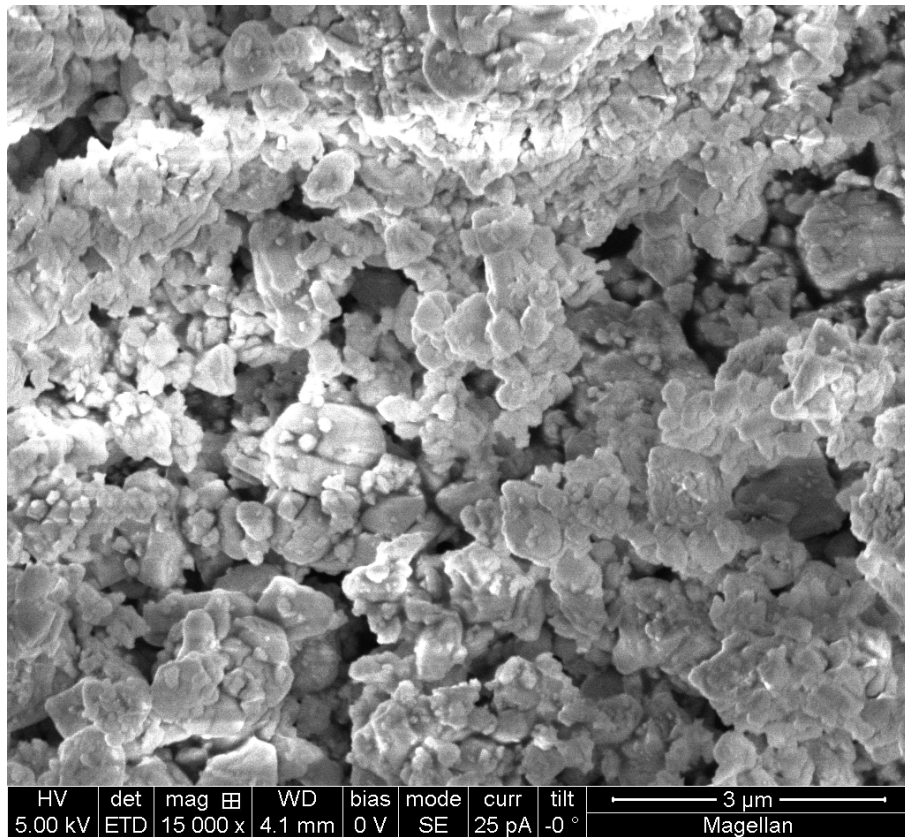
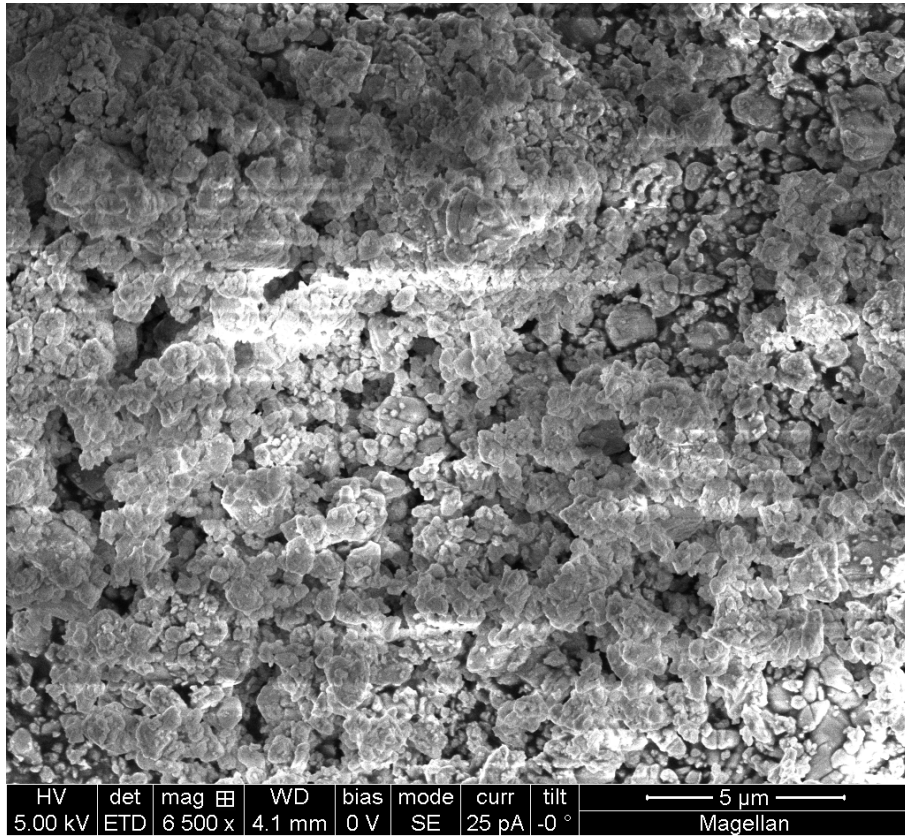


Figure 3-12. SEM images of the CuInO_2 powder.

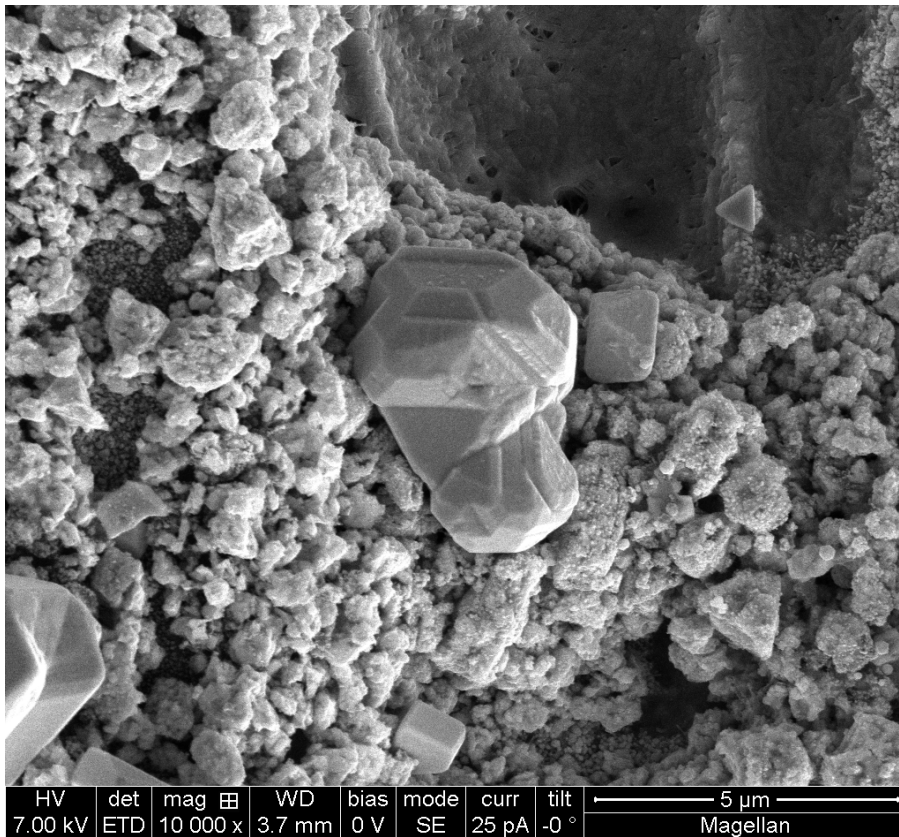
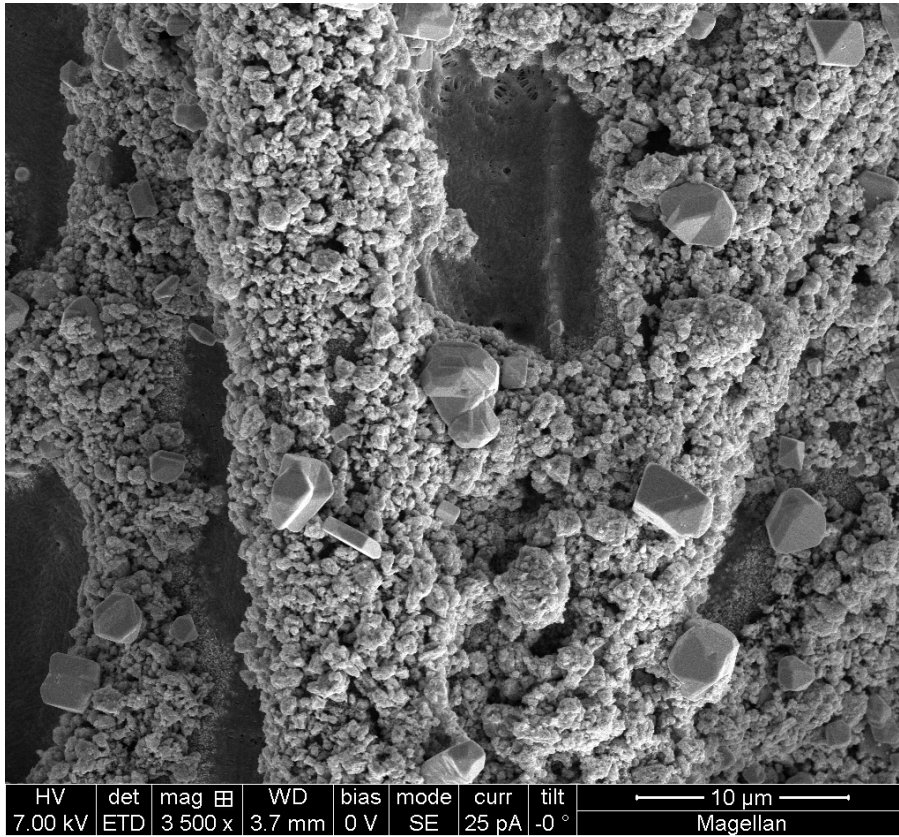


Figure 3-13. SEM images of the thermal reduced sample at 450 °C.

In *Figure 3-14* and *Figure 3-15*, are shown the SEM images of the thermally reduced samples at 600 and 800 °C, respectively. It is possible to notice the appearance of spherical crystalline structures, more abundant in the case of the reduced sample at 800 ° C. Considering the previous XRD analysis; it is possible to assume that such spherical formations are attributable to the Cu_7In_3 alloy.

This alloy is present in the sample reduced to 600 ° C, but in smaller quantities, in fact, the SEM images show a more varied morphological structure with the presence of small parallelepiped shaped crystalline formulations that could be brought back to the $\text{Cu}_{10}\text{In}_7$ alloy or a Cu metal.

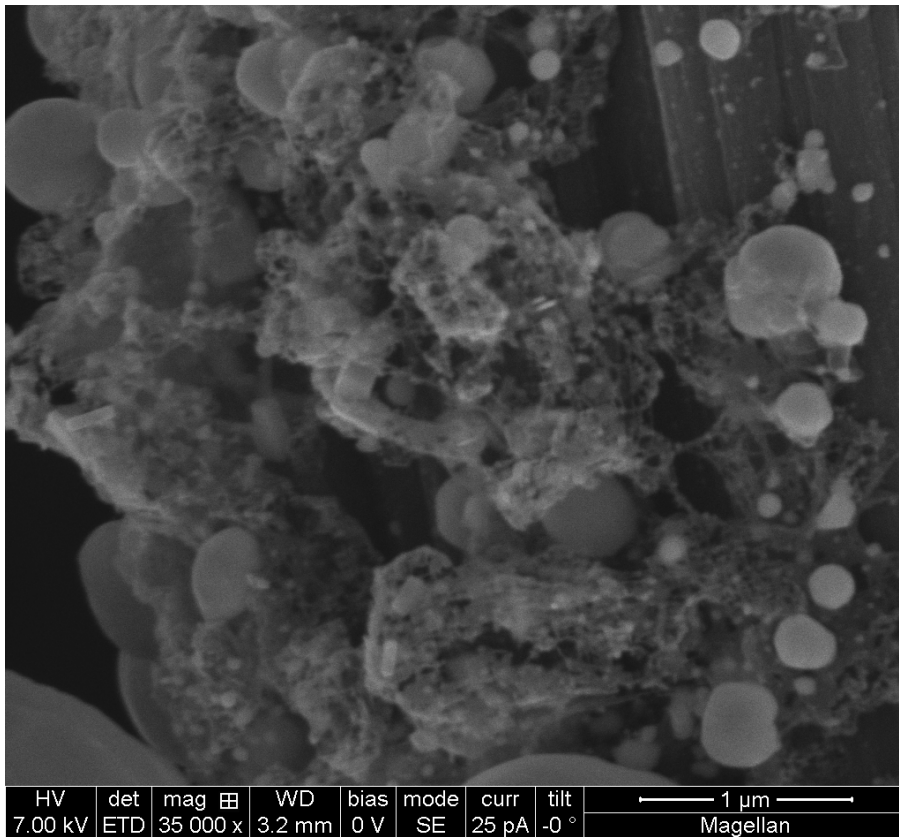
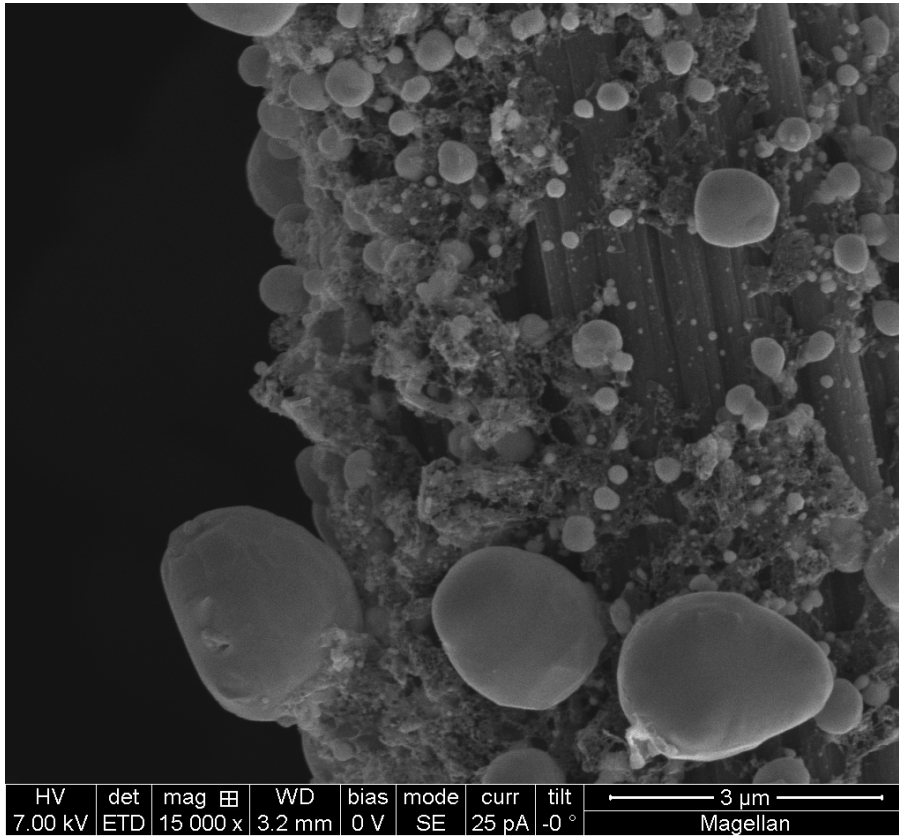


Figure 3-14. SEM images of the thermal reduced sample at 600 °C.

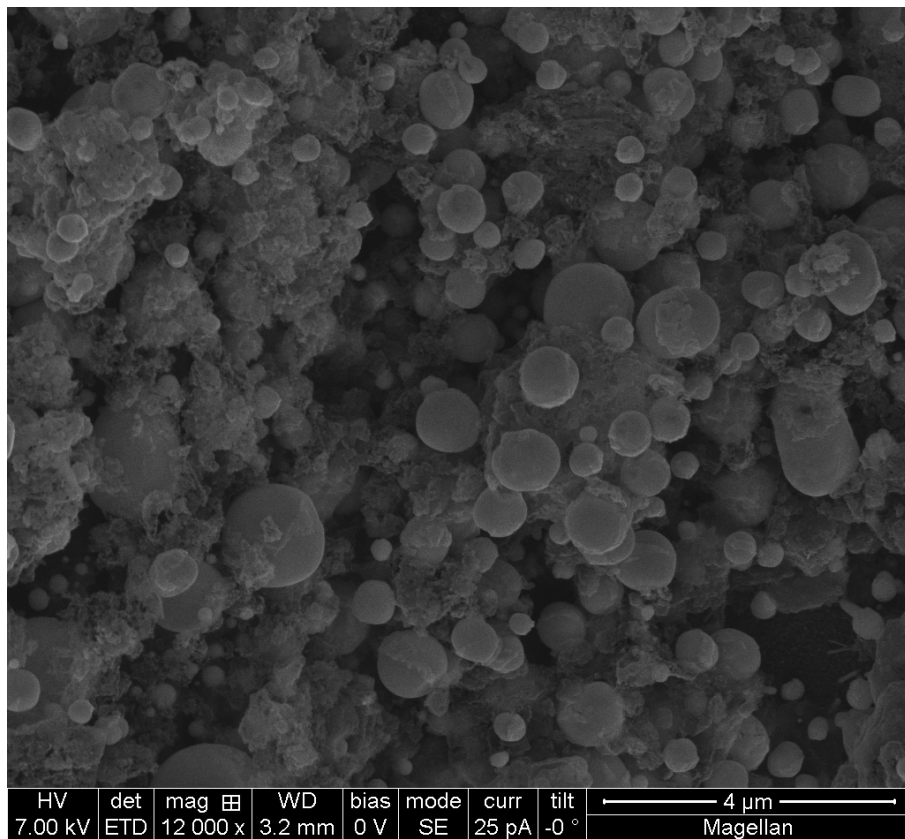
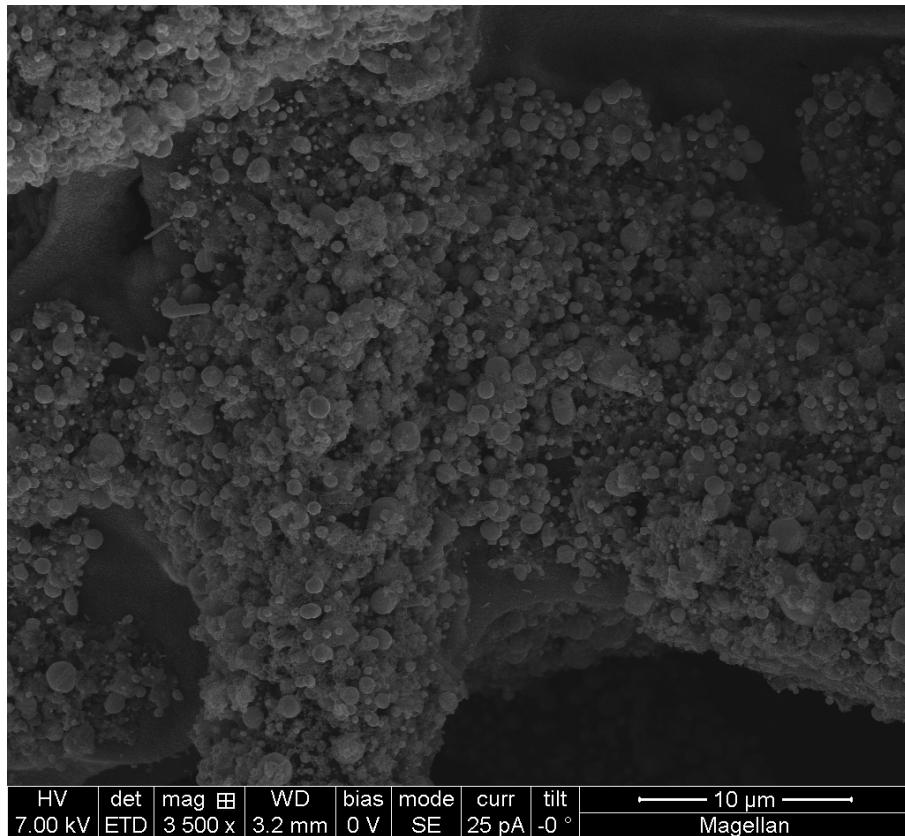


Figure 3-15. SEM images of the thermal reduced sample at 800 °C.

3.1.3 Electrochemical CO₂ reduction measurements

The electrocatalytic performance of the thermally reduced samples were evaluated at geometric-electrode current density of -1.67 mA cm^{-2} for 1 hour in 0.1 M KHCO_3 electrolyte solution, saturated with CO_2 . To compare the performance of the samples, another sample, thermally treated at the same condition but at a lower temperature ($200 \text{ }^\circ\text{C}$) than the minimum reduction temperature observed during the characterization.

The chronopotentiograms showed in *Figure 3-16*, report the potentials applied versus a constant current density of -1.67 mA cm^{-2} for 1 hour. The 200 and $450 \text{ }^\circ\text{C}$ samples showed, up to ≈ 50 minutes, an initial transition of the potential to originate from the material reduction, while the 600 and $850 \text{ }^\circ\text{C}$ samples showed a constant potential applied from the beginning of the experiment. Moreover, a more negative potential was needed to maintain the same current density in case of the two-last sample. In particular, the $600 \text{ }^\circ\text{C}$ sample showed a potential of -0.8 V vs RHE , while the $450 \text{ }^\circ\text{C}$ sample showed a potential of -0.6 V vs RHE at steady-state condition.

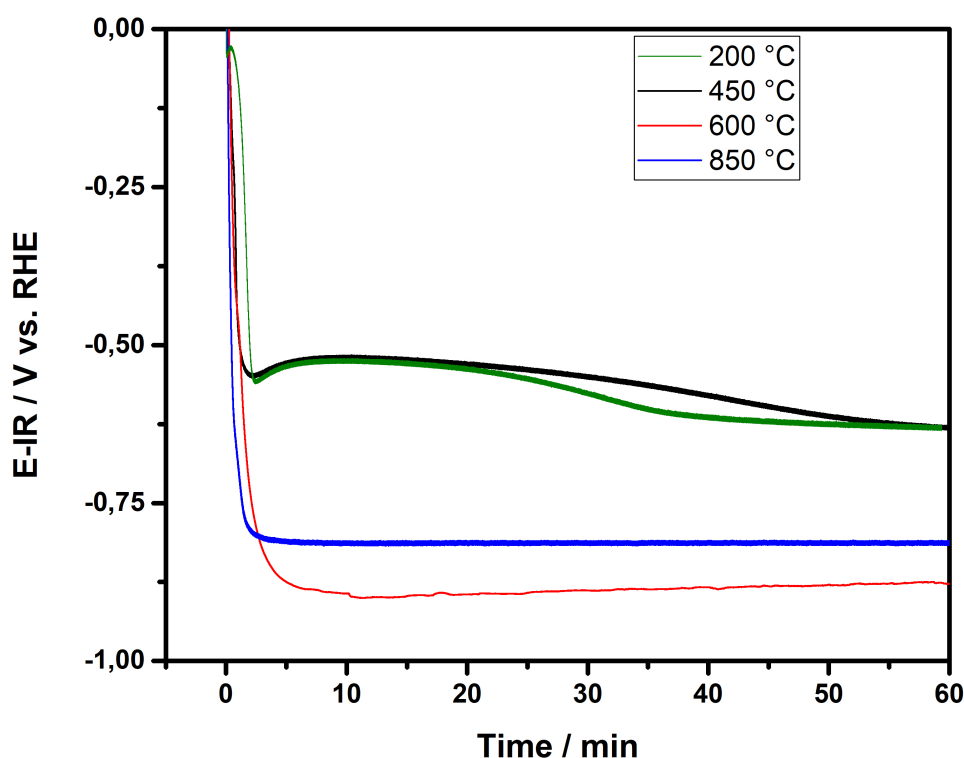


Figure 3-16. Chronopotentiometric electrolysis of thermally reduced samples at a current density of -1.67 mA cm^{-2} in CO_2 saturated 0.1 M KHCO_3 .

In *Figure 3-17* the faradaic efficiency of each sample is reported. The sample thermally treated at $200 \text{ }^\circ\text{C}$ generated a high faradaic efficiency toward H_2 evolution (63%) and very

low value for the overall CO₂ reduction reaction, to form CO and HCOOH with a faradaic efficiency of 5 and 8%, respectively. How was previously observed with the sample of CuInO₂ not treated, even in this case the probably weak contact between the catalyst precursor and the carbon paper support avoid the its electrochemical reduction, and the hydrogen evolution reaction accurses directly on the carbon paper surface.

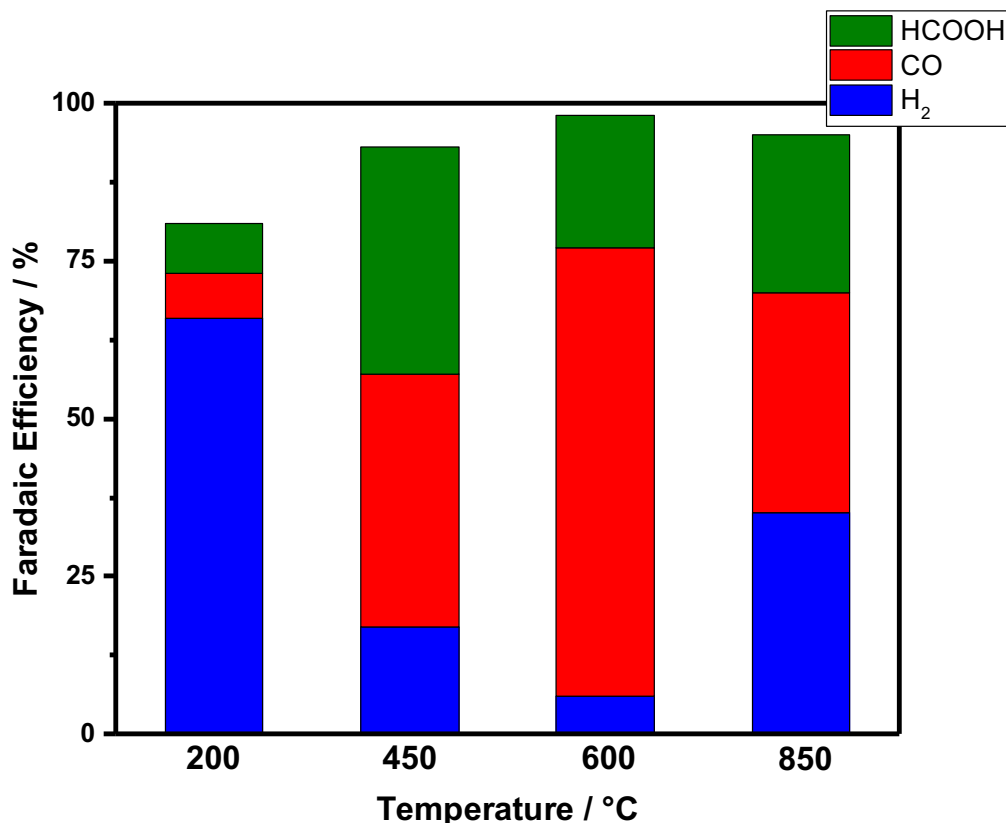


Figure 3-17. Comparison of the Faradaic Efficiencies obtained during the CO₂ reduction experiments at constant current density.

In case of 450 °C sample, the hydrogen evolution reaction was not dominant and CO₂ reduction was the main reaction occurring on the electrode surface. The H₂ faradaic efficiency was about 13%, while the faradaic efficiency toward CO and HCOOH was 43 and 40%, respectively. The formation results of both main product are interesting if compared with the chronopotentiogram in *Figure 3-16*: during the electrochemical experiment was visible an initial reduction step due to the presence on the electrode of In₂O₃. In this way, on the surface of the electrode there are Cu and In as metals, as two separate phases. In *Figure 3-18* and *Figure 3-19*, the XRD analysis of the 450 °C sample before the electrochemical experiment and after it are reported. It is evident from the

diffractogram the presence of both metals as separate phase, and there was not any Cu-In alloy.

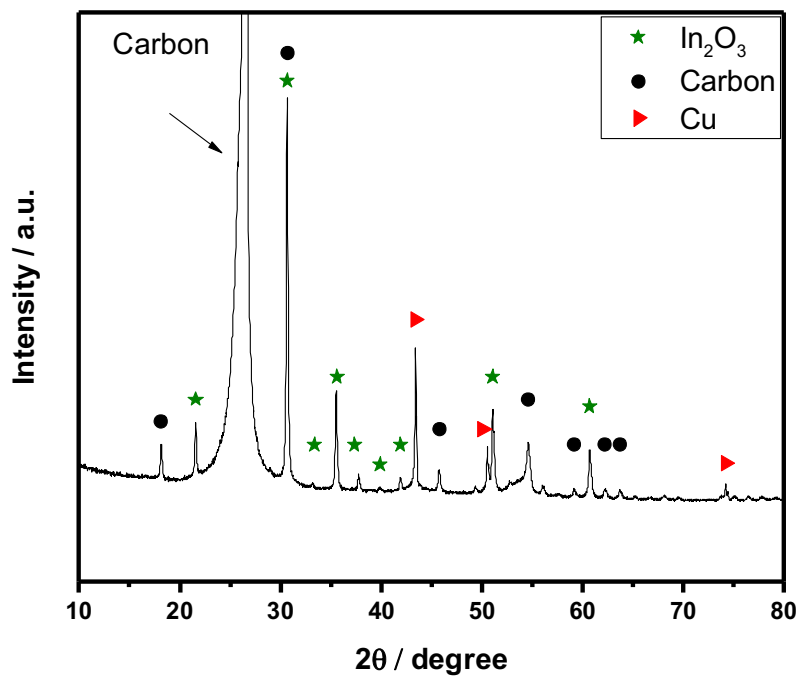


Figure 3-18. XRD analysis of the 450 °C sample before CO₂ reduction experiment.

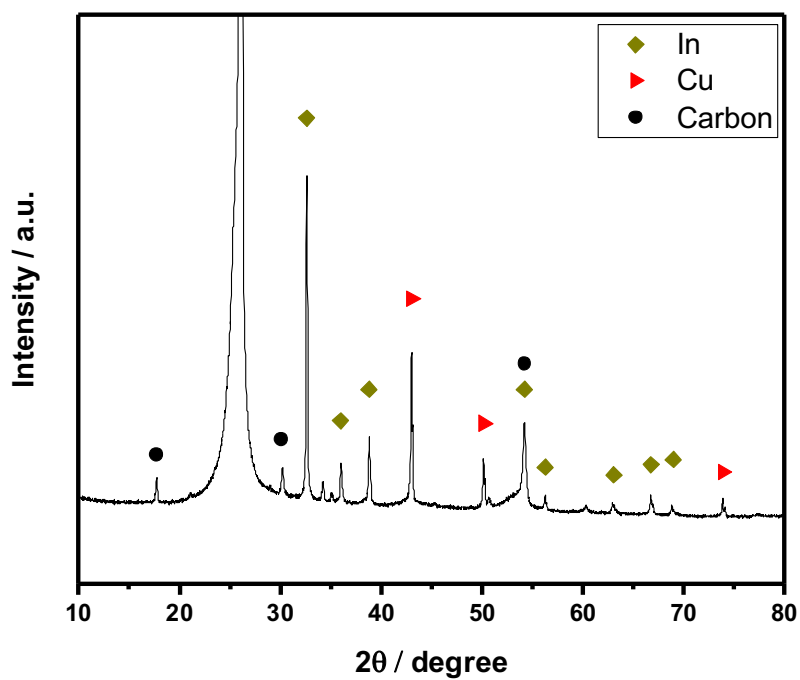


Figure 3-19. XRD analysis of the 450 °C sample after CO₂ reduction experiment.

The best result was obtained in case of the 600 °C sample: overall CO₂ reduction faradaic efficiency was of 93%, with a specific faradaic efficiency of 70% toward CO and 23% toward HCOOH. The presence of Cu-In alloys on the surface had an influence for the selectivity of the reaction, suppressing the hydrogen evolution reaction and favoring the CO formation.

The 800 °C sample showed a less overall faradaic efficiency toward CO₂ reduction. A H₂ faradaic efficiency of 36% was observed, and 34% of faradaic efficiency toward CO was recorded. The presence of only Cu₇In₃ phase in this sample suggests that this Cu-In alloy is not a good catalyst for CO₂ reduction, while the Cu₁₀In₇ present on the surface of 600 °C sample could better influence the selectivity of the reaction toward CO production.

The thermally reduced samples were further tested at various applied potentials by chronoamperometry technique. From *Figure 3-20* to *Figure 3-23* are shown the current density and the faradaic efficiency at different potentials from -0.4 to -0.8 V vs RHE in 0.1 M KHCO₃ solution, CO₂ saturated.

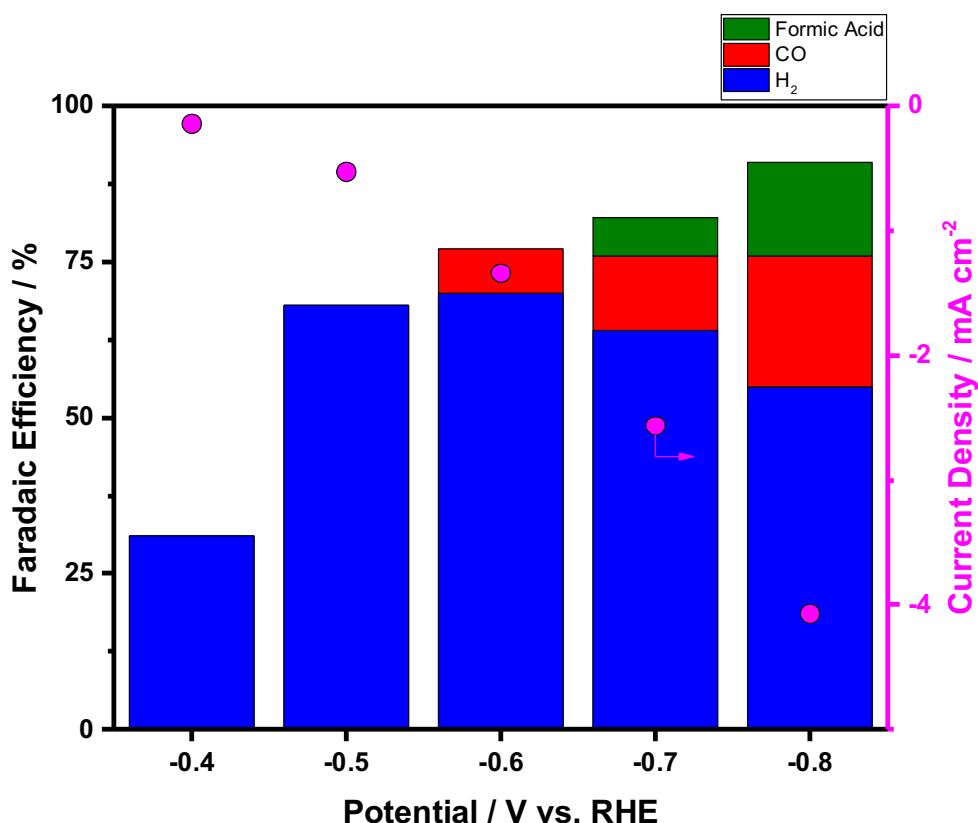


Figure 3-20. Current density and Faradaic efficiencies of the 200 °C thermally reduced sample at various applied potentials from -0.4 to -0.8 V vs RHE in CO₂ saturated 0.1 M KHCO₃ solution.

The 200 °C thermally treated electrode started to convert CO₂ to CO at -0.6 V vs RHE, while the HCOOH formation started from -0.7 V vs RHE. The current density increases at lower potentials; however, these high values are imputable to the hydrogen evolution reaction.

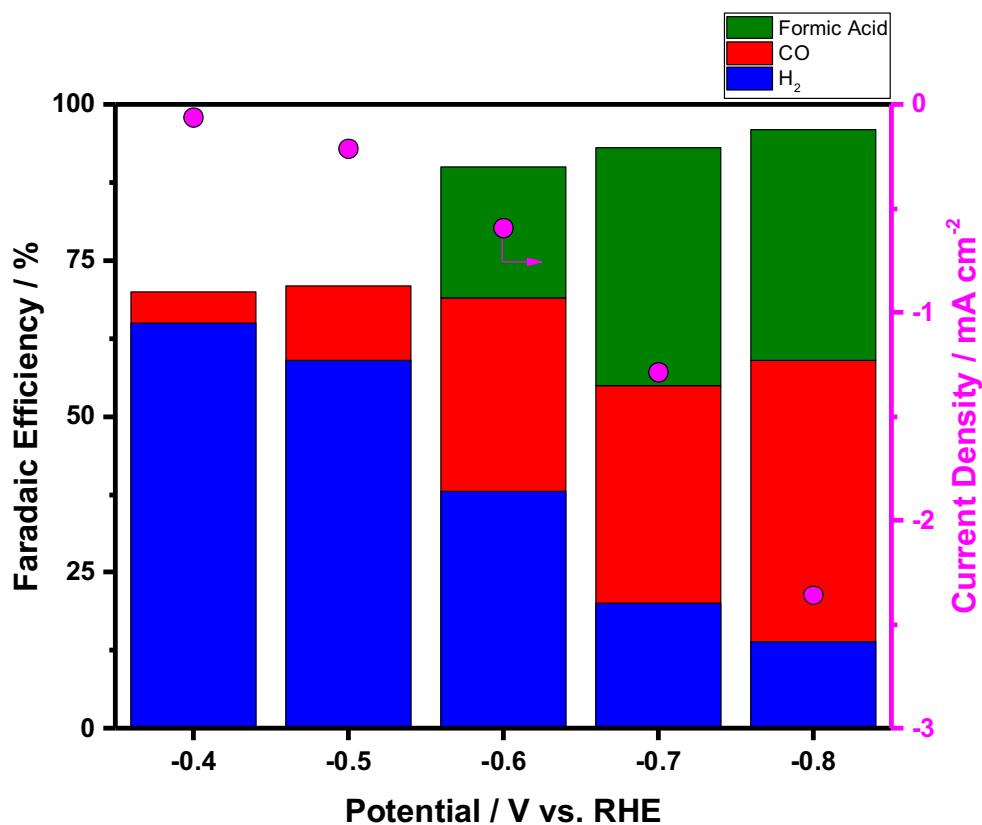


Figure 3-21. Current density and Faradaic efficiencies of the 450 °C thermally reduced sample at various applied potentials from -0.4 to -0.8 V vs RHE in CO₂ saturated 0.1 M KHCO₃ solution.

The 450 °C thermally treated electrode started to convert CO₂ to CO at -0.4 V vs RHE, while the HCOOH formation started from -0.6 V vs RHE. The current density observed was lower than the 200 °C sample, but in this case at high overpotentials almost all the current passing through the electrode comes from CO₂ reduction. How discussed before, the electrode shows a separate selectivity for CO and HCOOH, due to the catalyst morphology.

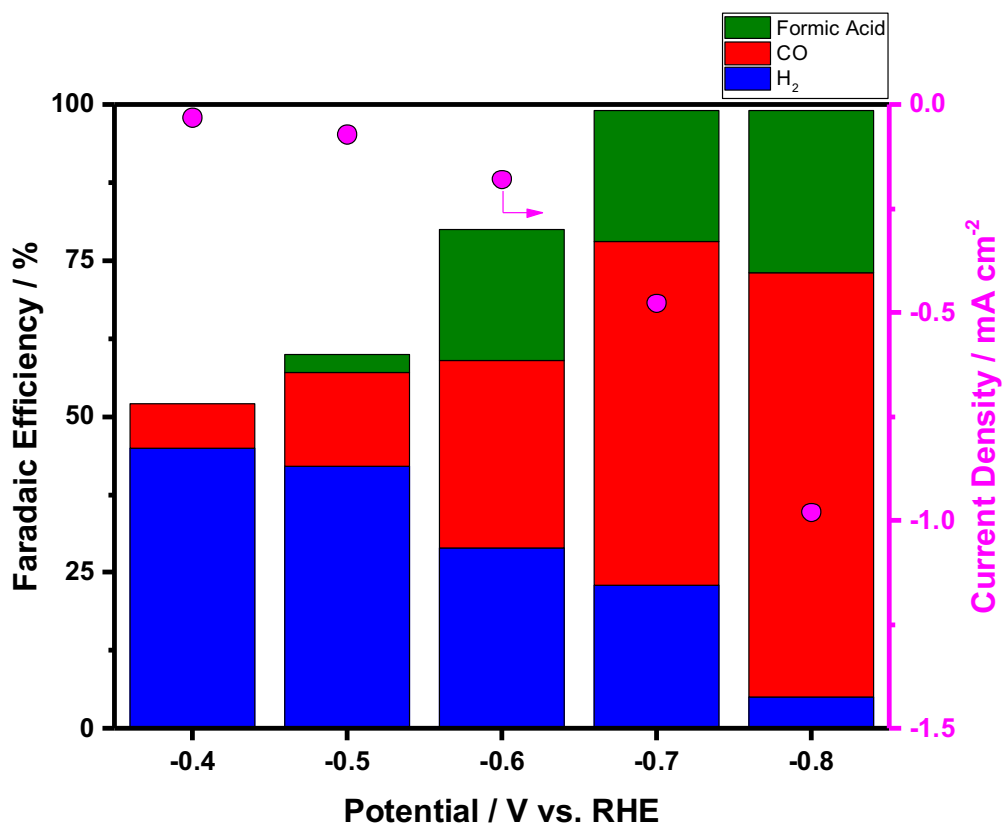


Figure 3-22. Current density and Faradaic efficiencies of the 600 °C thermally reduced sample at various applied potentials from -0.4 to -0.8 V vs RHE in CO_2 saturated 0.1 M KHCO_3 solution.

The 600 °C thermally treated electrode started to form CO at -0.4 V vs RHE, while the HCOOH formation started from -0.5 V vs RHE. The CO faradaic efficiency gradually increase with the overpotential, achieving a considerable value of 71% at -0.8 V vs RHE. Also, the HCOOH faradaic efficiencies grow up similarly, but with a less marked increase. Instead, contrary to the sample of 200 °C, the selectivity towards the hydrogen evolution reaction decreases abruptly at more negative potentials. Nevertheless, a low current density is observed, but is ascribable only to CO_2 reduction.

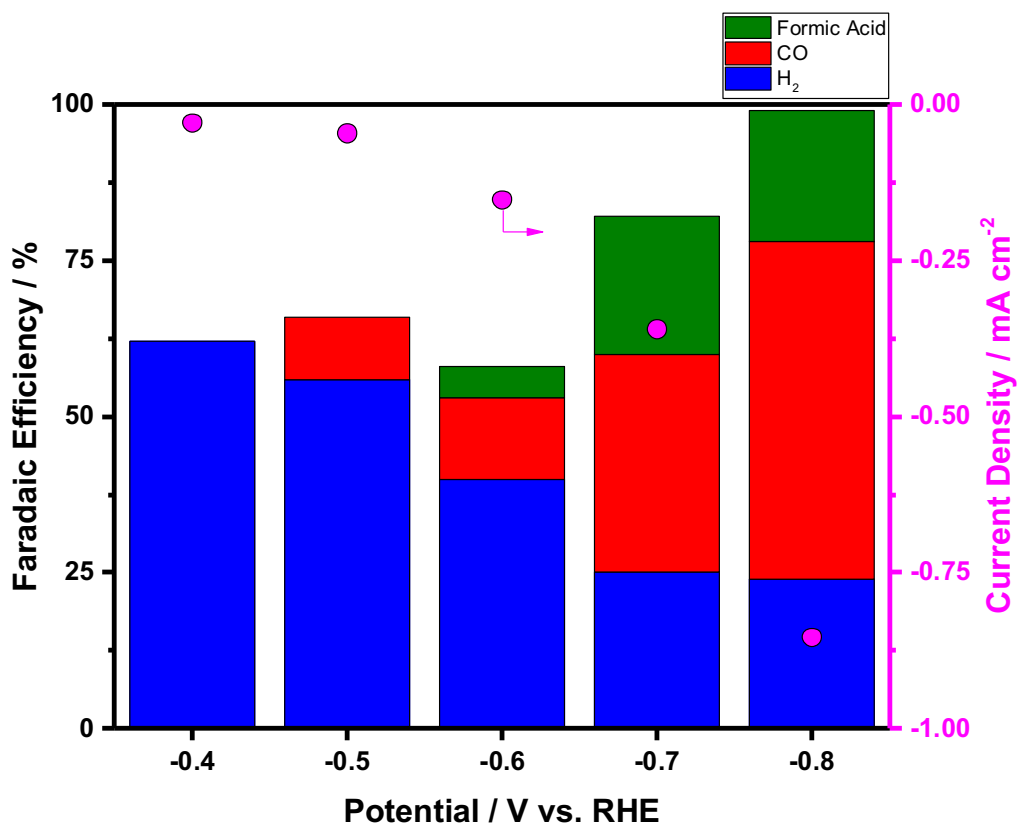


Figure 3-23. Current density and Faradaic efficiencies of the 800 °C thermally reduced sample at various applied potentials from -0.4 to -0.8 V vs RHE in CO_2 saturated 0.1 M KHCO_3 solution.

The 600 °C thermally treated electrode started to convert CO_2 to CO at -0.5 V vs RHE, while the HCOOH formation started from -0.6 vs RHE. The faradaic efficiencies toward CO_2 reduction is high, but less than the previous sample treated at 600 °C. Even the current density is lower.

3.2 *Experimental section*

3.2.1 *Materials*

An Ag/AgCl reference electrode saturated in KCl solution was obtained from BAS Corporation, Japan. A carbon paper of 0.19 mm thickness (TGP-H-60) was purchased from Toray Industries, Japan. MF-Millipore Membrane, mixed cellulose filter paper hydrophilic 0.02 μm of diameter was purchased from Merck Millipore company, Germany. High purity CO₂ gas cylinder (99.9999%) was bought from AHG industrial gases, Saudi Arabia.

The following chemicals were obtained from Sigma-Aldrich:

- Potassium bicarbonate (KHCO₃, 99.99%);
- Indium (III) oxide (In₂O₃, 99.998% trace metals basis);
- Sodium carbonate (Na₂CO₃ anhydrous, 99.999% trace metals basis);
- Copper (I) chloride (CuCl anhydrous, 99.98% trace metals basis);
- Acetone reagent grade (C₃H₆O, 99.9%);
- Copper (I) oxide (Cu₂O anhydrous, 99.99% trace metals basis);
- Iodine (I₂, 99.999% trace metals basis).

3.2.2 *Instruments*

For the CO₂ reduction experiments, a BioLogic VMP3 potentiostat was used.

Gas products were quantified using a VARIAN 450-GC gas chromatograph equipped with a 5 Å MolSieve column and two detectors: a thermal conductivity detector (TCD) and a flame ionization detector (FID) for hydrocarbons. Furthermore, a high-performance liquid chromatograph (HPLC) from Agilent Technologies equipped with an ICE-Coregel 87-H3 column and 1260 Infinity Variable Wavelength Detector for the detection of HCOOH.

X-ray diffraction (XRD) measurements were carried out using a Bruker D8 Advanced A25 diffractometer with a Cu X-ray tube (Cu K α , $\lambda = 0.154$ nm). The operating conditions used were 40 mA at 40 kV. A 3400 KRATOS AMICUS/ESCA was used for the X-ray photoelectron spectroscopy (XPS), with an un-monochromatized Al-anode K α X-ray source (1486.6 eV) activated at 15 mA and 10 kV. To calibrate the binding energy of diffractogram obtained was used the adventitious C 1s spectra with a reported binding energy of 284.8 eV.

Scanning electron microscopy (SEM) images were obtained using a Magellan 400 XHR from FEI.

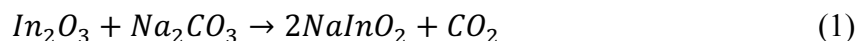
Thermo gravimetric analysis was obtained using an Automatic TGA 2 (LF) from Mettler Toledo, placing the sample into an alumina crucible.

Thermal treatments were conducted using a Tube Furnace RT 50-250/13, from Nabertherm, United States.

3.2.3 *CuInO₂ synthesis*

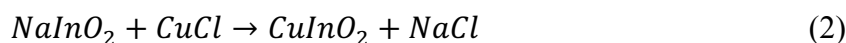
The synthesis of CuInO₂ was obtained starting from solid reactants. First, the In₂O₃ was physically mixed with Na₂CO₃ in a 1:1 molar ratio, with the help of mortar and pestle. The two powders were placed into the mortar and, few mL of reagent-grade acetone was added to improve the mixing. After vigorous mixing for 10 minutes, the acetone was completely evaporated, and the mixed powders looked like a single phase.

The dried reagents powder was transferred into an alumina boat, then heated at 1273 K in a tube furnace under a flow of nitrogen gas (300 mL min⁻¹) for 12 hours. The solid-state reaction proceeds according to the equation:



The white powder thus obtained was weighed and transferred into the mortar. At the NaInO₂ powder was added CuCl in a 1:1 molar ratio (assuming a complete conversion in the previous reaction) and physically mixed using a pestle without using acetone (to avoid the oxidation of Cu^I to Cu^{II}).

The mixed powder was transferred into an alumina boat, then heated at 773 K in a tube furnace under a flow nitrogen gas (300 mL min⁻¹) for 6 hours. The ion-exchange reaction proceeds according to the equation:



The brick red powder obtained was weighed and transferred on a Millipore cellulose filter paper with a diameter of 0.2 μm, and using a Büchner funnel was washed with Milli-Q water under vacuum, in order to eliminate NaCl from the powder. Washing was carried out several times until the wash waters give a negative result to the chlorine test with AgNO₃. Later, the filtered powder was dried in an oven at 80 °C for 2 hours.

3.2.4 Electrophoretic deposition

To prepare the working electrode with the CuInO₂ powder, a carbon paper substrate was chosen. A 1.5 × 2 cm carbon paper was cut from a carbon paper sheet, and then cleaned by sonication for 5 minutes in ethanol before and acetone after.

The electrophoretic deposition method was used to deposit the CuInO₂ particles on the carbon paper surface. A suspension was prepared by ultra-sonication using 50 mL of reagent-grade acetone, 50 mg of CuInO₂ powder and 25 mg of iodine. Using a two-electrode cell, where the counter electrode was another carbon paper sheet with the same size, the well-suspended catalyst was deposited on the carbon paper substrate applying 30 V for 3 minutes.

The film of CuInO₂ on carbon paper was then dried in vacuum oven at 373 K for 6 hours, in order to remove all the acetone and promote a good contact between the catalyst and the substrate.

3.2.5 Thermal treatment

The catalyst supported on carbon paper was thermally treated under reducing atmosphere at various temperatures. The dried CuInO₂ carbon paper supported was placed horizontally into an alumina boat and insert inside a tube furnace, where a 4% H₂ in Argon flow was flowing at 300 mL min⁻¹. Each sample was heated at various temperatures: 200, 450, 600 or 850 °C for 3 hours, under a heating ramp of 200 °C h⁻¹. After that, the sample was cooled slowly before stopping the stream of 4% H₂ in Argon, until it reached room temperature.

3.2.6 Electrochemical reduction measurements

For the electrochemical measurements, the same procedure described in Chapter 2 (2.2.6 *Electrochemical reduction measurements*) was used.

3.3 Conclusions

In conclusion, the thermal reducing treatment of the CuInO₂ can improve the performance of the catalyst. By varying the reduction temperature, it is possible to change the crystalline structure of the catalytic surface, thus orienting the selectivity of the CO₂ reduction reaction.

It is important to note that the 600 ° C sample, which showed the best results regarding selectivity towards CO and partly to HCOOH, is the only one that presents the Cu₁₀In₇ alloy on the surface of the XRD analysis. This suggests that Cu₁₀In₇ could play a central role in the selectivity of the reaction.

The thermally reduced sample at 450 ° C demonstrates that co-capability on the electrode of the two metals is not sufficient to improve selectivity, but interaction between the two is crucial to retard the performance of the catalyst. This consideration highlights the importance of a geometric factor on the catalytic surface, with the close presence of the two heteroatoms which is crucial to affect the reaction pathways.

3.4 Bibliography

- [52] A. Jedidi, S. Rasul, D. Masih, L. Cavallo e K. Takanabe, «Generation of Cu–In alloy surfaces from CuInO_2 as selective catalytic sites for CO_2 electroreduction.», *Journal of Materials Chemistry A*, vol. 3, n. 37, pp. 19085-19092, 2015.
- [53] L. Besra e M. Liu, «A review on fundamentals and applications of electrophoretic deposition (EPD).», *Progress in materials science*, vol. 52, n. 1, pp. 1-61, 2007.
- [54] A. S. Koster, L. R. Wolff e G. J. Visser, «Structure of copper–indium Cu_7In_3 .», *Acta Crystallographica Section B: Structural Crystallography and Crystal Chemistry*, vol. 36, n. 12, pp. 3094-3096, 1980.
- [55] S. Piao e S. Lidin, «A New Compound in the Cu-In System—the Synthesis and Structure of $\text{Cu}_{10}\text{In}_7$.», *Zeitschrift für anorganische und allgemeine Chemie*, vol. 634, n. 14, pp. 2589-2593, 2008.

Chapter 4

4 Conclusions

This work was focused on the research of new, efficient, cost-effective and scalable Cu-based bimetallic catalysts for the CO₂ selective reduction.

- The results obtained show that it is possible to modify an Au electrode surface with Cu layers by means of a simple electrodeposition in aqueous solution. The sample prepared with a monolayer (ML) of copper on gold electrode showed the highest current density, a good reaction rate and overall catalyst activity. The CO₂ reduction led to the formation of CO, HCOOH whereas the production of low molecular weight hydrocarbons such as CH₄ and C₂H₄ was not observed.
- The prepared oxide CuInO₂ proved to be a suitable material for the deposition on a large variety of supports such as carbon paper and carbon cloth, which are commonly used in fuel cells. Once deposited on the support of choice, the oxide can be reduced to different Cu-In alloys by thermal treatment in hydrogen flow, and by varying the temperature, the surface morphology and composition can be easily tuned. The resulting materials have been used for CO₂ reduction and the alloy having composition Cu₁₀In₇ seems to be a good candidate for the selective reduction from CO₂ to CO ($\approx 70\%$ of F.E. at -0.8 V vs RHE).
- Different multi-metallic functional catalysts must be investigated in the future: literature data indicate that bimetallic Cu-Sn electrocatalysts (prepared by electrodeposition) showed a selective and efficient production of CO, and other elements such as Gallium showed catalytic performance similar to Indium. Thus, a Cu-based bimetallic mixed oxide containing these elements can be synthesized and tested as catalyst precursor for CO₂ reduction, and this strategy can be further improved.